2000

Point Doppler velocimetry measurements in circular jets

Patrick Michael Collins
West Virginia University

POINT DOPPLER VELOCIMETRY MEASUREMENTS IN CIRCULAR JETS

By

Patrick M. Collins

THESIS

Submitted to the College of Engineering and Mineral Resources
West Virginia University

In partial fulfillment of the requirements
for the degree of

Master of Science
in
Mechanical Engineering

John M. Kuhlman, Ph.D., Chair
Gary J. Morris, Ph.D.
Charles F. Stanley, Ph.D.

Department of Mechanical and Aerospace Engineering

Morgantown, WV
2000

Keywords: Point Doppler Velocimetry, PDV, Velocity Instrumentation

Abstract

Point Doppler Velocimetry Measurements in Circular Jets

Patrick M. Collins

Improvements have been made to an existing 2-component Point Doppler Velocimetry (PDV) system to improve instrument accuracy and repeatability and to reduce mean velocity offset. Most importantly, the original iodine cells have been replaced by vapor-limited iodine cells that are not influenced by room temperature variations. PDV is a non-intrusive laser based flow measurement technique with capabilities that are similar to hot wire anemometry, but without inserting a probe into the flow. The insertion of a probe into a flow can affect the flow, resulting in inaccurate measurements.

PDV measurements for 1 inch diameter standard, swirling, and annular jets have been made at a nominal exit velocity of 60 m/s, corresponding to a Reynolds number of 100,000. Measurements of radial profiles of mean and RMS velocities were taken for each jet from the jet exit to X/D=12 at nine different X locations. Also, centerline velocity profiles were taken from the jet exit to X/D=12. Comparisons between hot wire anemometry and PDV measurements have been made for standard and swirling jets, and PDV data repeatability has been judged by multiple runs for each jet.

Hot wire anemometry measurements in the swirling jet appear to be inaccurate for $X/D \leq 4$ due to the inability of the hot wire anemometer to accurately measure two-dimensional flow velocities. The PDV and hot wire comparisons for the standard jet have good correlation for the mean velocity; however, the RMS velocities do not agree. PDV measurements of the axial and circumferential mean velocities exhibited an uncertainty and repeatability of 2 m/s. This error, for the axial mean velocity, was of the same order as was produced by using a different calibration from the same day. PDV RMS velocities exhibited a repeatability of 0.5-1.0 m/s, and generally are about one half as large as the hot wire anemometer RMS velocities.

Acknowledgments

I would like to begin this work by thanking the NASA Langley Research Center for their support under grants NAG-1-1892 and NAG-1-2132 . I would also personally like to thank Jim Meyers, technical monitor, for the knowledge that he has provided for this project. I would also like to thank AFOSR/DEPSCoR for the support under grant F49620-98-1-0068, M. Glauser and T. Beutner technical monitors.

I would like to thank Tom Scarberry for the assistance he provided over the summer for much of the preliminary work needed for this project. I would also like to thank David Webb for the software that he has written, making much of the data reduction automated and less prone to user error.

The Mechanical and Aerospace Engineering faculty and staff deserve recognition for all the support they have provided during my education. In particular I would like to thank Dr. Kuhlman for the guidance and knowledge that he has provided on this project and in the classroom. It is because of him that my career is taking off into the direction of my choice.

And finally I would like to thank my parents for all of the support, financial and otherwise, that they have provided me with during my college years. Without them this thesis and my college education would not have been possible. I dedicate this thesis to the both of you.

Table of Contents

Figure List

Chapter 1: Introduction

Flow measurement techniques can be grouped into two main categories. The first type is categorized as intrusive, in which some type of probe is inserted into the flow for measurement. Intrusive measurement techniques are generally relatively simple and inexpensive; however, the probe that is used to measure the flow can alter the flow significantly. The second type of flow measurement method is categorized as non-intrusive, which is generally an optically based measurement. Non-intrusive measurements do not alter the flow; however, they are more complex, require more expensive equipment, and often are more sensitive to outside interference.

The most common and simplest method of flow measurement is accomplished by a pitot-static probe. Pitot-static probes can be connected to a manometer or pressure scanner to measure the difference between static and stagnation pressures, and hence the fluid velocity. Even with the use of a pressure scanner the response time of a pitot-static probe based measurement system limits results to mean velocity flow measurements. Direction of flow cannot be resolved by pitot-static probe measurements. The pitot-static probe can only determine the velocity component of flow aligned with it and is susceptible to errors in turbulent flows.

Another well established intrusive flow measurement system is known as hot wire anemometry (Bruun, 1995). This method consists of placing a very thin wire or film into a flow. This wire is used as a resistor in a Wheatstone bridge. The resistance of the wire is a function of temperature. The convective cooling of the wire is measured by the imbalance in the bridge voltage. A feedback amplifier applies a higher bridge voltage to maintain a constant temperature of the wire. Because of the very fast response time of

this system (order of 100 kHz) a hot wire anemometer can be used to measure both mean and turbulent velocities as well as time histories of coherent structures at a point in a flow. The hot wire anemometer cannot resolve the direction of flow, and can incorrectly report flow velocities due to velocity components which are not perpendicular to the wire.

One well established non-intrusive flow measurement technique is known as laser Doppler velocimetry (LDV). In LDV two focused laser beams intersect in a seeded flow and the light scattered off the seeding material is measured. The overlapping of the two beams displays interference fringes, which are dependent on laser frequency and the angle between the beams. As the particles pass through the interference fringes the beat frequency of the scattered light is used to determine velocity. LDV can determine flow direction through use of an acousto-optical cell that adds a known offset to the flow in one direction. LDV can measure mean flow and turbulence statistics; however it generally cannot be used to follow time histories of coherent structures.

Another popular non-intrusive flow measurement technique is known as particle image velocimetry (PIV). In PIV a laser sheet illuminates a seeded flow and individual seeding particles are followed. The time interval between two snapshots of the flow is used to calculate velocities of each particle. The seeding material must be small enough not to alter the flow but it also must be large enough that it can be resolved by the optics. Problems can also arise when the seeding particle moves out of the light sheet plane and is lost. PIV can measure mean velocities and get turbulence statistics; however like LDV, it generally cannot follow time histories of coherent structures.

The focus of this research is on the accuracy improvement of a point Doppler velocimeter (PDV) system, as well as its comparison to an established technique. The

measurements and comparisons are to be made on three different circular jets. PDV is a non-intrusive laser based measurement system where scattered laser light is collected from a point in the flow and encounters a beam splitter. One portion of the beam is focused on a photodetector called the reference photodetector. The other portion of the beam passes through an iodine absorption cell and is focused on a second photodetector called the signal photodetector. From the voltages produced from the signal and reference photodetectors the Doppler shift of the light can be found. This Doppler shift can be used to determine velocity. The basic Doppler velocity equation is

$$\Delta f = \frac{f_o}{c}\left(\hat{a} - \hat{l}\right)\cdot\vec{V}$$

Equation 1.1

Here Δf is the Doppler shift, f_o is the laser frequency, c is the speed of light, $\hat{a}$ is a unit vector between the flow and the velocity measuring component optics, $\hat{l}$ is a unit vector along the laser and $\hat{V}$ is is the particle velocity. For a schematic of the relevant vectors of the Doppler equation see Figure 1.1. The vectors $\overline{M}d_1$ and $\overline{M}d_2$ are the measurement direction vectors, which are the bisectors between the laser vector and viewing vectors. The iodine absorption cell absorbs a varying amount of the scattered light as the frequency varies. The left half of a typical absorption line from a cell calibration can be found in Figure 1.2.

The PDV system previously used by James (1997) and Webb (1999) has undergone some modifications in the present work to improve accuracy and repeatability, and to reduce offset error. Webb demonstrated that rather large errors could occur due to a $\pm 0.1^0$ C temperature drift of the iodine absorption cell stem temperature for the iodine

absorption cells used in that work. This error was caused by the changing amount of iodine vapor in the cell as the cell stem temperature varied. New iodine absorption cells that only contained iodine vapor at operating temperature were purchased and installed. These vapor-limited cells had absorption characteristics that were independent of temperature. Beamsplitters that are relatively insensitive to the polarization axis of the scattered light were also installed in an effort to ensure a constant split ratio. The goal of this research, and these system modifications, was to decrease the offset in mean velocity which had been encountered previously, so as to improve repeatability, and increase the accuracy of the PDV system in use. The modified PDV system has been used in this present work to acquire 2-component mean and RMS velocity profiles in a standard circular jet with a uniform exit mean velocity, an annular jet with a non-uniform exit axial velocity profile, and a swirling jet . PDV data have been compared with hot wire probe data to assess accuracy of the modified PDV system.

Chapter 2: Previous Research Work in DGV and PDV

2.1 Early Work

Much of the work in the fields of Doppler Global Velocimetry (DGV) and Point Doppler Velocimetry (PDV) has been based on the original DGV concept, as patented by Komine (1990). Komine received a United States patent for a Doppler Global Velocimeter concept that used a laser light sheet to illuminate a seeded flow. A frequency-to-intensity converter was used to determine the Doppler shift of laser light scattered from a seeded flow, and from this the flow velocity field in the plane of the light sheet could be determined. Komine's frequency-to-intensity converter consisted of an iodine absorption cell, two CCD cameras, and recording hardware. Komine relied on an analog video divider and storage on a video cassette recorder. Large errors were associated with the separation of signals into individual channels. The absorption spectrum of iodine has been studied and presented by Tellinghuisen (1982). In the iodine absorption spectrum there are several regions of absorption, termed absorption lines, that will absorb a varying amount of light depending upon the frequency of the light.

2.2 Doppler Global Velocimetry (DGV)

Meyers and Komine (1991) developed a one component DGV system and performed measurements on a rotating wheel, a standard jet, and a flow above a 75^0 delta wing. Meyers and Komine determined that the signal processing should involve the CCD cameras being synchronized, the signal camera and reference camera images being overlaid and normalized, and correction for varying pixel sensitivities of the CCD arrays. Although real-time data acquisition was possible using analog dividers and viewing the

results on a monitor; it was found to be much more accurate to sample each image and digitally divide the signal and reference images pixel by pixel. Meyers, et. al (1991) later go into more detail about the signal processing, stating that the digital approach maintains the full resolution of the CCD cameras and allows adjustment for varying pixel sensitivities and for the removal of background light.

Later Meyers (1992 and 1996) describes digital DGV image correction in detail. It was realized that through movement of the optics exact pixel overlay was impossible. The concept of de-warping was introduced. De-warping was the process of using a calibration card containing a grid of equally spaced dots to determine the "warping" caused by small imperfections in the receiving optics of the DGV system. Grid points were isolated using a Sobel filter. Once the grid point centroids were found, bilinear interpolation was used to determine the offset required to align the grid. Instead of the entire image being dewarped, each pixel was individually mapped and adjusted. The pixel sensitivity was corrected by using a flat field illumination at two different intensities to determine the slope and intercept of the transfer function of each pixel. The transfer function for each pixel was then used to remove the sensitivity variations for each pixel.

McKenzie (1995) performed a very theoretically complete error analysis and concluded DGV should be able to provide measurements within 2 m/s for flows in the tens of m/s range. McKenzie used a pulsed Nd:YAG laser with only one camera per DGV component. The single camera setup used pairs of beam splitters and mirrors to divide the image for Doppler shift measurement, and then projected the signal and the reference image onto a scientific grade cooled CCD camera. This single camera setup was used to reduce the number of cameras required, as these cameras were rather expensive.

McKenzie also examined the effects of absorption cell temperature drift and vapor pressure; he found that the light transmission is a weak function of cell body temperature but a very strong function of cell stem temperature for cells containing solid phase iodine in the stem.

Ainsworth and Thorpe (1994) proposed using DGV for measurement in transonic turbine applications. In this paper they present a chart displaying the effect of scattering angle on light scattering power, for their particular seeding particles. This chart shows two minima that occur in what is referred as side scattering scatter angles. They also present a chart showing the frequency drift of an argon ion laser over the period of 0.02 seconds. The data collected by Ainsworth and Thorpe indicates a nominally 200 Hz oscillation in output frequency with an amplitude of 10MHz. A very strong case is made for the need of a laser frequency monitoring system, by showing errors of ±5m/s can be attributed to this oscillation of laser frequency. In a later paper (Thorpe., et al 1996) a slight drop in centerline velocity in the potential core of a circular jet is noticed; it is uncertain if this drop is a physical phenomenon or due to measurement error.

Forkey et al. (1995) present measurements in a Mach 2 free jet. A pulsed Nd:Yag laser was used in their DGV measurements. Velocity measurements in still air were taken and the velocity reported ranged from -12 m/s to 31 m/s. The measurements on the Mach 2 jet show core velocities between 192-221 m/s. In the error analysis performed uncertainty of the measurement should be no larger than 3.5 m/s. The predicted uncertainty of the Mach 2 jet should be no larger than 5.1 m/s. The excessive error was attributed to the nonlinearity of the system and the non-uniformity of the laser light sheet energy across the beam.

Smith and Northam(1995) also developed a DGV system utilizing a pulsed Nd:Yag laser and a single camera setup for each component. It was noted that in addition to reducing cost, the single camera setup eliminated any problems associated with unequal pixel response that can result from manufacturing tolerances for two separate cameras. Experiments were performed using different camera and lens setups. Using cooled high-grade CCD cameras 10 seconds were required to transfer an image so a faster, less expensive, non-intensified camera was used. The non-intensified camera could transfer the images at an acceptable rate, but brightness became an issue. Smith stated that the largest source of random errors in DGV measurements was laser speckle. In a later paper (Smith 1998), great care was taken to reduce speckle noise by carefully selecting optical components. A laser frequency monitoring system was also employed to reduce velocity errors due to laser drift.

Elliott et al. (1997) reported DGV measurements of a transverse jet in a supersonic cross-flow. The DGV setup used a pulsed Nd:YAG laser with a pressure broadened vapor-limited iodine absorption cell. The pressure broadened cell allows measurements to be made on higher speed flows by making the slope of the absorption line less steep, covering a wider range of frequencies. The measurements presented included mean velocities and turbulence quantities upstream and downstream of the jet location. The separation shock, bow shock and mixing layer of the jet turning into two counter rotating vorticies were shown by the data.

Beutner et al. (1998) reported DGV measurements from large-scale wind tunnel facilities. Beutner noted that the transmission function was very dependent on the cold finger (stem) of the iodine cell containing iodine in solid form. Due to the harsh wind

tunnel environment maintaining a constant temperature of the cold finger became very difficult. Vapor-limited cells, that contained no solid iodine at operating temperature, were developed and found to be relatively insensitive to temperature changes.

Three-component DGV measurements on high speed flows were recorded by Samimy (1998). Samimy compares data between DGV with and without a laser frequency monitoring system and LDV. The normalized data was presented and appeared to agree well with LDV data when a laser frequency monitoring system was used.

A two-component DGV system was used to make measurements on a rotating wheel and on a turbulent pipe/jet flow by Naylor (1998). An accuracy of 2% for a maximum of 58 m/s was achieved for DGV data taken on a rotating wheel. For the pipe/jet flow RMS errors in the 5-10% range were achieved, however the velocity offset error was as high as 10-15% of the 42 m/s velocity range.

Currently most DGV researchers are moving away from continuous wave argon-ion lasers to pulsed Nd:YAG lasers. The use of the pulsed laser freezes the flow and allows turbulence statistics to be generated using the relatively slow CCD cameras. Vapor-limited cells are also becoming more popular due to their absorption stability with temperature fluctuations. New technology in the computer and frame grabber fields will allow storage of more images and faster data acquisition all at a lower price than before.

A review of recent advancements in DGV can be found in Elliott and Beutner (1999). Elliott and Beutner discuss the theory behind DGV, the components of DGV, data processing, development and applications of DGV, measurements, and uncertainity analysis in the current state of the art DGV systems.

2.3 Point Doppler Velocimetry

Roehle and Schodl (1996) made single-component PDV measurements on a free jet and obtained measurement uncertainties of less than ±3m/s, with a maximum mean velocity of 115 m/s. Roehle and Schodl used an argon ion laser; however they used an optical chopper in conjunction to achieve a pulsed laser effect. The photomultiplier tube signals were amplified with a lock-in amplifier, which only allowed the signals that were in phase with the optical chopper to pass. This insured that only the scattered laser light is measured. They also used a unique laser frequency control system, consisting of a piezo translator mounted on the back laser mirror so that the laser frequency was controlled by traversing the mirror. A spectrum analyzer was used to measure laser frequency and generate an error signal, which was fed into a PI controller for short-term control. The PI controller stabilized the laser frequency on a point of the transmission profile slope of the spectrum analyzer. Short-term fluctuations in the laser output were lowered to ±250 kHz. The frequency drift of the spectrum analyzer was not neglected either. For operating times longer than 1 minute a control was established using the hyperfine structure of iodine as a frequency standard.

Hoffenberg and Sullivan (1993) developed a single-component PDV system and compared the results to LDV for a turbulent jet flow. Using an argon ion laser a laser beam was focused down to 0.25mm in diameter into a seeded flow. An iodine absorption cell was used to determine the Doppler shift of the light scattered from the flow. Instead of photodetectors, photomultiplier tubes were used. Hoffenberg and Sullivan determined that: alignment is very important, as probe volume is reduced seeding concentration must be increased, and that laser frequency must be controlled or monitored.

McKenzie (1995) used a single-component PDV system to make measurements on a rotating wheel. McKenzie however used a pulsed Nd:YAG laser and only one photodetector per velocity measuring component. Because the signal and reference pulse of light occurs at the same time period a signal delay in the form of a very long fiber optic cable was used. The pulse of the laser was short enough (20 ns) such that the signal and reference flash were separated. This was done to eliminate the large effects of speckle on the light scattered from the rough wheel surface. Using two photodetectors per velocity sensing component resulted in uncorrelated speckle noise with an RMS ten times higher than the noise from all other sources. Accuracies of ±2ms out of a maximum of 54 m/s were recorded.

Ramanath (1997) developed a 3-axis positioning system used in PDV and DGV measurements at West Virginia University. Early PDV data was taken by Ramanath, but due to inadequate calibration procedure, this data was inaccurate. James (1997) continued this research and was able to develop a calibration procedure that was able to produce data with errors of 1-2% for a full scale of 56 m/s on a rotating wheel. Data was also taken on a turbulent pipe flow with reasonable results, however inaccuracies determining zero velocity existed. Webb (1999) made PDV measurements above an airfoil and obtained mean velocity errors of 2-4 m/s for a 22 m/s flow. Determination of zero velocity was also a large source of error. The RMS velocities however agreed well when compared to hot wire measurements. Webb concluded that because the iodine absorption cells used contained solid phase iodine that a stem temperature drift could result in mean velocity errors of 1.6 m/s for the backscatter channel and 6.9 m/s for the forward scatter channel. PDV accuracies of 2-3 m/s for mean velocity and 0.5-1.0 m/s for RMS velocity

have been documented. The present work is to improve on the mean velocity accuracies of Webb.

Chapter 3: Apparatus and Configuration

A general sketch of the PDV measurement laboratory layout can be seen in Figure 3.1. The basic components of the PDV measurement system included two velocity measuring PDV components, laser, a laser frequency monitoring system, computer with data acquisition hardware, traversing system and controlling computer, and the actual flow facility. For earlier PDV laboratory layouts refer to Webb (1999) and James (1997).

3.1 PDV Setup

3.1.1 Laser

The laser used in the PDV velocity measurements was a 5-watt Innova 305 continuous wave Argon-Ion laser from Coherent, operating at a single wavelength of 514.5 nm. For the velocity measurements it was necessary to operate the laser in a single mode; this necessitated the use of a heated etalon. Without the etalon and in single line mode the laser has a gain bandwidth of 6 to 8 GHz, which far exceeds the width of an absorption band of molecular iodine. With the etalon inserted in the laser cavity a fairly narrow range is possible, less than 10 MHz (Naylor 1998). The etalon also reduces available power to just under 1 watt.

3.1.2 Iodine Cells

The iodine cells used in the PDV velocity measurements were manufactured by Innovative Scientific Solutions Inc (ISSI). The cylindrical cells had a length and optical path of 5 inches and a diameter of 3 inches (Figure 3.2). They were made of Pyrex glass and filled to be vapor-limited, meaning at operating temperature (greater than 45^0 C) there would be no iodine in the solid state present in the cells. This allowed the cells transmission to be unaffected by changes in temperature. It was demonstrated by Webb

(1999) for non-vapor-limited iodine cells that a change of 0.1^0 C could produce a velocity error of 6.9 m/sec in the forward scatter channel and 1.6 m/sec in the back scatter channel. The present iodine cells were wrapped in metal foil, a flexible band heater, a layer of insulation, and another layer of metal foil. The flexible band heater was controlled by an Iomega CN9000A temperature controller that was capable of controlling the temperature at a set point to within an RMS of $\pm 0.1^0$ C. The selected operating temperature was chosen to be 80^0 C. An un-insulated and unheated stem left over from the filling process of the cells protrudes from the top of the cells.

3.1.3 Laser Frequency Monitoring System

A laser frequency monitoring system was employed to monitor and record the laser frequency variations so that any drift that occurred in the laser frequency could be accounted for in the reduction of the velocity data (Figure 3.3).

Just past the beam exit of the laser a flat 2 inch diameter piece of Pyrex glass splits the beam in two. The main beam (over 90%) passes through the Pyrex glass onto a mirror that directs the beam into the flow measurement area. The rest of the beam is sent into a large wooden box containing the laser frequency monitoring system and a laser spectrum analyzer. This box blocked any outside light from entering the laser frequency monitoring system. Once inside the box the light is split once again by second flat circular piece of Pyrex glass. One portion of the beam goes to the Burleigh Instruments model SA-200 Plus spectrum analyzer, which is connected to a Burleigh Instruments DA-100 detector amplifier, the output of which is viewed on an oscilloscope. The spectrum analyzer was employed so that mode hops could be viewed by the person tilting the etalon during the calibration process to achieve an optimal calibration. The other portion of the beam goes

through a 1% transmission neutral density filter and then through a pinhole, which is used to block out any secondary beams created by the Pyrex glass. This beam is then split by a 2 inch Melles Griot dielectric beam splitter, which is specified to be insensitive to laser beam polarization to within +/- 3%. The portion of the beam that was reflected from the surface of the dielectric beamsplitter passed through a CVI Instruments beam expander. The purpose of the beam expander was to prevent the transmission of the iodine cell from becoming a function of laser power due to saturation of the molecular iodine. The beam expander is adjustable from 4.5:1 to 10:1 and rated for wavelengths from 488 to 515 nm. The beam expander was set at a ratio of 10:1 for a wavelength of 515 nm. The light then passed through the iodine absorption cell and was then focused down by a 2 inch lens onto the signal photodetector. The other portion of the beam that passes through the dielectric beamsplitter is then deflected 90^0 by a mirror and focused by a 2 inch lens onto the reference photodetector. The photodetectors used in the laser frequency monitoring system are Thor Labs PDA 150 fixed gain amplified silicone detectors with maximum outputs of 1.5V. The Thor Labs PDA 150 has a spectral response of 400nm to 1100 nm, a rise time of 7 ns, a band width of 50 MHz, and a sensitivity of 0.3A/W at the operating wavelength of laser (514.5 nm).

The laser and laser frequency monitoring system were mounted on an optical breadboard, which was supported by a custom built vibration damping table. The vibration damping table consisted of a wooden box 3 inches high filled half way with sand. On top of the sand four 8 inch diameter inner tubes were positioned evenly, with 12 inch extension valves attached. The optical breadboard was supported entirely by the inflated inner tubes. The end of the extension valves were mounted in the sides of the sandbox

such that the inner tubes could be inflated or deflated to level the optical breadboard on which the laser and laser frequency monitoring system was mounted.

3.1.4 PDV Components

The PDV system used to measure flow velocities consisted of two PDV components that were identical with the exception that they are mirror images of each other (Figure 3.4). Each component was contained on an 18.5 inch by 30.5 inch optical breadboard from Thor Labs mounted on a tripod. On each optical breadboard two Melles Griot optical rails with 1mm graduations were mounted. These rails allowed optical components to be mounted and moved forward or backward to any desired location. Each velocity measuring component was covered with black cloth material to block out any undesired light.

The scattered laser light from the test area entered each component through a 2.25 inch diameter opening on the face of each component. This opening was covered with polarizing film from Edmund Scientific. The purpose of this polarizing film was to filter out any scattered laser light that did not have the same polarization as the original laser beam. The original beamsplitters used by Webb (1999) were sensitive to polarization of light and could cause a deviation from a constant split ratio. The beamsplitters used by Webb were replaced with non-polarization sensitive ones, which will be discussed shortly. The polarizing film was positioned so that it would pass the maximum amount of light possible through to the photodetector.

Once the light was inside each PDV component it was focused down to as small a point as possible and passed through a pinhole. The pinhole allowed selection of light from a single point in the flow to be measured. The adjustment of the size of the pinhole

also allowed the signal strength of each component to be adjusted as deemed necessary. After the light passed through the pinhole it was allowed to diverge to a diameter slightly less than 2 inches before it passed through another 2 inch diameter lens which gave the beam a constant diameter. The beam was then split by a 4 inch diameter custom Melles Griot non-polarizing beam splitter similar to the one used in the laser frequency monitoring system (Figure 3.2). The beamsplitter was mounted in a Newport 605-4 gimbaled mount. The light that passed through the beamsplitter then passed through an iodine cell identical to the one discussed previously in the laser frequency monitoring system. After the light passed through the iodine cell it was focused down by a 2 inch diameter lens to a point onto the signal photodetector, which will be described below. The light that was reflected by the beamsplitter was reflected once again by a 4 inch diameter mirror mounted in an Aerotech A0M110-4 gimbaled mount. The mirror was from Newport, model 40D10BD.1, and had an antireflective coating on it. The components of the signal and reference channel of each velocity measuring component were carefully placed so that both had the same optical path length from the beamsplitter.

3.1.5 Component Photodetectors

The photodetectors used in the velocity measuring PDV components were Thor Labs model PDA55 switchable gain silicone photodetectors. The photodetectors had 5 discrete gain settings of 0, 10, 20, 30, and 40 dB which were selectable via a 5 position click stop switch. They had a spectral range of 400-1100 nm. The active area of the photodetector was approximately 13mm^2. The photodetectors had a bandwidth of 10 mHz at the minimum gain setting but, the bandwidth decreases as the gain setting is increased. Because the photodetectors in the backscatter unit were set to the maximum

gain setting they had a bandwidth of 60 kHz. The photodetectors in the forward scatter unit were set on gain #4 and had a bandwidth of 170 kHz. They had a maximum spectral responsivity of 0.6 A/W at approximately 900 nm and spectral responsivity of 0.3 A/W at 514.5 nm, the wavelength of the laser used in the velocity measurements.

3.2 Flow Facility

3.2.1 Traverse

The jet flow system was mounted on an electrically driven traversing system. This traversing system allowed the laser and other PDV components to remain stationary while the flow was moved to map out velocity profiles. The traverse had a movement range of 24" by 18" in the horizontal plane, with a movement of 12" in the vertical direction. It was found that for uni-directional moves of a few inches the traverse had an accuracy of 0.001" (Webb, 1999). A schematic of the traversing system can be found in Figure 3.5 while a full description of the traversing system can be found in Ramanath (1997).

3.2.2 Flow Facility

The flow was provided by a Clements Cadillac 9 amp Quick-Vac blower. The blower speed was controlled by a Powerstat variable auto transformer from Superior Electric. This variable transformer allowed voltage to the blower to be controlled from 0V to 115V. A 20.5 inch long steel diffuser was attached to the blower, with a diameter of 2 inches at the blower end and a diameter of 4 inches at the outlet end. In the end of the diffuser soda straws were glued in to serve as flow straighteners. Attached to the end of the diffuser was a clear Plexiglas circular channel 5 inches in length by 4 inches in diameter. A plenum and nozzle were then attached to the Plexiglas channel. A schematic of the flow facility can be found in Figure 3.6. The plenum was constructed with a 5 inch

radius circular converging contour arc, and the nozzle continued this arc and reversed curvature at a tangency point to complete the contraction; see Figure 3.7 (Cavage 1992). The nozzles used had a diameter of 1 inch. The annular nozzle used had a center body 0.5 inches in diameter installed on the nozzle centerline. The center body has a length of 4.5 inches with its hemispherical tip countersunk 0.5 inches into the nozzle (Figure 3.8). For swirling jet measurements the standard nozzle was is used, with a swirler installed in the Plexiglas chamber at the end of the diffuser. The swirler was constructed from a personal computer fan, with an aluminum hemispherical nose on the upstream side and a smooth conical tail behind the fan (Figure 3.9). The PC fan used had an inner diameter of 2 inches, an outer diameter of 3.5 inches, 5 blades each with a nominal chord length of 1.25 inches, which varied from 1 inch at the hub to 1.625 inches at the tips of the blades. The hemispherical nose of the swirler has a radius of 1 inch. The conical tail section has a length of 2.5 inches, making the total length of the swirler 3.5 inches. The swirler was mounted in the Plexiglas channel by inserting it into a "keyed" mounting system. This keyed mounting system was made by gluing thin pieces of Plexiglas in key locations circumferencially around the Plexiglas channel. The tips of the swirler had tabs glued to the ends of them that allowed insertion, then the swirler to be locked into place by rotating it approximately 15 degrees.

3.2.3 Flow Seeding

For PDV velocity measurements to be taken the flow had to be seeded with some type of small particles. The chosen seeding particles were theatrical fog, which had an average diameter of 1 μm. The fog particles are small enough to be expected to accurately track the flow. A Rosco model 1500 fog machine would vaporize an ethylene-

glycol based fluid, then the fog would be pumped into a 32 gallon plenum. The purpose of this plenum was to dampen out oscillations in smoke production that occur. The fog was then drawn from the top of the plenum into the blower via a flexible household clothes dryer duct. The Rosco fog machine has been modified by placing two voltage dropping diodes in series with the pump motor to lower the amount of fog produced at the lowest setting. This modification was needed because the original design produced too much smoke and would saturate the photodiode outputs.

3.3 Hot Wire Anemometer

The hot wire anemometer used in data comparisons was a Dantec 55P04 single sensor probe. The probe was connected to an IFA-300 constant temperature anemometer from TSI inc. The IFA-300 is capable of 1 to 16 channel operation at up to 300 kHz. It provides 12-bit analog to digital conversion. All operations are controlled via an RS-232 interface.

3.4 Computer Equipment

3.4.1 Computers

The data acquisition computer was an IBM compatible PC running Microsoft Windows 95. This computer contained an Intel 400 MHz Pentium II processor, 64 megabytes of RAM, and three hard drives with just over 13 gigabytes of storage. This computer was interfaced with an IO Tech A/D board which is described in the next section. The other computer, which was used to control the traverse was also an IBM compatible PC running Microsoft Windows 95. It contained an Intel compatible 486 class processor running at 80 MHz. Speed of processing was not a concern with this computer, because it is only used with the traversing system and a Star 2000 pitot probe data

acquisition system that would not benefit from a faster CPU. The data acquisition computer for the hot wire anemometer was an IBM compatible PC with an Intel compatible 350 MHz processor, 13 gigabytes of storage, and 128 megabytes of RAM.

3.4.2 Data Acquisition Boards

The main data acquisition board used in velocity measurements was an IO Tech ADC488/8SA 16 bit variable gain A/D board. This board is an external unit that was interfaced with the main data acquisition computer via an IEEE 488 cable and National Instruments AT-GPIB/TNT controller card capable of a sustained 1MB/sec transfer rate. The maximum output of the IO Tech board was 200 kB/sec. The board has 8 differential input channels with simultaneous sample and hold capabilities. In the velocity measurements 6 of these channels were used. The voltages were converted to digital signals every 10 μs in a first in first out manner (FIFO) and then sent to the data acquisition PC. It was capable of sampling rates up to 100 kHz for a single channel, but in the configuration used it was limited to a maximum sampling rate of 10 kHz.

A secondary data acquisition board, National Instruments AT-MIO E series, was used to monitor the iodine cell temperatures. This board was an 8 channel 16-bit board with a maximum sampling rate of 20 kHz. This board did not have the simultaneous sampling capability of the IO Tech board used for velocity measurements. Because the temperature fluctuations of the cells were a fairly slow process, sampling rate and non-simultaneous sampling were not concerns.

Chapter 4: Data Acquisition and Processing

Data acquisition and reduction software, using Visual Basic 4.0 32 bit edition, was originally developed and described by Naylor (1998) and James (1997). This software was modified by Webb (1999) to be more user-friendly, reduce roundoff error, and to be somewhat more automated.

4.1 Alignment and Calibration

The PDV system had to be aligned and calibrated so that photodetector voltages could reliably be converted to velocity components. The PDV system was aligned by using a triangular vellum tab attached to the end of the flow nozzle. The traverse was moved until laser beam was centered on the tip of the vellum tab. The traverse was then moved in very small increments until a small triangle, estimated to be about 4mm on each side, was formed at the tip of the tab and the light reflecting off the tab was as bright as possible. The PDV velocity sensing components were then checked for alignment. The adjustable pinhole iris inside each of the components was closed down to a minimum diameter (estimated to be 0.2-0.4mm) and the components were adjusted left/right and up/down such that the light passing through the pinhole produced a perfectly symmetrical "bulls eye" interference pattern on a sheet of paper placed behind the pinhole. The iris was then opened to a diameter of nominally 1.0-1.5mm for the forward scatter channel and 2.0-3.0mm for the back scatter channel. The light going through the lenses and iodine cells was checked to verify it was centered on each respective optical component. The focused down light striking the signal and reference photodetectors was then checked to verify that it was as small as possible and centered on the sensing area of the photodetectors.

The flow was turned on to a speed as slow as the blower would allow (estimated as 1-2 m/s) and the fog machine was turned on to produce smoke. The voltages of the photodetectors were checked to see that the smoke level was appropriate. When the smoke was at an appropriate level the voltages of the forward scatter photodetectors were nominally 1V on a 0-2V scale. It was noted that for calibrations, more repeatable curves were produced with the standard jet than with the swirling or annular jet. Because of this, all calibrations were done with the standard jet nozzle only.

The calibration files were 20 second long records of photodetector voltages, taken at a sampling rate of 100 Hz, in which the laser frequency was scanned throughout the frequency range of one side of the iodine absorption line by forcing the laser to mode hop, by mechanically adjusting the tilt of the etalon. The cell transmission ratio data would look much like stair steps (Figure 4.1), which would be ideally perfectly flat. For each calibration file the average ratio value for each "stair step" was taken and used as a data point in that file (Figure 4.2). The calibration files were then trimmed to contain only the left side of the absorption line. A calibration typically consisted of 10 files. All calibration files were then "slid" along the frequency axis so that the absorption lines would match up, using linear interpolation (Figure 4.3). A curve fit was then performed on all of the slid data points using the Boltzman fitting function (Equation 4.1).

$$y = \frac{A_1 - A_2}{1 + e^{\left[\frac{x - x_0}{D_x} + A_2\right]}} \qquad \text{Equation 4.1}$$

A_1 and A_2 represent the upper and lower ratio bounds, x_0 represents the frequency shifting factor, and D_x represents the scaling factor. For a more complete description of the Boltzman fitting function see Naylor (1998).

4.2 Data Acquisition

A typical data file was taken at a sampling rate of 100 Hz with a varying total number of points depending on the jet width at that axial position. The traverse was set to move at a speed in the z direction of 0.1 inches/second, and a speed of 0.3inches/second in the x direction. Files at the jet exit were 1100 points, over a distance of 1.1 inches and up to 3000 points and a distance of 3 inches at X/D = 8 to X/D = 12. For the traverses along the jet center line 3999 data points were taken to cover a distance of 12 inches. The data acquisition software was triggered simultaneously with the traversing system to map out the velocity profiles. The movement was in the z direction for all data files except for the centerline profiles, which were taken while traversing in the x direction along the jet axis. This method of data acquisition had been previously developed due to its quickness, in attempts to minimize the effects of any cell stem temperature drifts.

4.3 Data Reduction

After the calibration curve fit was performed the data reduction was begun. The sensitivities of the PDV velocity measuring components with regard to the orthogonal velocity components were dependent on the viewing angles of the velocity measuring components (Figure 3.1). For accurate measurement of the viewing angles several distance measurements were taken and the angles were calculated. The distances measured included the distance between the PDV velocity measurement components, the distance between the jet nozzle and each PDV velocity measuring component, and the distance between the mirror and each PDV velocity sensing component. These measurements included several redundant lengths not needed to calculate angles, however

allowed the angles to be calculated in two ways. The average of the two angle calculations was used for data reduction.

The raw data files were then loaded and low voltage thresholds were chosen. Typically low voltage thresholds were 0.003V for the back scatter channel and 0.01V for the forward scatter channel. If a point had a voltage for any channel below the minimum allowable voltage threshold that point was discarded. An allowable percentage of the points to be discarded was also chosen and if that amount was exceeded the user was then prompted with the option to continue or reset the minimum voltage thresholds. Typically less than 10 points out of a total of 1100-4000 in any single file were discarded.

Signal to reference voltage ratios were first calculated for each data point. Frequency was next calculated for each data point, using an inverted form of the Boltzman fitting function. Frequency shift between each point was then calculated by subtracting the frequency of the laser frequency monitoring system from that of each velocity sensing component. The relative velocities were then computed for each velocity sensing component. Then using the geometry of the system (see Figure 3.1) the orthogonal velocities were calculated. Then using an Excel macro the orthogonal velocities were plotted, the RMS velocities were calculated and plotted, and a running 10 point average was also computed and plotted for each file. It was the 10 point averages that were then saved, and 10 of these files have then been averaged to generate the final results to be presented in this work. During the 10 point running averages the distance traveled by the traverse was 0.01 inches, which is small compared to the probe volume.

Chapter 5: Results

The data collected from the present PDV velocity experiments are primarily presented herein in a condensed composite form, which show radial profiles for all X/D stations at which measurements were taken. These plots allow a quick comparison, as well as an easy way to see the overall behavior of each jet. For each of the three jets in which measurements were made, two data sets are presented to compare the repeatability of the mean and RMS velocities. Also presented are centerline velocity profiles for each of the three jets, and a complete data set for the standard jet. The complete data sets consist of pairs of graphs (mean and RMS velocity versus r/D) for each X/D station. The remainder of the complete data sets can be found in Appendix A.

5.1 Standard Jet

Composite plots of the mean velocities and RMS velocities for run 2 of the standard jets can be found in Figure 5.1 (axial) and Figure 5.2 (circumferential). The mean axial velocity at the jet exit is approximately uniform at 60 m/s, with a measured RMS velocity of 1.25 m/s. At the jet exit the variation from a smooth curve for the axial mean velocity is judged to be approximately 0.5 m/s, while variation for the axial RMS data is approximately 0.25 m/s. The axial turbulence intensity at the jet exit is 2.1%. The centerline mean axial velocity decays to 29 m/s at X/D=12 with a measured RMS velocity of approximately 5 m/s. The variability in mean axial velocity data at X/D=12 is judged to be approximately 2 m/s, and variability is 0.5 m/s for the RMS velocity. The turbulence intensity at X/D=12 is 17%. The measured RMS velocity is at a minimum value of 1.25 m/s at the jet exit and at a maximum value of 5 to 6 m/s at X/D=8. The mean circumferential velocities range from -2 m/s to 3 m/s but, the offset appears to worsen

somewhat at the edges of the jet and at larger X/D values where the smoke levels are lower. The measured circumferential RMS velocities range from 1 m/s at the jet exit to a maximum of 5 m/s at X/D = 8, and decay slightly to 4.5 m/s at X/D = 12. From the composite plot for the standard jet it can be seen that the shear layer widens until reaching the center of the jet. Once the shear layer reaches the jet center it becomes a self preserving jet, exhibiting a Gaussian lateral profile shape for all X/D locations.

A centerline velocity profile for this standard jet run can be found in Figure 5.3. The centerline profile shows a maximum axial mean velocity at the jet exit of 60 m/s, decaying to 30 m/s at X/D = 12. These values for the axial velocity compare well with the corresponding values in Figure 5.1. The circumferential velocity is offset from zero approximately 2-3 m/s through the centerline traverse. These values for circumferential velocity are within the range of those in the radial cuts shown in Figure 5.2; however the circumferential velocities in Figure 5.2 range from -2 m/s to 3 m/s. The RMS is at a minimum value of 1 m/s for the axial and circumferential directions at the jet exit, and a maximum value of 5.5 m/s for the axial direction and 5 m/s for the circumferential direction between X/D = 6 and X/D = 8. At values of X/D larger than 8 the RMS decays slightly. These RMS velocity values agree well with those of the radial cuts shown in Figure 5.2. An entire data set of radial cuts for this standard jet run can be found in Figure 5.4 through Figure 5.11, showing the data at each X/D location on a single graph.

Composite plots of the mean velocities and RMS velocities for the other standard jet run can be found in Figure 5.12 (axial) and Figure 5.13 (circumferential). The mean axial velocity at the jet exit is approximately 62 m/s, with a measured RMS velocity of 1.25 m/s. At the jet exit the variation from a smooth curve for the axial velocity is again

judged to be approximately 0.5 m/s, and for the axial RMS variability is approximately 0.25 m/s. The measured turbulence intensity at the jet exit is 2.0%. The velocity decays to 28 m/s at X/D=12 with a measured RMS velocity there of approximately 5 m/s. The variability in mean axial velocity at X/D=12 is judged to be approximately 2 m/s and 0.5 m/s for the RMS velocity. The turbulence intensity at X/D=12 is 18%. The measured RMS velocity is at a minimum value of 1.25 m/s at the jet exit and at a maximum value of 5.75 m/s at X/D=8. As with the other run, the mean circumferential velocities generally range from -2 m/s to 3 m/s, and the offset again appears to worsen at the edges of the jet and at larger X/D values, where the smoke levels are lower. The circumferential RMS velocities range from 1 m/s at the jet exit to a maximum of 5 m/s at X/D = 8, and then decay slightly to 4.5 m/s at X/D = 12. The only notable differences between these two standard jet runs are a slightly higher mean velocity at the jet exit for run 1 of the standard jet and a velocity that increases slightly at the edges for run 1, where the profile of run 2 of the standard jet is relatively flat. A centerline velocity profile was not measured for run 1 of the standard jet.

5.2 Swirling Jet

The composite velocity plots for run 1 of the swirling jet can be found in Figure 5.14 (axial) and Figure 5.15 (circumferential). The mean axial velocity at the jet exit is approximately 57 m/s, with a measured RMS velocity near the centerline of 1 m/s. At the jet exit the variation from a smooth curve for the axial velocity is judged to be approximately 0.5 m/s and for the axial RMS is approximately 0.25 m/s. The turbulence intensity at the jet exit is 1.75%. The mean axial velocity decays to 18 m/s at X/D=12 with a measured RMS velocity of approximately 3 m/s. The variability in mean axial

velocity at X/D=12 is judged to be approximately 1 m/s, and variability is 0.5 m/s for the RMS velocity. The turbulence intensity at X/D=12 is 17%. The measured RMS velocity is at a minimum value of 1 m/s at the jet exit and at a maximum value of 4.5 m/s at X/D=3, before decaying slightly to a nearly constant value of between 3 and 4 m/s out to X/D=12. The circumferential velocity at the jet exit achieved a maximum value of 20 m/s at r/D=0.4 and a minimum value of -22 m/s at r/D=-0.4, for an offset error of 1m/s. The RMS circumferential velocity at the jet exit had a maximum value of 2.5 m/s in the center of the jet, decreasing to 1.5 m/s where the mean circumferential velocity was greatest. The mean circumferential velocity at X/D=12 had a maximum value of 3 m/s at r/D=-1.5 and a minimum value of 1m/s at r/D=1.5. This shows a slight offset error of 2 m/s. The RMS circumferential velocity at X/D=12 had a uniform value of 4 m/s with a variation from a smooth curve of approximately 1 m/s. The notable characteristics of the swirling jet include a much more rounded axial velocity profile than the standard jet at the jet exit, a slight asymmetry in mean axial velocity at X/D=2, a much quicker axial mean velocity decay than the standard jet, higher RMS in the circumferential mean velocity from the jet exit to X/D=6, and offsets from zero velocity of opposite sign for the circumferential velocity at the jet exit and X/D=1.

The composite velocity plots for run 2 of the swirling jet can be found in Figure 5.16 (axial) and Figure 5.17 (circumferential). The mean axial velocity at the jet exit is approximately 60 m/s, with a measured RMS velocity of 1 m/s. At the jet exit the variation from a smooth curve for the axial velocity is judged to be approximately 0.5 m/s and for the axial RMS is approximately 0.25 m/s. The turbulence intensity at the jet exit is 1.67%. The velocity decays to 20 m/s at X/D=12 with a measured RMS velocity of approximately

3 m/s. The variability in mean axial velocity at X/D=12 is judged to be approximately 1 m/s, while variability is 0.5 m/s for the RMS velocity. The turbulence intensity at X/D=12 is 15%. The measured RMS velocity is at a minimum value of 1 m/s at the jet exit and at a maximum value of 4.5 m/s at X/D=3, before decaying slightly to a constant value of 4 m/s out to X/D=12. The circumferential velocity at the jet exit achieved a maximum value of 20 m/s at r/D=0.4 and a minimum value of -23 m/s at r/D=-0.4, for an offset of -1.5 m/s. The RMS circumferential velocity at the jet exit had a maximum value of 2.25 m/s in the center of the jet, decreasing to 1.25 m/s where the mean circumferential velocity was greatest. The mean circumferential velocity at X/D=12 had a maximum value of 3 m/s at r/D=-1.5 and a minimum value of 1m/s at r/D=1.5. This shows a slight offset error of 2 m/s. The RMS circumferential velocity at X/D=12 had a value of 4 m/s for all r/D locations with a variation from a smooth curve of approximately 1 m/s. The notable characteristics of the second swirling jet run again include a much more rounded axial velocity profile than the standard jet at the jet exit, a slight asymmetry in mean axial velocity at X/D=2 (although less than run 1 of the swirling jet), a much quicker axial velocity decay than the standard jet, higher RMS in the circumferential velocity from the jet exit to X/D=6, and a offsets of opposite sign for the circumferential mean velocity at the jet exit and X/D=1.

A centerline velocity profile for run 1 of the swirling jet can be found in Figure 5.18. The centerline profile shows a maximum axial velocity at the jet exit of 58 m/s, decaying to 21 m/s at X/D = 12. These values for the axial velocity compare well with the values in Figure 5.14. The circumferential velocity on the centerline is offset from 0 approximately 2-3 m/s through the centerline traverse. The RMS is at a minimum value of

1 m/s for the axial direction and 2 m/s for the circumferential directions at the jet exit. The RMS velocity in the axial direction achieved a maximum of 4 m/s, and the maximum in the circumferential direction was 6 m/s, both at X/D=3. At values of X/D larger than 6 the RMS decays to approximately 4 m/s for both the axial and circumferential directions. These RMS velocity values agree well with those of the radial cuts shown in Figures 5.14 and 5.15.

A centerline velocity profile for run 2 of the swirling jet can be found in Figure 5.19. The centerline profile shows a maximum axial velocity at the jet exit of 60 m/s, decaying to 21 m/s at X/D = 12. These values for the axial velocity compare well with the values in Figure 5.16. The centerline circumferential velocity is offset from 0 approximately 2-3 m/s through the centerline traverse. The RMS is at a minimum value of 1 m/s for the axial direction and 2 m/s for the circumferential directions at the jet exit. The RMS velocity in the axial direction achieved a maximum of 4 m/s, while in the circumferential direction the maximum was 6 m/s, both at X/D=3. At values of X/D larger than 6 the RMS decays to approximately 4 m/s for both the axial and circumferential directions. These RMS velocity values agree well with those of the radial cuts shown in Figures 5.16 and 5.17.

5.3 Annular Jet

The composite velocity plots for run 1 of the annular jet can be found in Figure 5.20 (axial) and Figure 5.21 (circumferential). The mean axial velocity at the jet exit exhibited a nearly symmetric “M” shape profile with a maximum velocity of 55 m/s at r/D=-0.4 (50 m/s at r/D=0.4) and a minimum value of 28 m/s at the centerline. The axial RMS of the annular jet also exhibited an “M” shaped profile with the centerline value of 4

m/s being the lowest, and the value at r/D=±0.4 being the highest at about 7 m/s. At the jet exit the variation from a smooth curve for the axial velocity was approximately 1 m/s, and for the axial RMS variability was approximately 0.5 m/s. The turbulence intensity at the jet exit on centerline was 14.5%. The mean axial velocity decays to 12 m/s at X/D=12 with a measured RMS velocity of approximately 3.5 m/s. The variability in mean axial velocity at X/D=12 was approximately 1 m/s and variability was 0.5 m/s for the RMS velocity. The turbulence intensity at X/D=12 was 30%. The measured RMS velocity was at a minimum value of 3.5 m/s at X/D=12 and at a maximum value of 7 m/s along the jet edges at the exit. The circumferential velocity at the jet exit exhibited a slight "V" shaped profile with the minimum value being -2 m/s at centerline and the maximum being 2 m/s at r/D=±0.5. The circumferential velocity was approximately zero at X/D=4, and at X/D=12 it was measured to be 2 m/s. The RMS velocity in the circumferential direction was a constant value of about 3.5 m/s for all locations in the jet.

The composite velocity plots for run 2 of the annular jet can be found in Figure 5.22 (axial) and Figure 5.23 (circumferential). The mean axial velocity at the jet exit again exhibited a nearly symmetric "M" shape profile with a maximum velocity of 54 m/s at r/D=-0.4 (45 m/s at r/D=0.4) and a minimum value of 22 m/s at the centerline. The axial RMS of the annular jet also exhibited an "M" shaped profile with the centerline value of 4 m/s being the lowest, and the value at r/D=±0.4 being the highest at 7 m/s. At the jet exit the variation from a smooth curve for the mean axial velocity was approximately 1 m/s, and for the axial RMS variability was approximately 0.5 m/s. The turbulence intensity at the jet exit on centerline is 18%. The mean axial velocity decays to 11 m/s at X/D=12 with a measured RMS velocity of approximately 3.5 m/s. The variability in mean axial

velocity at X/D=12 was approximately 1 m/s and variability was 0.5 m/s for the RMS velocity. The turbulence intensity at X/D=12 was 32%. The measured RMS velocity was at a minimum value of 3.5 m/s at X/D=12 and at a maximum value of 7 m/s along the jet edges at the exit. The circumferential mean velocity at the jet exit again exhibited a "V" shaped profile with the minimum value being -3 m/s at centerline and the maximum being 1 m/s at r/D=±0.5. The circumferential mean velocity at X/D=12 was measured to be about 1 m/s. The RMS velocity in the circumferential direction was a constant value of about 3.5 m/s for all locations in the jet.

A centerline velocity profile for run 1 of the annular jet can be found in Figure 5.24. The centerline profile shows an exit velocity of 32 m/s, growing to 40 m/s at X/D=1, and then decaying to 11 m/s at X/D=12. The circumferential mean velocity had a measured value of zero at the jet exit and had an increasing offset, reaching a maximum of 3 m/s at X/D=12. These values agree reasonably well with those of the radial profiles presented in Figure 5.24 and Figure 5.25. The axial and circumferential RMS of the annular jet along the centerline exhibited a nearly constant value of 3.5 m/s for all X/D locations.

A centerline velocity profile for run 2 of the annular jet can be found in Figure 5.25. The centerline profile shows an exit velocity of 29 m/s, growing to 38 m/s at X/D=1, and then decaying to 12 m/s at X/D=12. The circumferential mean velocity had a measured value of -2 m/s at the jet exit and had an increasing offset, reaching a maximum of 1 m/s at X/D=4. These values agree fairly well with those of the radial profiles presented in Figure 5.26 and Figure 5.27. The axial and circumferential RMS of the annular jet along the centerline exhibited a nearly constant value of 3.5 m/s for all X/D

locations.

5.4 Effect of Calibration Accuracy on PDV Velocity Results

For all of the PDV data presented two calibrations were taken for each data run. Of these calibrations the smoother of the two calibration data sets has been used to reduce the presented data. In general, the second calibration curve acquired was the better of the two taken, due to improved technique for making the laser mode hop in a controlled fashion. The data was also reduced using the other calibration curve, in an effort to quantify the repeatability of the calibrations. A 2-4 m/s difference in mean axial velocity was observed from using different calibration curves for the six different jet data sets. The mean circumferential velocity showed no noticeable difference, and both RMS velocities showed no noticeable difference when using a different calibration curve for the data reduction. The difference in mean axial velocity may be somewhat exaggerated because typically the first of the two curves would be significantly less smooth compared to what was considered a good calibration curve. Nonetheless, the observed variation of 2-4 m/s difference in the mean axial velocity for a data set reduced using a somewhat lower quality calibration data set is not too different from the observed mean velocity errors of 1-2 m/s. This supports the belief that the dominate mean velocity error is the accuracy of the cell calibrations.

5.5 PDV and Hot Wire Anemometry Comparisons

Single-component hot wire anemometry measurements were made for the standard and swirling jets for comparison purposes. For the standard jet the hot wire anemometer performed as expected, but for the more complex case of the swirling jet the hot wire results in the core of the swirl are questionable.

Figure 5.26 shows a comparison of PDV and hot wire measurements for the jet exit radial profiles for the standard jet. The PDV shows a mean axial velocity of 60 m/s, while the hot wire anemometer shows a mean velocity of 58 m/s. The mean velocities match up well, with only a 2 m/s difference. It should be noted that a series of repeat runs at the exit measured with a pitot-static probe showed a total variability of 1 m/sec. The measured RMS velocities however were much lower for the hot wire anemometer results than the PDV. This difference can attributed to the A/D board noise level, or the resolution of PDV not being as good as that of the hot wire anemometer. Figure 5.27 shows a comparison of PDV and hot wire measurements for the jet centerline profile of the standard jet. The mean exit velocities match up well; however the PDV data shows a decrease in velocity in the potential core of the jet, where as the hot wire data does not. The mean velocities at X/D = 12 also match well between the PDV and the hot wire measurements. For the RMS measurements the hot wire measured a lower RMS than the PDV at the jet exit, however at all values beyond X/D=4 the hot wire measured significantly higher RMS values. It is believed that this difference can be attributed to the differing sampling rates for the two measurements (100 Hz for PDV and 10 kHz for hot wire) and the short time records for the PDV data (average of ten 0.1 second intervals).

Figure 5.28 shows a comparison of PDV and hot wire anemometer measurements for the jet exit of the swirling jet. The mean velocities measured by the PDV and the hot wire match up well, with the exception of in the core of the vortex formed by the swirling jet. The RMS values reported by the hot wire are greater than those measured from the PDV. It should be noted however that the probe used was a single element probe designed for one dimensional flows. Note the very high RMS values (23 m/s) measured

by the hot wire in the centerline of the swirling jet; this is believed to be due to the movement of the vortex core, which is expected to be significantly colder than the surrounding air. Figure 5.29 shows comparison of PDV and hot wire measurements for the jet centerline profile of the swirling jet. The mean axial velocity measured by the PDV was 60 m/s, whereas the value measured by the hot wire was 68 m/s. The hot wire mean axial velocity measurements are higher than those from the PDV until a value of X/D=5 is reached, and then the mean axial velocities match up well. The RMS values measured by the hot wire are significantly greater than those measured by the PDV for the entire centerline traverse for the swirling jet.

5.6 Comparisons Between Standard, Swirling, and Annular Jets

From the mean axial velocity composite plots of the standard jet (Figure 5.1 and Figure 5.12) it can clearly be seen that a potential core exists in the standard jet. Viewing the mean axial velocity composite plots for the swirling jet (Figure 5.14 and Figure 5.16) and the mean axial velocity composite plots for the annular jet (Figure 5.20 and Figure 5.22) it can be seen that no potential core exists; this leads to the much quicker decay of the mean axial velocity along X/D. Also, it can be seen that the swirling and annular jets widen much faster than the standard jet. Upon examination of the centerline velocity plot for the standard jet (Figure 5.3) and swirling jet (Figure 5.18 and Figure 5.19) it can be realized that the RMS velocity is at its lowest at the jet exit, then achieves a maximum value at about X/D=4 then decays slightly. The centerline velocity plots for the annular jet (Figures 5.24 and Figure 5.25) however show a constant RMS velocity for all X/D locations.

Chapter 6: Conclusions and Recommendations

A two-component Point Doppler Velocimetry (PDV) system has been modified in an attempt to improve accuracy and repeatability of the system, as well as reduce mean velocity offset errors. The modifications to the PDV system included the installation of vapor-limited iodine absorption cells, non-polarization sensitive beam splitters, and improved photodetectors. The vapor-limited iodine absorption cells were added in an effort to eliminate any mean velocity drift caused by changing amounts of iodine vapor in the cells due to cell stem temperature fluctuations, that the previous cells were subject to. The non-polarization sensitive beam splitters were added to reduce the effects polarization could have on mean velocity caused by a non-constant split of the scattered light at the beam splitters as the polarization axis of the scattered light varied. The current photodetectors had a higher signal to noise ratio than the previous detectors, as well as discrete gain settings which reduced the bias voltages.

A series of velocity measurements were made for standard, swirling and annular jets. Comparisons between PDV and hot wire anemometer measurements in the standard and swirling jets were made. The mean axial velocities for the standard jet generally agreed within 2 m/s (about 3% of the exit velocity). PDV and hot wire comparisons for the swirling jet could not easily be made, due to the inability of the hot wire to measure multi-dimensional flow accurately, but in regions of low swirl, the PDV and hot wire mean axial velocities again agreed to within 2 m/s. PDV mean circumferential velocity offsets were no larger than 3 m/s for all three jets. These errors for the mean velocities are of the same order as the mean axial velocity difference produced by using a different calibration from the same day. The mean circumferential velocity appears relatively unchanged from

using a different calibration from the same day. Repeatability of the PDV data was generally to within about 2 m/s for the mean velocities and 0.5 m/s for RMS velocities for all three jets. This is comparable to the level of mean velocity repeatability which was observed in the present jet flows using pitot-static and hot wire anemometer probes (about 1 m/s). RMS velocity comparisons of the PDV and hot wire measurements in general, showed a lower RMS value for PDV measurements, possibly attributable to the relatively slower sampling rate (100 Hz) compared to the hot wire (10 kHz) and short time histories (0.1 second) compared to those taken with the hot wire anemometer (0.81 seconds).

The annular, and especially the swirling jet both exhibited enhanced widening and center-line velocity decay compared to the standard jet. Also, no potential core existed for either of these jets, and they both displayed higher turbulence levels.

It would prove to be very useful to take PDV measurements at discrete, fixed locations in the flow, and using the same sampling rate and time histories as those utilitized for the hot wire anemometer, for a more accurate comparison. With these data records, time auto correlations and power spectral densities could be calculated for further information about the flow behavior, as well as for direct comparison between the capabilities of PDV and hot wire anemometry.

There are also several areas that could warrant further investigation in efforts to achieve better data quality. The effects of viewing angles on scattered light intensity and data quality could prove to be useful. Methods to increase the sensitivity of the back scatter channel, without saturating the forward scatter channel would be a practical investigation. Two possible methods include adjusting photodetector signal levels with

the use of neutral density optical filters, or the adjustment of photodetector signal levels with the use of terminations of differing resistance at the interface between the BNC cable and the data acquisition A/D board.

Another possibility for future research work in the field would be the use of line scan cameras as one-dimensional photodetector arrays to develop a Multiple Point Doppler Velocimeter (MPDV). This could allow a researcher to gather data on an entire row of points in a flow simultaneously, cutting experiment time dramatically. Also, such an MPDV system, once developed, would enable calculations of both time and spatial correlations, which would provide a great deal of insight into complex flow behavior.

References

Adrian, R.J., and Yao, C., "Development of Pulsed Laser Velocimetry (PLV) for Measurement of Fluid Flow," Proceedings of 8th Biennial Symposium on Turbulence, University of Missouri-Rolla, 1983, pp. 170-186

Ainsworth, R.W., and Thorpe, S.J., "The Development of a Doppler Global Velocimeter for Transonic Turbine Applications," International Gas Turbine and Aeroengine Congress and Exposition, The Hague, Netherlands, June 13-16, 1994.

Beutner, T.J., Elliott, G., Mosedale, A., and Carter, C., "Doppler Global Velocimetry Applications in Large Scale Facilities," AIAA Paper 98-2608, 20th Advanced Measurement and Ground Testing Technology Conference, Albuquerque, NM, June 15-18, 1998.

Bruun, H. H., Hot-Wire Anemometry Principles and Signal Analysis. Oxford Science Publications,. New York 1995

Cavage, W., "The Ground Vortex Flow Field Associated with a Jet Impinging in a Cross Flow for Uniform and Annular Turbulent Axisymmetric Jets," MS Thesis, Department of Mechanical and Aerospace Engineering, College of Engineering, West Virginia University, 1992.

Elliott, G.S., Mosedale, A., Gruber, M.R., Nejad, A.S., and Carter, C.D., "The Study of a Transverse Jet in a Supersonic Cross-Flow Using Molecular Filtered Based Diagnostics," AIAA Paper 97-2999, 33rd AIAA/ASME/SAE/ASEE, Joint Propulsion Conference, Seattle, WA, July 6-9, 1997.

Elliott, G.S., and Beutner, T.J., "Moleculear filter based planar Doppler Velocimetry," Progresses in Aerospace Sciences, Vol 35. pp. 799-845, 1999

Forkey, J.N., Finkelstein, N.D., Lempert, W.R., and Miles, R.B., "Control of Experimental Uncertainties in Filtered Rayleigh Scattering Measurements," AIAA Paper 95-0298, 33rd Aerospace Sciences Meeting, Reno, NV, Jan. 9-12, 1995.

Hoffenberg, R., and Sullivan, J.P., "Filtered Particle Scattering: Laser Velocimetry Using an Iodine Filter," ASME-FED, Vol. 161, pp. 135-8, June 20-24, 1993.

James, K.M., "Determination of the Accuracy of a Two-Component Point Doppler Velocimetry System." MS Thesis, Department of Mechanical and Aerospace Engineering, College of Engineering, West Virginia University, June 1997.

Komine, H., United States patent, Patent No. 4,919,536, pp.1-16, April 24, 1990.

McKenzie, R.L., "Measurement Capabilities of Planar Doppler Velocimetry Using Pulsed Lasers," AIAA Paper 95-0297, 33rd Aerospace Sciences Meeting, Reno, NV, Jan. 9-12, 1995.

Meyers, J.F., and Komine, H., "Doppler Global Velocimetry A New Way to Look at Velocity," ASME Fourth International Conference on Laser Anemometry, Cleveland, OH, Aug. 3-9, 1991.

Meyers, J.F., Lee, J.W., and Cavone, A.A., "Signal Processing Schemes for Doppler Global Velocimetry," IEEE 14th International Congress on Instrumentation in Aero Simulation Facilities (ICIASF), Rockville, MD, Oct. 27-31, 1991.

Meyers, J.F., "Doppler Global Velocimetry *The Next Generation?*," AIAA Paper 92-3897, 17th Aerospace Ground Testing Conference, Nashville, TN, July 6-8, 1992.

Meyers, J.F., "Evolution of Doppler Global Velocimetry Data Processing," Eighth International Symposium on Applications of Laser Techniques to Fluid Mechanics, Lisbon, Portugal, pp. 1-22, July 8-11, 1996.

Naylor, S.M., "Development and Accuracy Determination of a Two-Component Doppler Global Velocimeter (DGV)", PhD Dissertation, Department of Mechanical and Aerospace Engineering, College of Engineering and Mineral Resources, West Virginia University, July 1998

Ramanath, S., "Development of a Point Doppler Global Velocimeter (DGV)," MS Thesis, Department of Mechanical and Aerospace Engineering, College of Engineering, West Virginia University, 1997.

Roehle, I., and Schodl, R., "Evaluation of the Accuracy of the Doppler Global Technique," Optical Methods and Data Processing in Heat and Fluid Flow, London, UK, pp. 155-61, Apr. 14-15, 1994.

Samimy, M., "A Review of Planar Multiple-Component Velocimetry in High Speed Flows," AIAA Paper 98-2509, 20th Advanced Measurement and Ground Testing Technology Conference, Albuquerque, NM, June 15-18, 1998.

Smith, M.W., and Northam, G.B., "Application of Absorption Filter-Planar Doppler Velocimetry to Sonic and Supersonic Jets," AIAA Paper 95-0299, 33rd Aerospace Sciences Meeting, Reno, NV, Jan. 9-12, 1995.

Smith, M.W., "Application of a Planar Doppler Velocimetry System to a High Reynolds Number Compressible Jet," AIAA Paper 98-0428, 36th Aerospace Sciences Meeting & Exhibit, Reno, NV, Jan. 12-15, 1998.

Tellinghuissen, J., "Transition Strengths in the Visible-Infrared Absorption Spectrum of I_2," Journal of Chemical Physics. Vol 76, No. 10 pp 4736-44, May 15, 1982.

Thorpe, S.J., Ainsworth, R.W., and Manners, R.J., "Time-Averaged Free-Jet Measurements Using Doppler Global Velocimetry," FED-Vol. 239, Fluids Engineering Division Conference, Vol. 4, ASME 1996.

Webb, D., "Development of and Measurements using a Point Doppler Velocimetry (PDV) System," MS Thesis, Department of Mechanical and Aerospace Engineering, College of Engineering and Mineral Resources, West Virginia University, 1999.

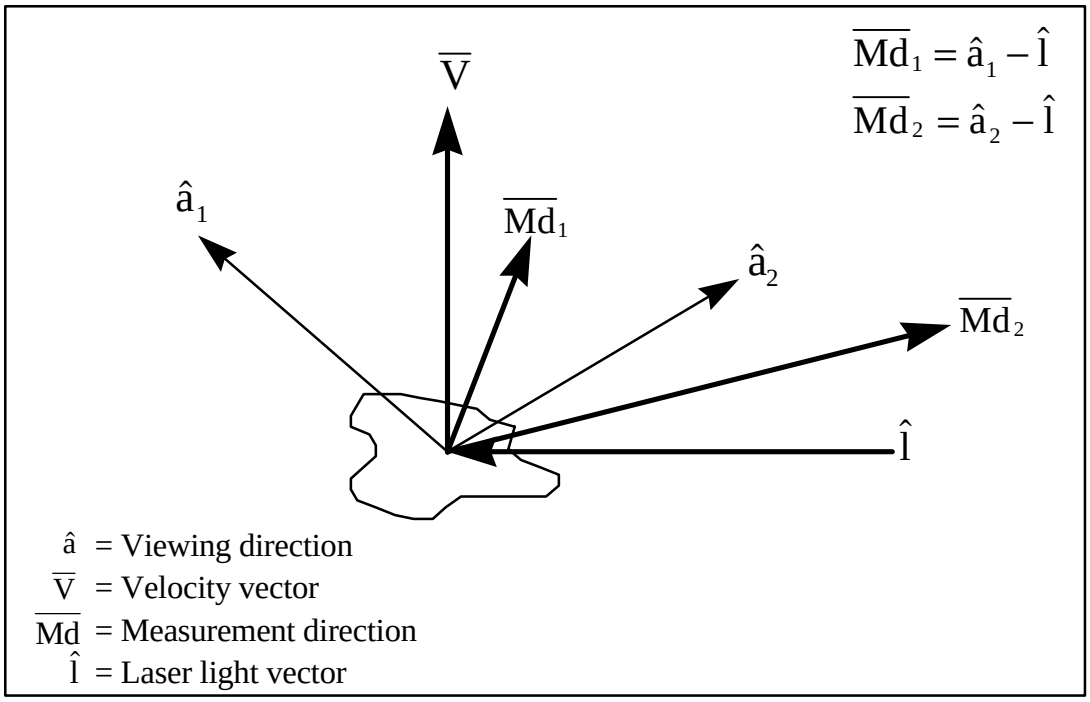

Figure 1.1. Vector geometry for a 2 component PDV system

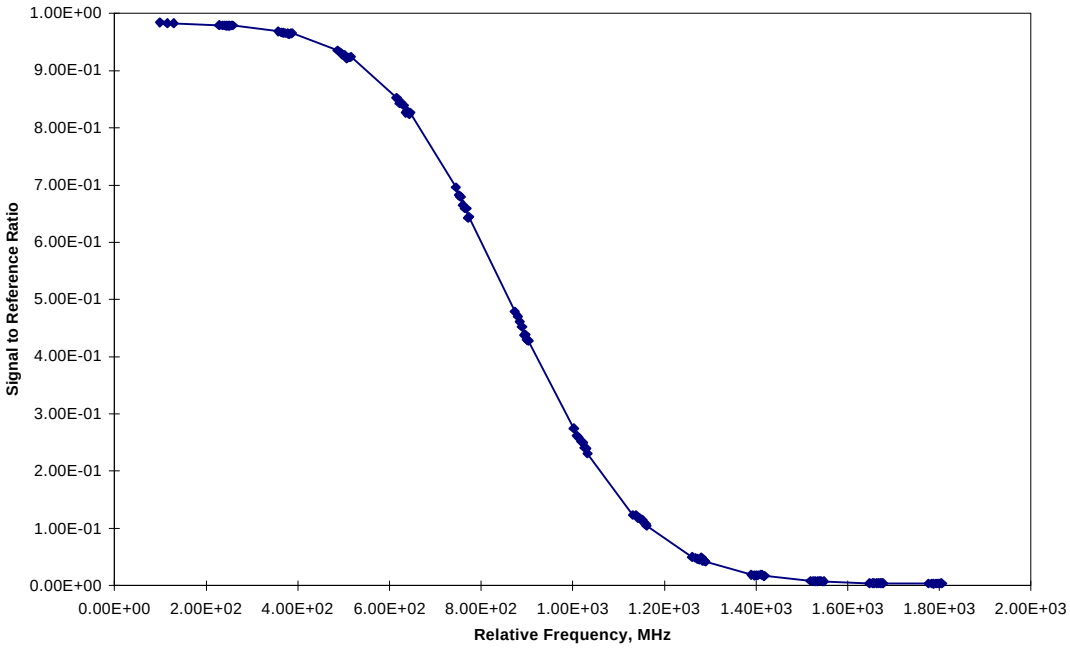

Figure 1.2. Left half of a typical absorption line of an iodine cell

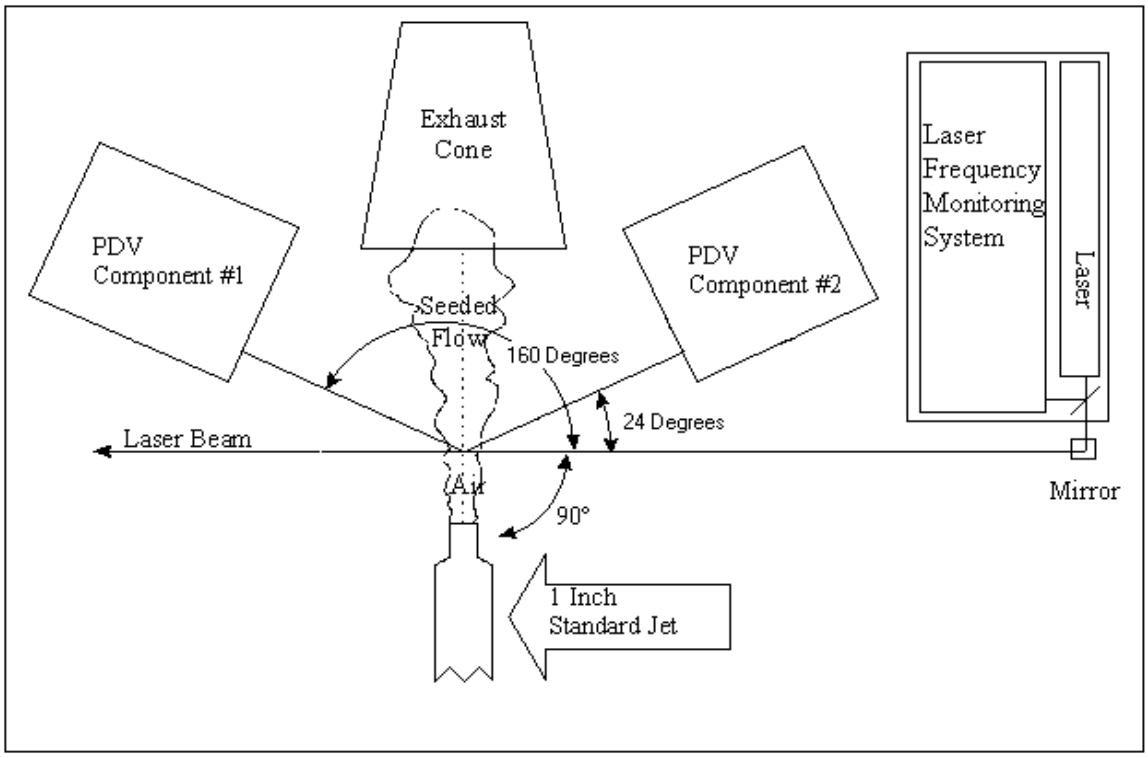

Figure 3.1. Overhead Schematic of PDV setup with typical component angles

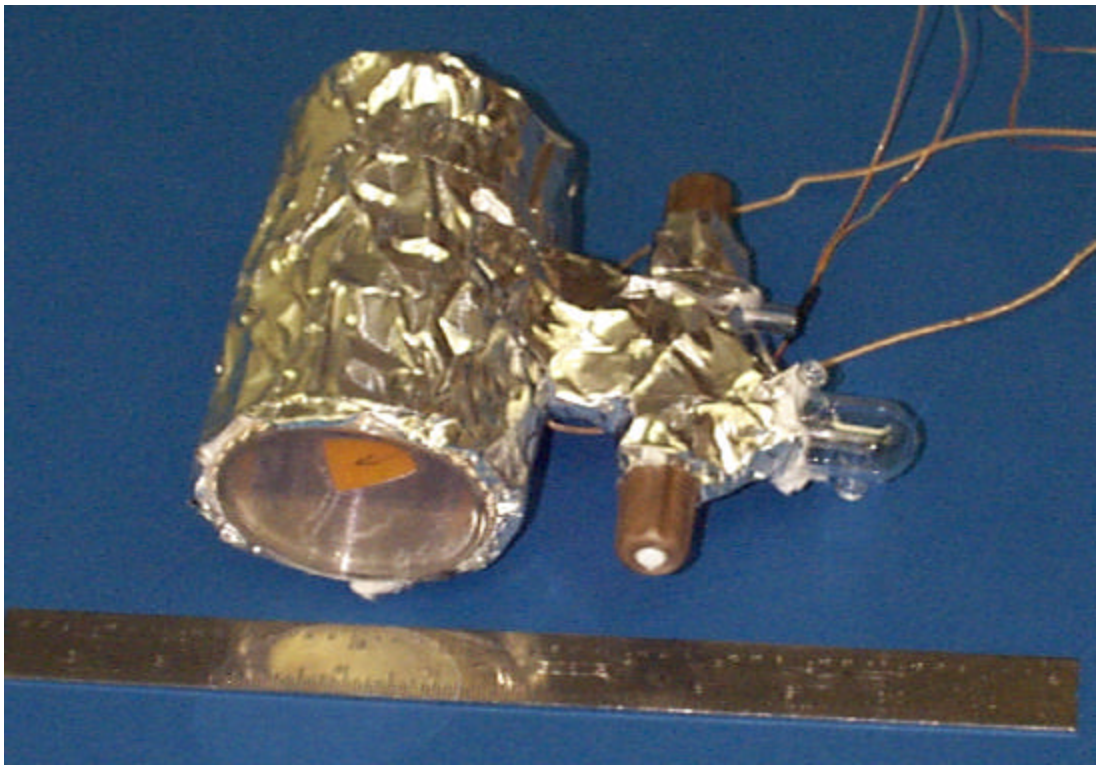

Figure 3.2. Iodine cell wrapped in heater tape and metal foil

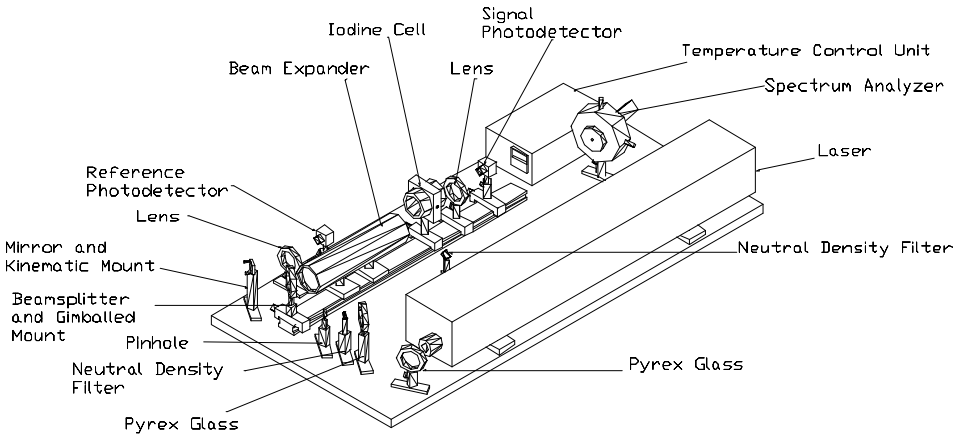

Figure 3.3. Schematic of laser frequency monitoring system

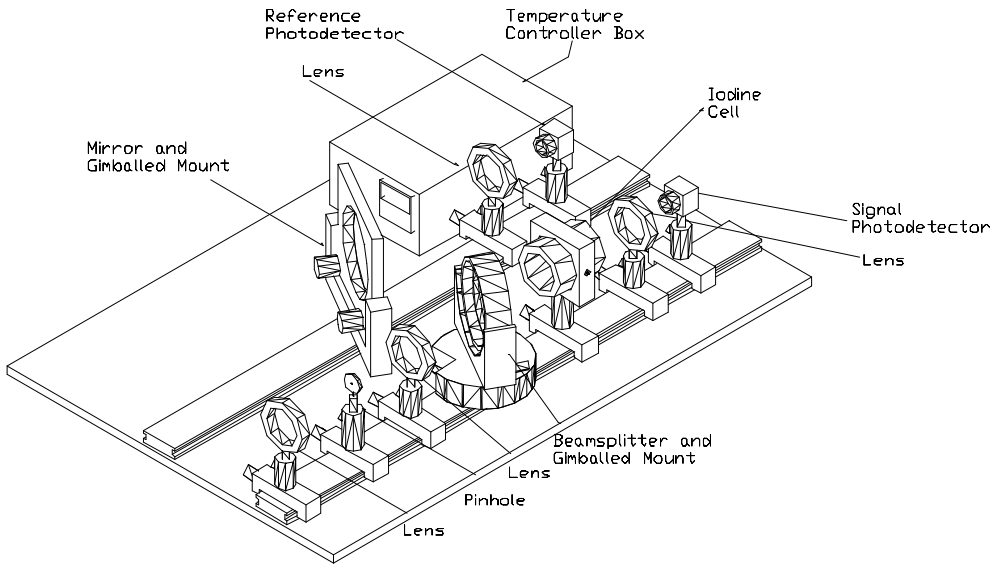

Figure 3.4. Schematic of PDV velocity measuring component

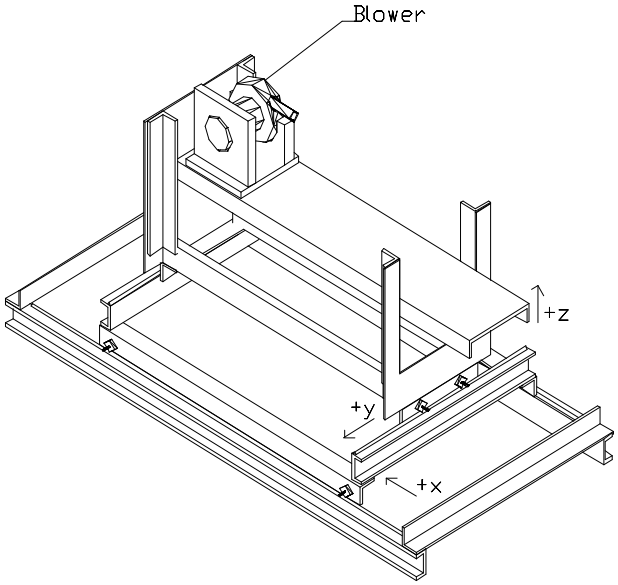

Figure 3.5 Schematic of traversing system

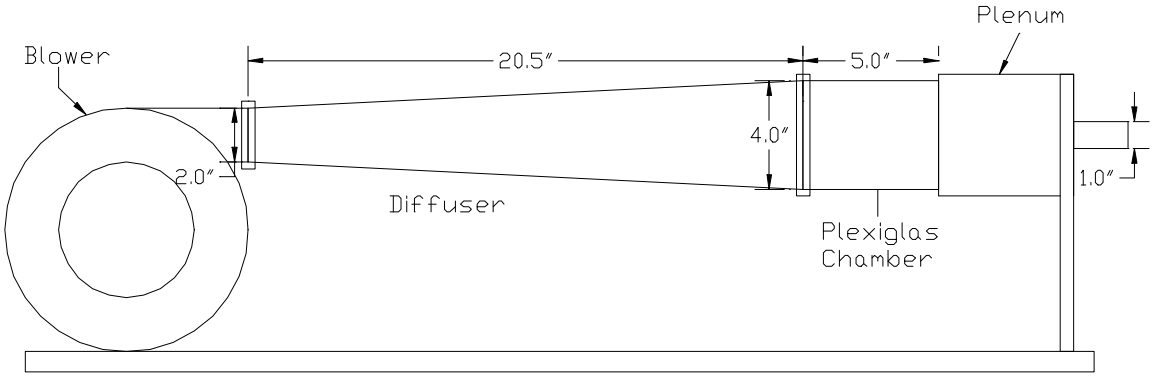

Figure 3.6 Schematic of flow facility

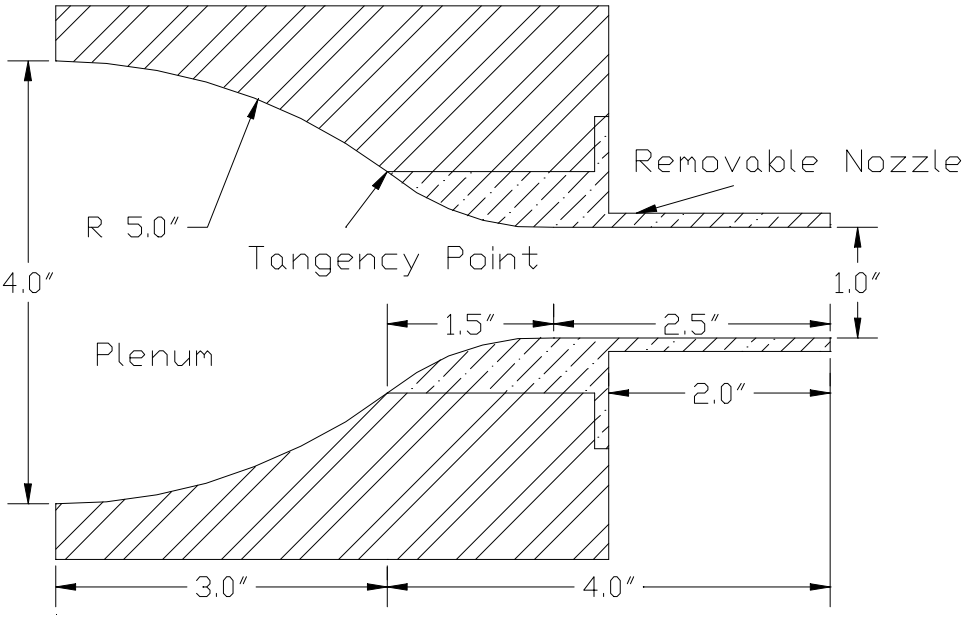

Figure 3.7. Cross Section of plenum and standard nozzle construction

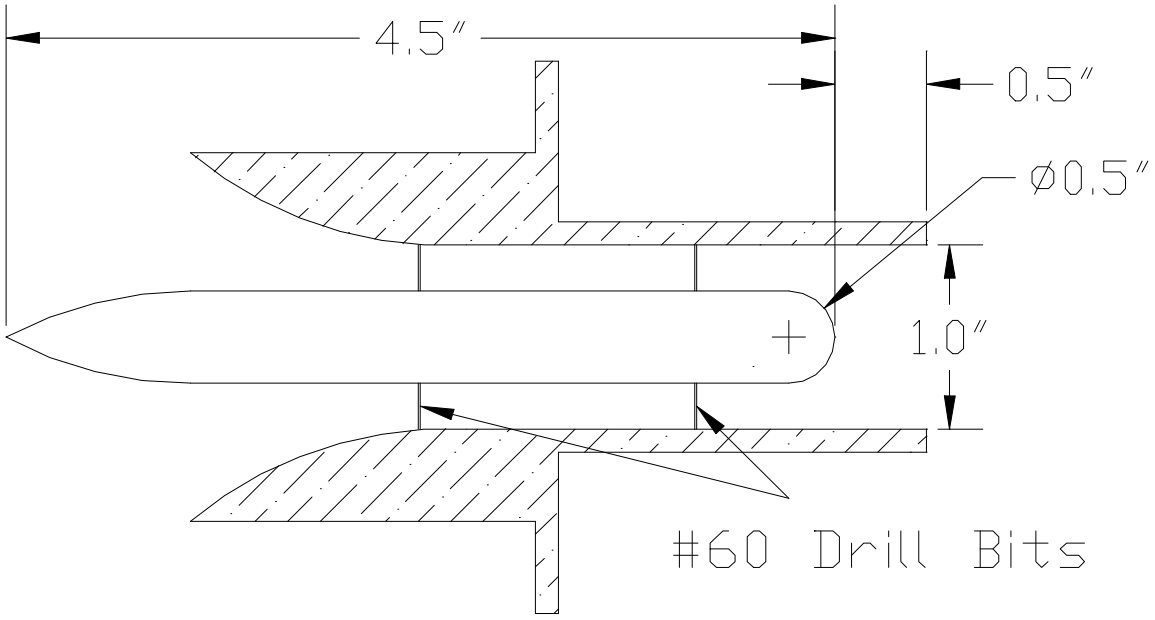

Figure 3.8. Cross Section of annular nozzle

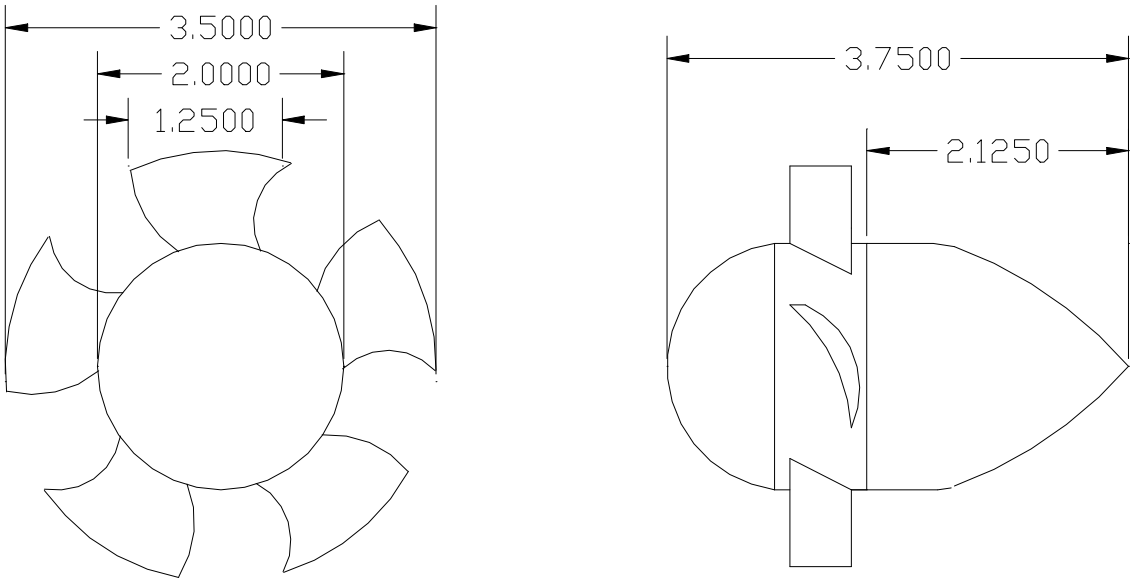

Figure 3.9. Schematic of flow swirler for swirling Jet

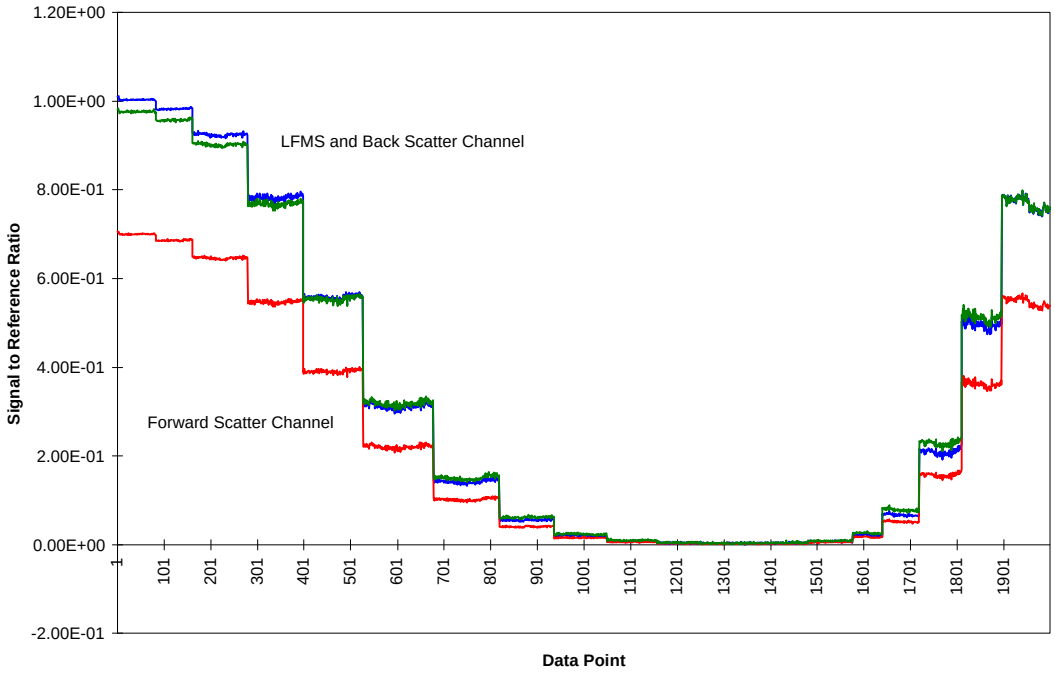

Figure 4.1. Typical raw calibration file showing ratios

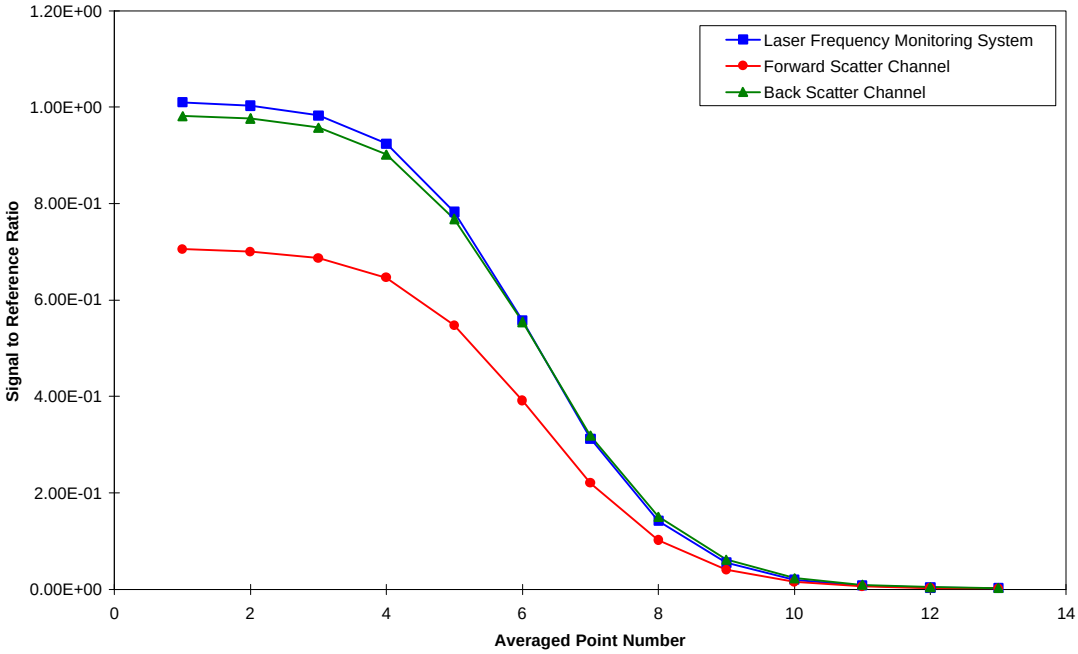

Figure 4.2. Example of a single averaged calibration file

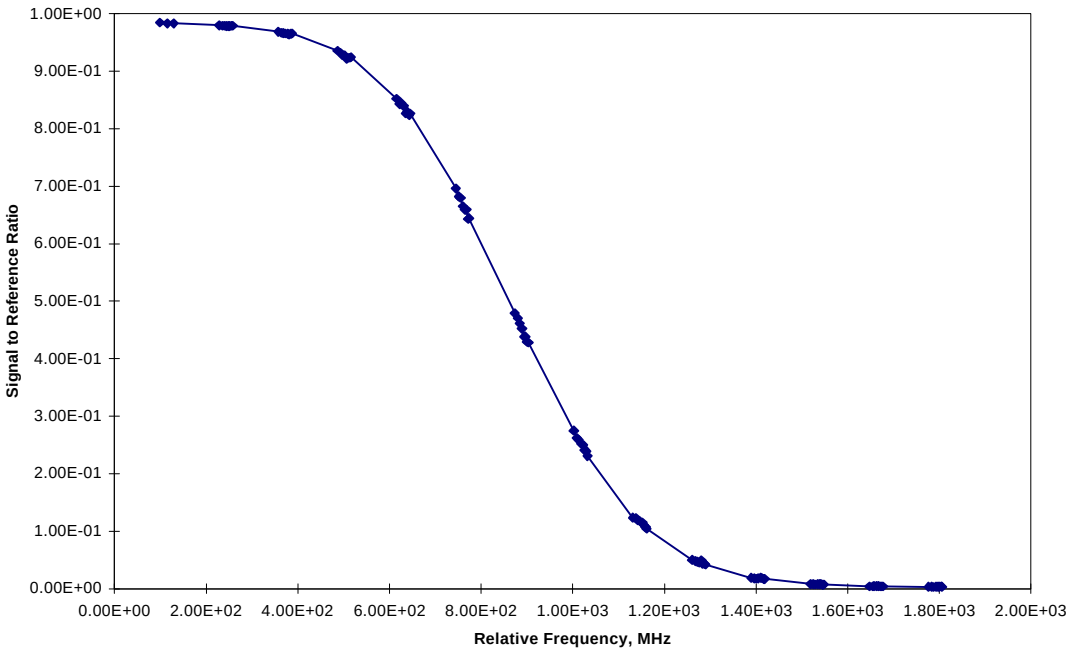

Figure 4.3. Example of a Final combined calibration file for back scatter channel

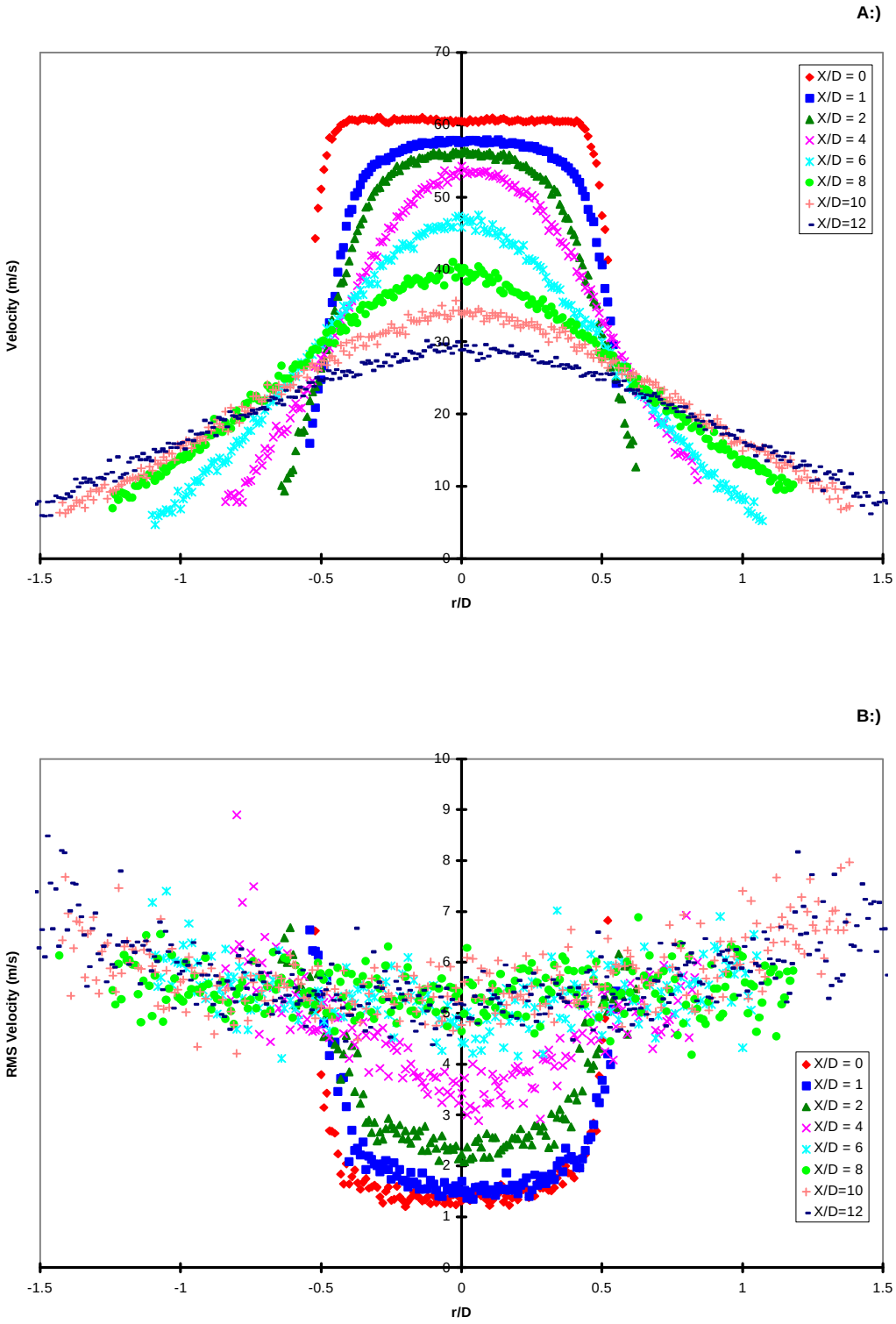

Figure 5.1. Axial composite results for standard jet, run 2
A.) Mean Velocities
B.) RMS Velocities

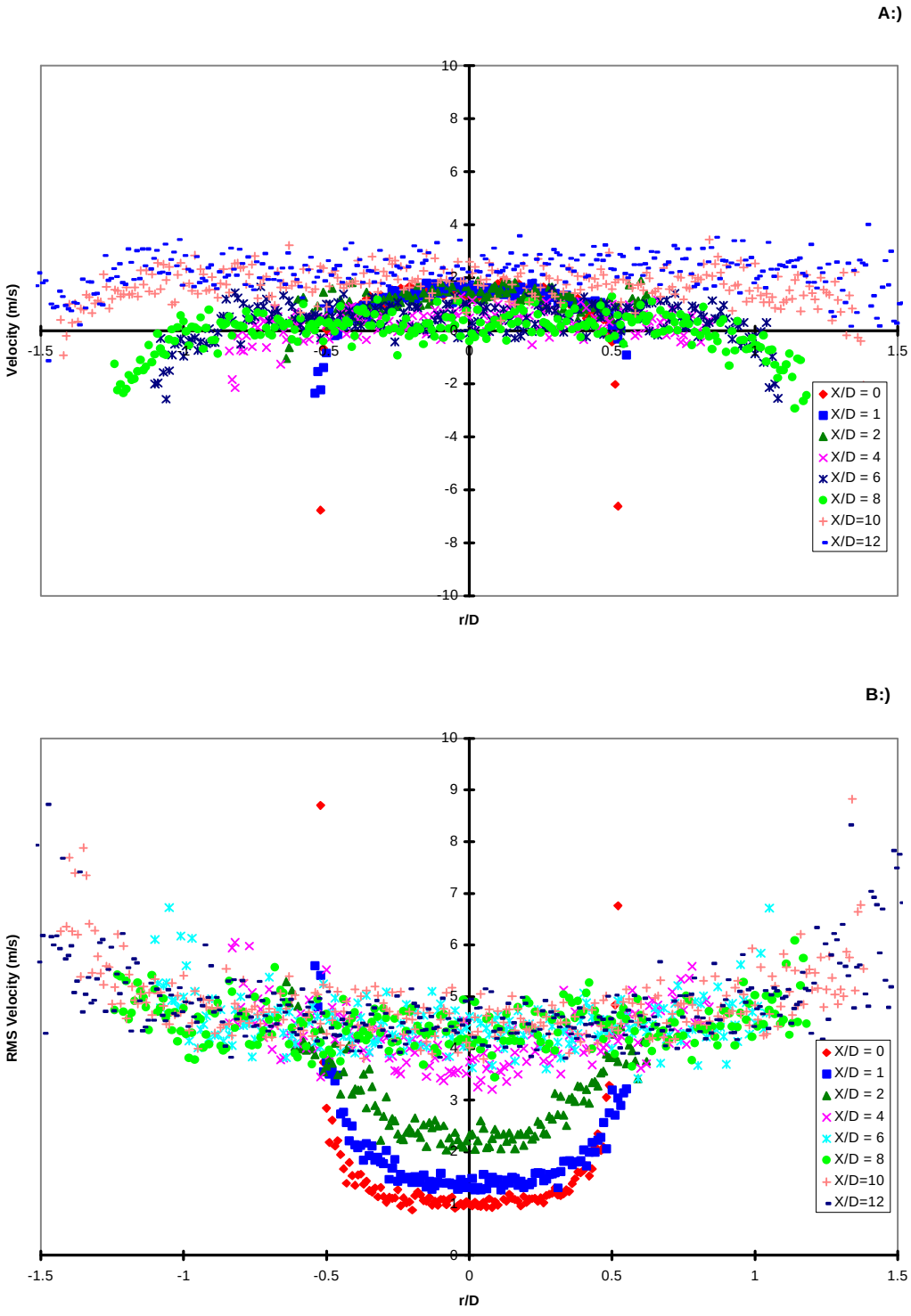

Figure 5.2. Circumferential composite results for standard jet, run 2
A.) Mean Velocities
B.) RMS Velocities

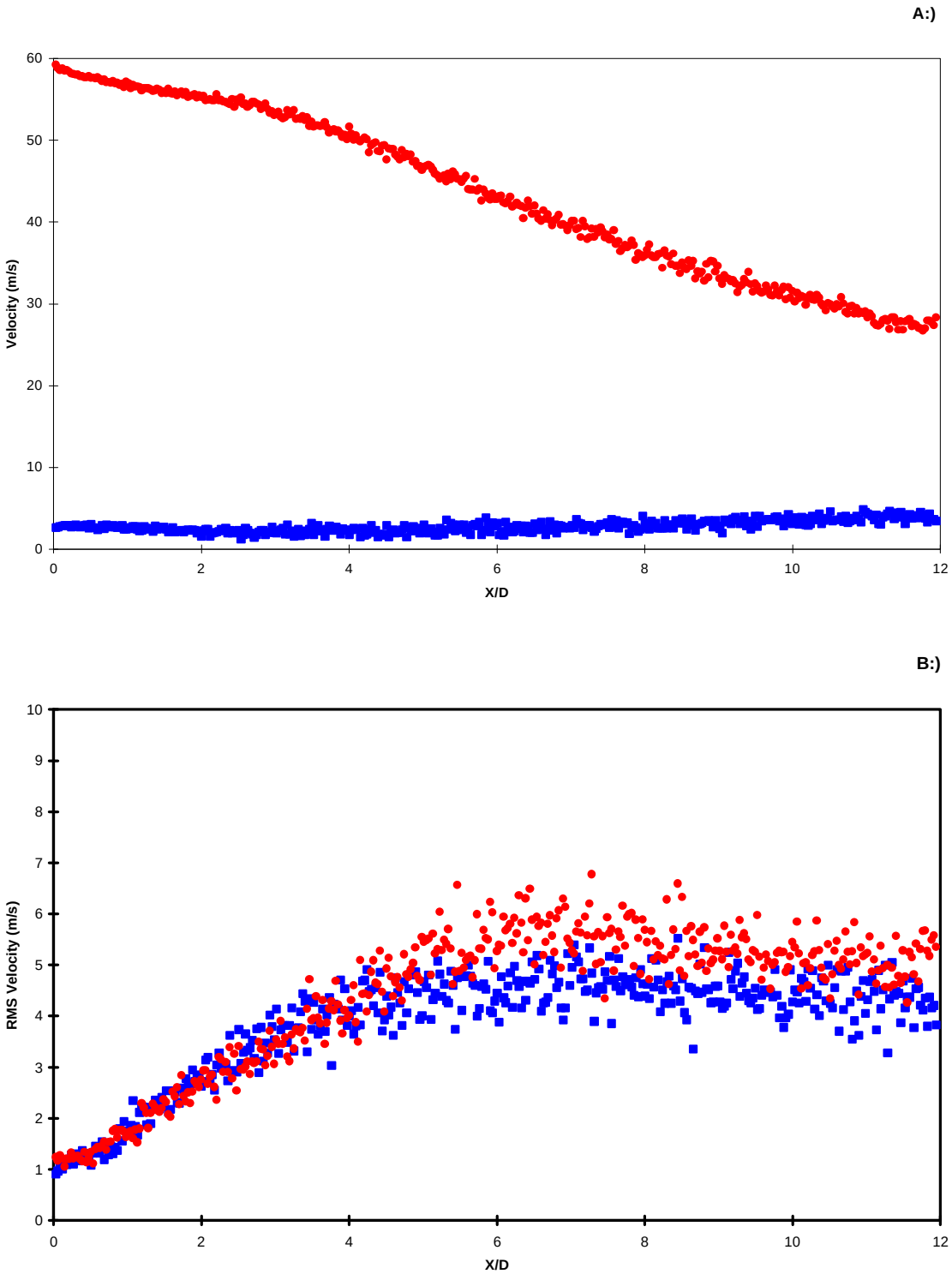

Figure 5.3. Standard jet centerline velocity profiles, run 2
Circles -axial velocity; Squares - circumferential velocity
A.) Mean Velocities
B.) RMS Velocities

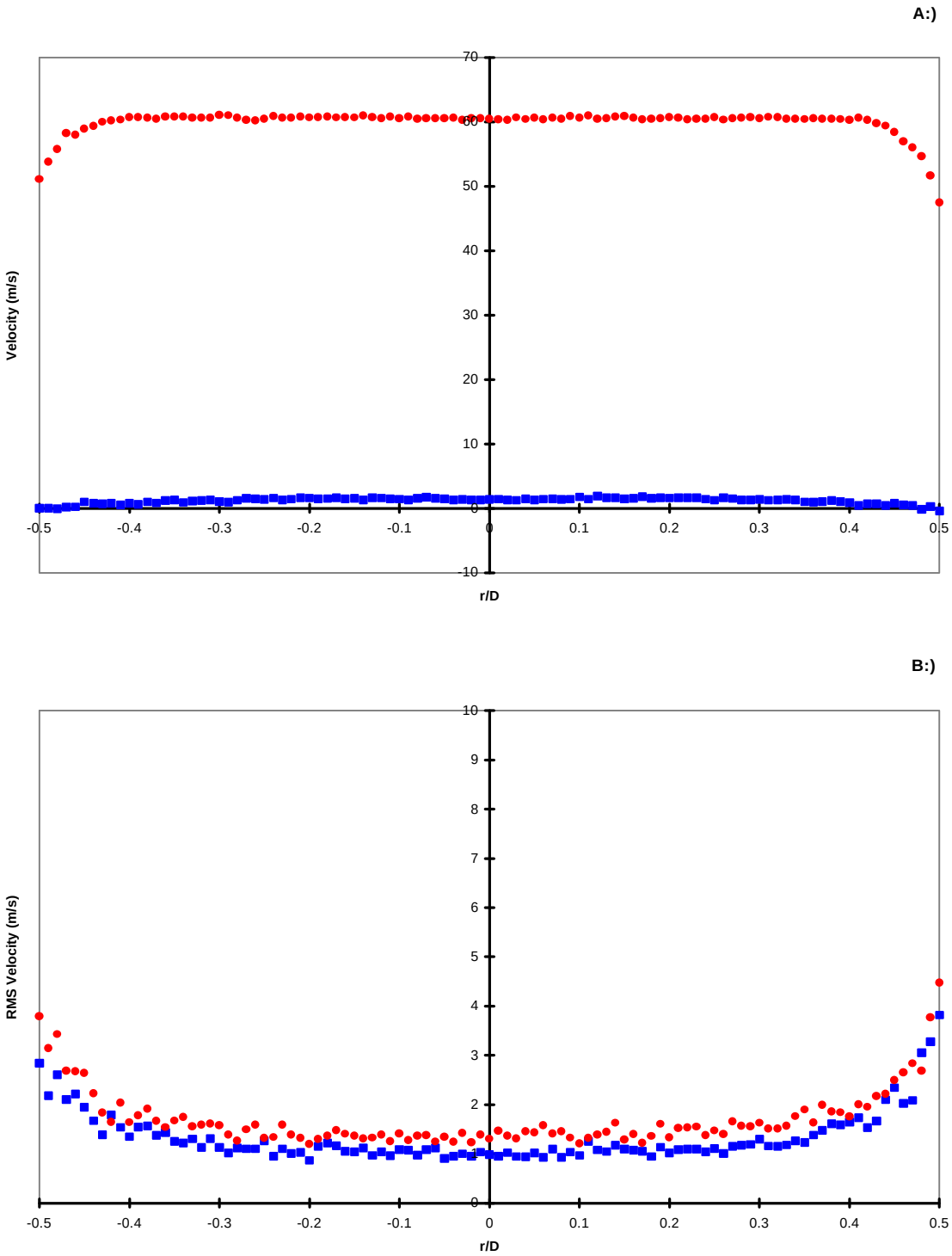

Figure 5.4. Radial cut of standard jet at X/D = 0.25
Circles -axial velocity; Squares -circumferential velocity
A.) Mean Velocities
B.) RMS Velocities

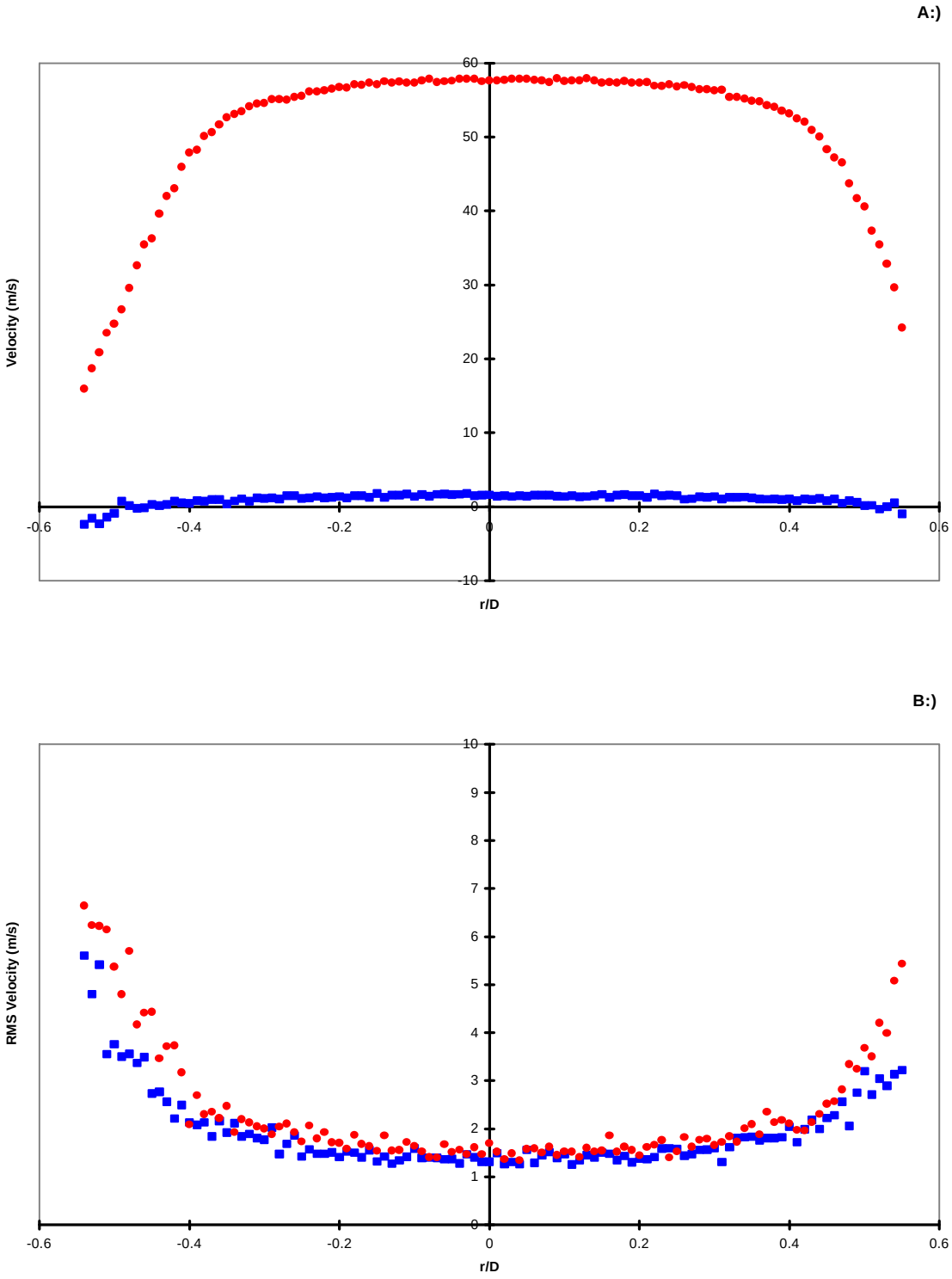

Figure 5.5. Radial cut of standard jet at X/D = 1
Circles -axial velocity; Squares -circumferential velocity
A.)Mean Velocities
B.) RMS Velocities

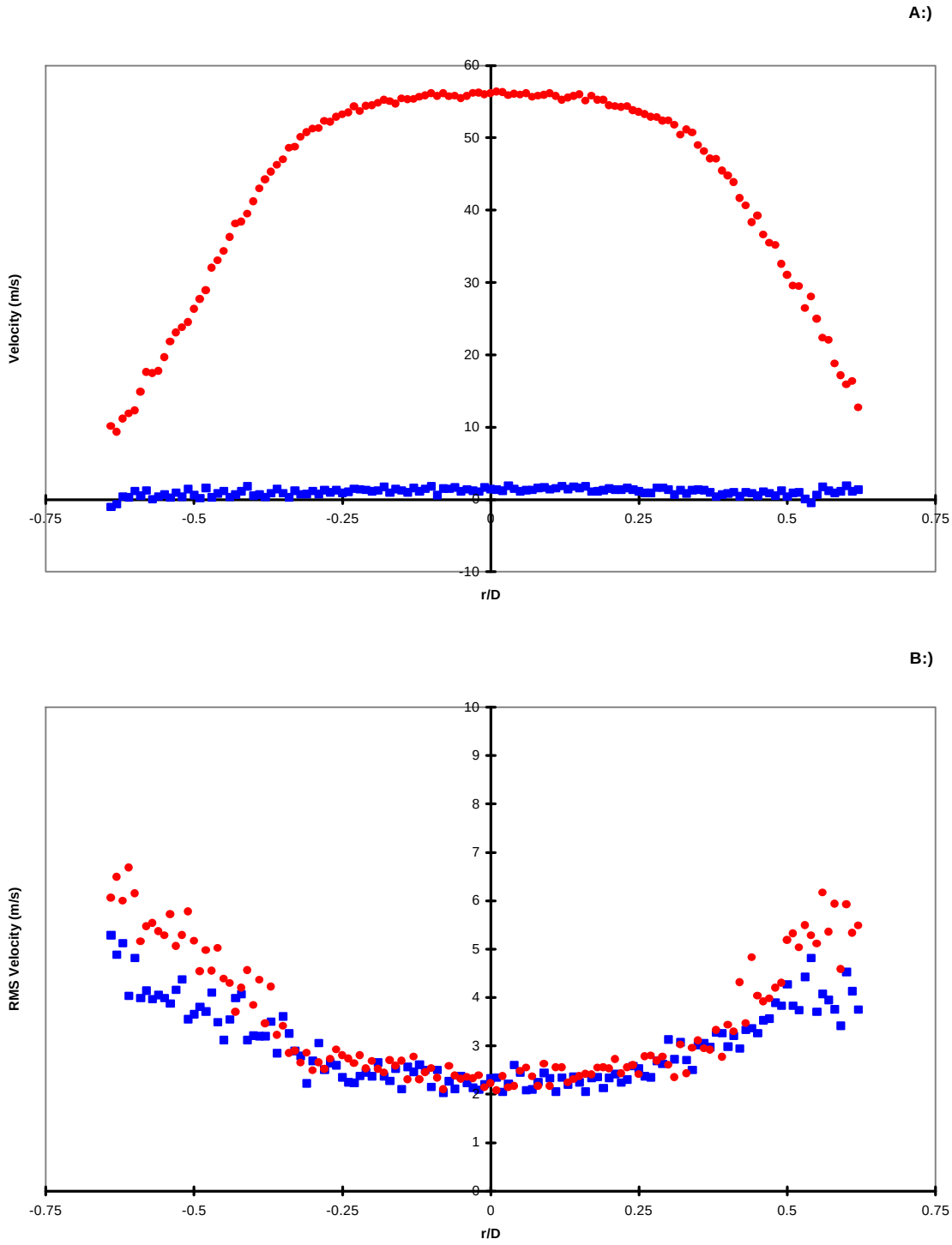

Figure 5.6. Radial cut of standard jet at X/D = 2
Circles -axial velocity; Squares -circumferential velocity
A.) Mean Velocities
B.) RMS Velocities

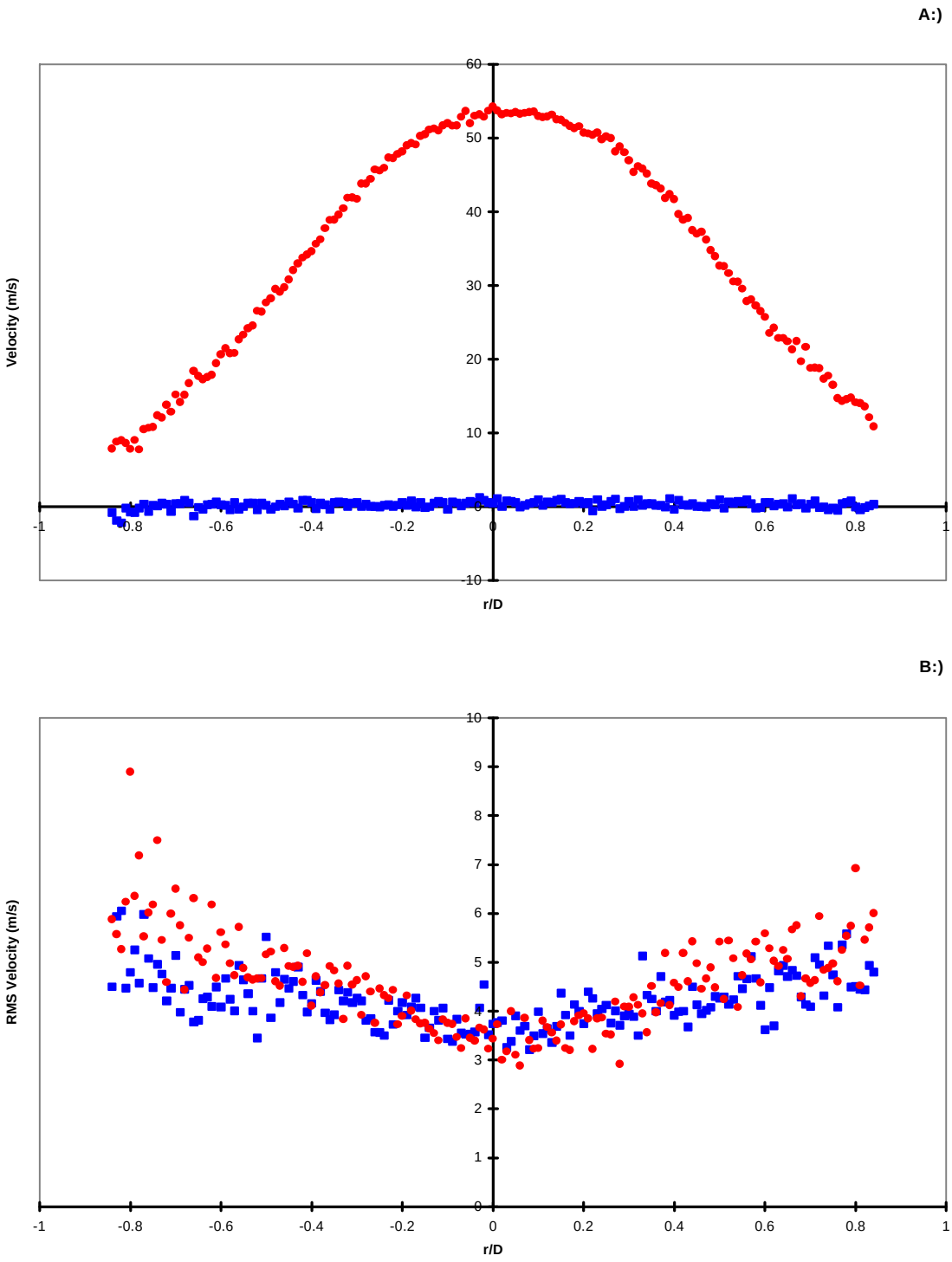

Figure 5.7. Radial cut of standard jet at X/D = 4
Circles -axial velocity; Squares -circumferential velocity
A.) Mean Velocities
B.) RMS Velocities

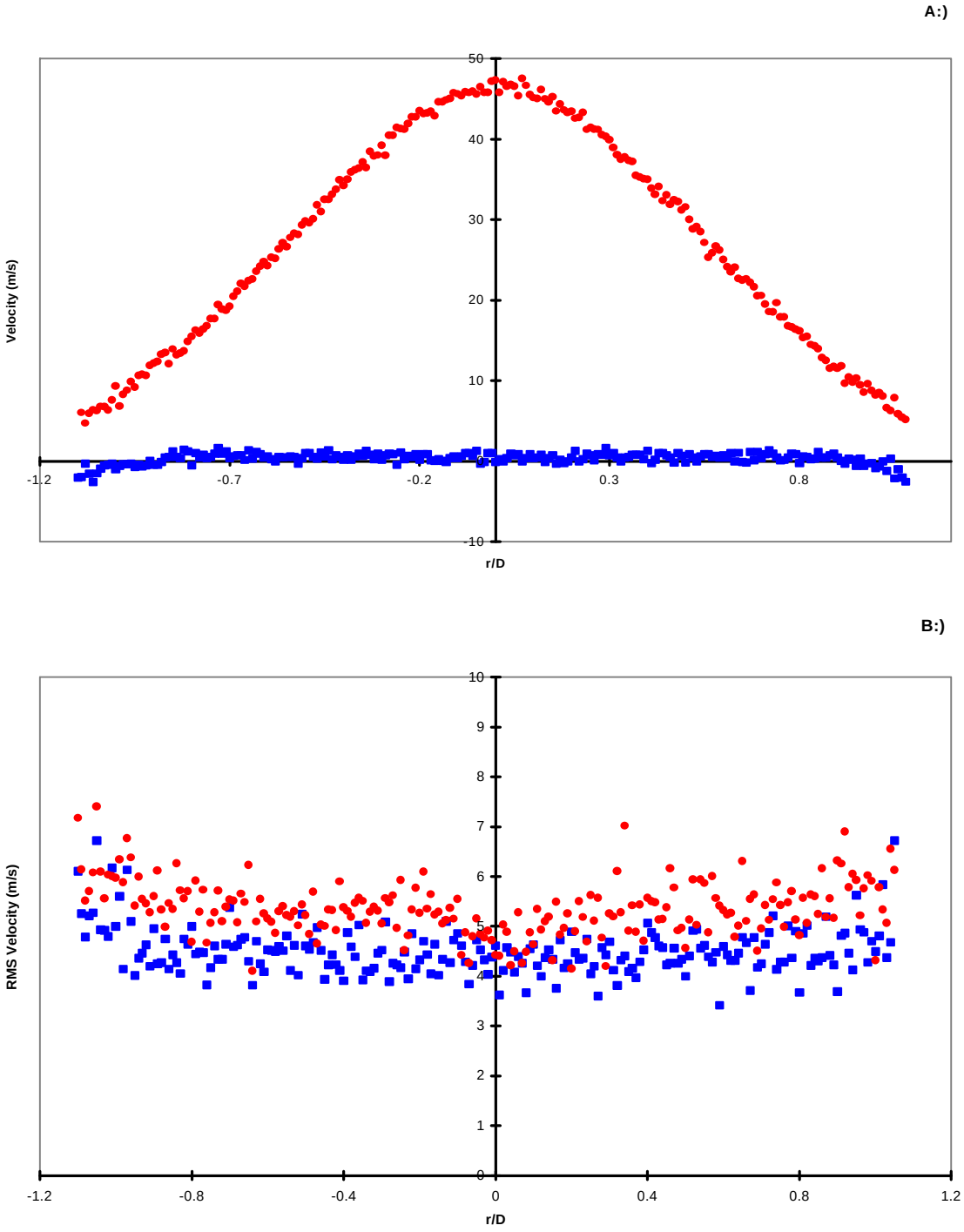

Figure 5.8. Radial cut of standard jet at X/D = 6
Circles -axial velocity; Squares -circumferential velocity
A.) Mean Velocities
B.) RMS Velocities

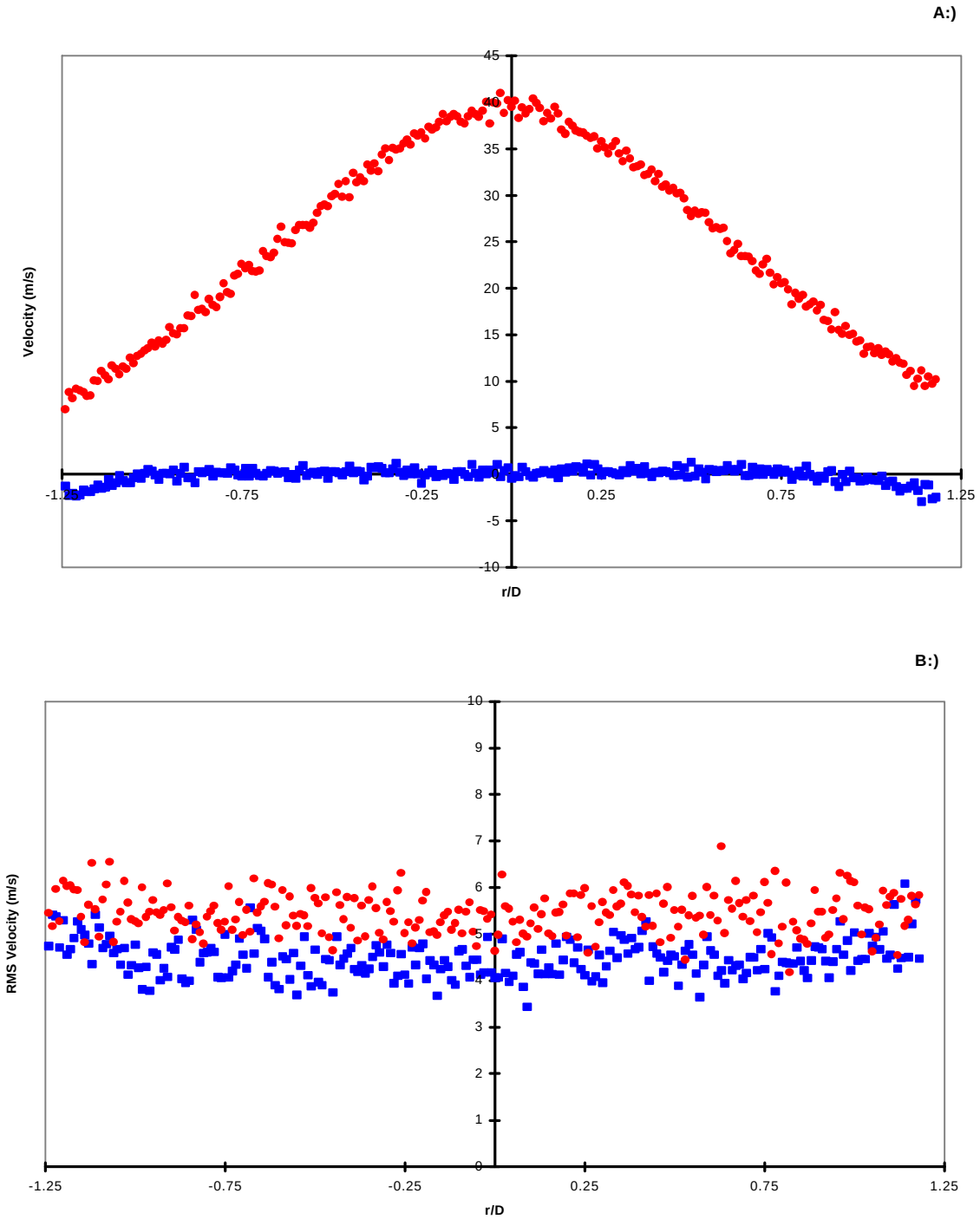

Figure 5.9. Radial cut of standard jet at X/D = 8
Circles -axial velocity; Squares -circumferential velocity
A.) Mean Velocities
B.) RMS Velocities

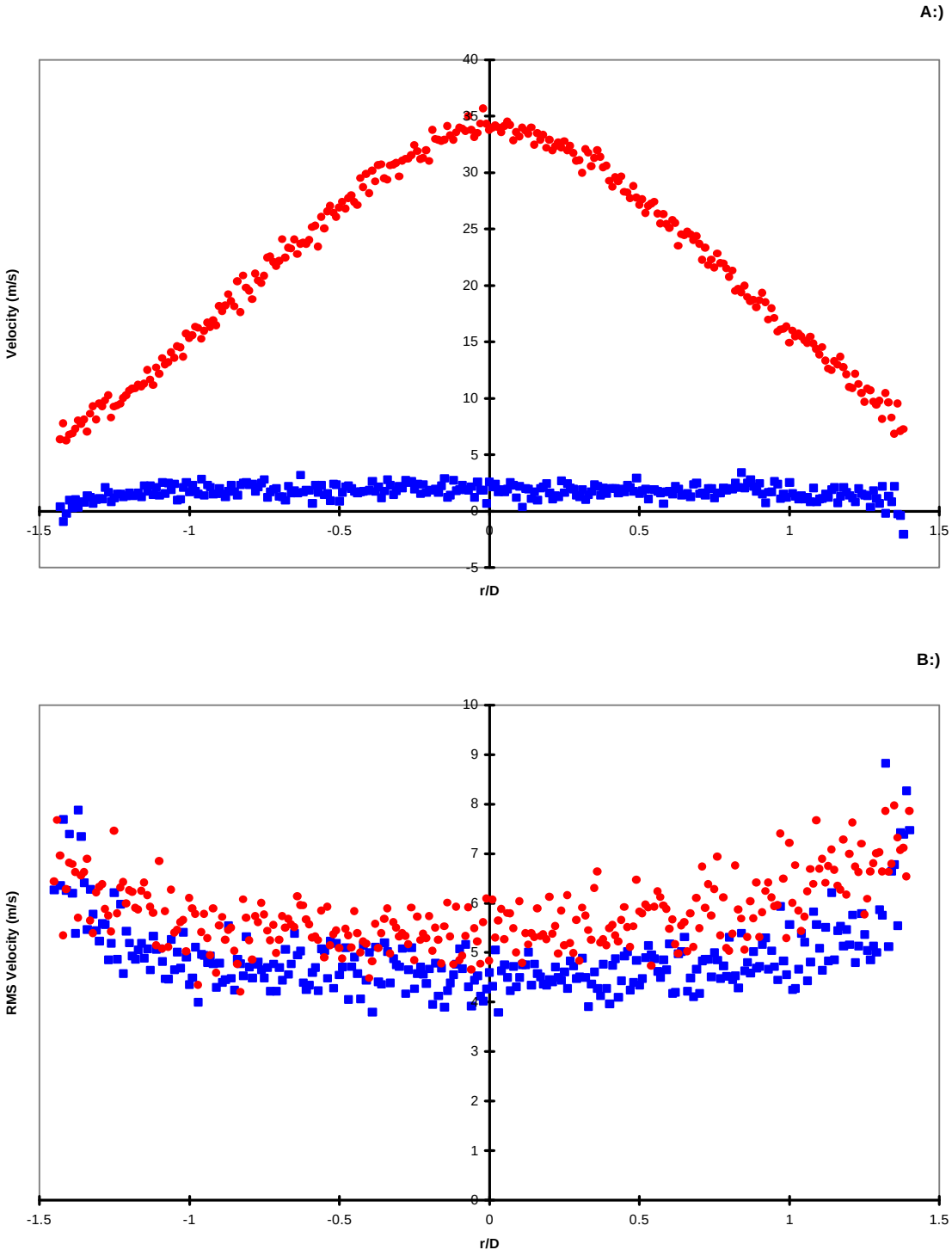

Figure 5.10. Radial cut of standard jet at X/D = 10
Circles -axial velocity; Squares -circumferential velocity
A.) Mean Velocities
B.) RMS Velocities

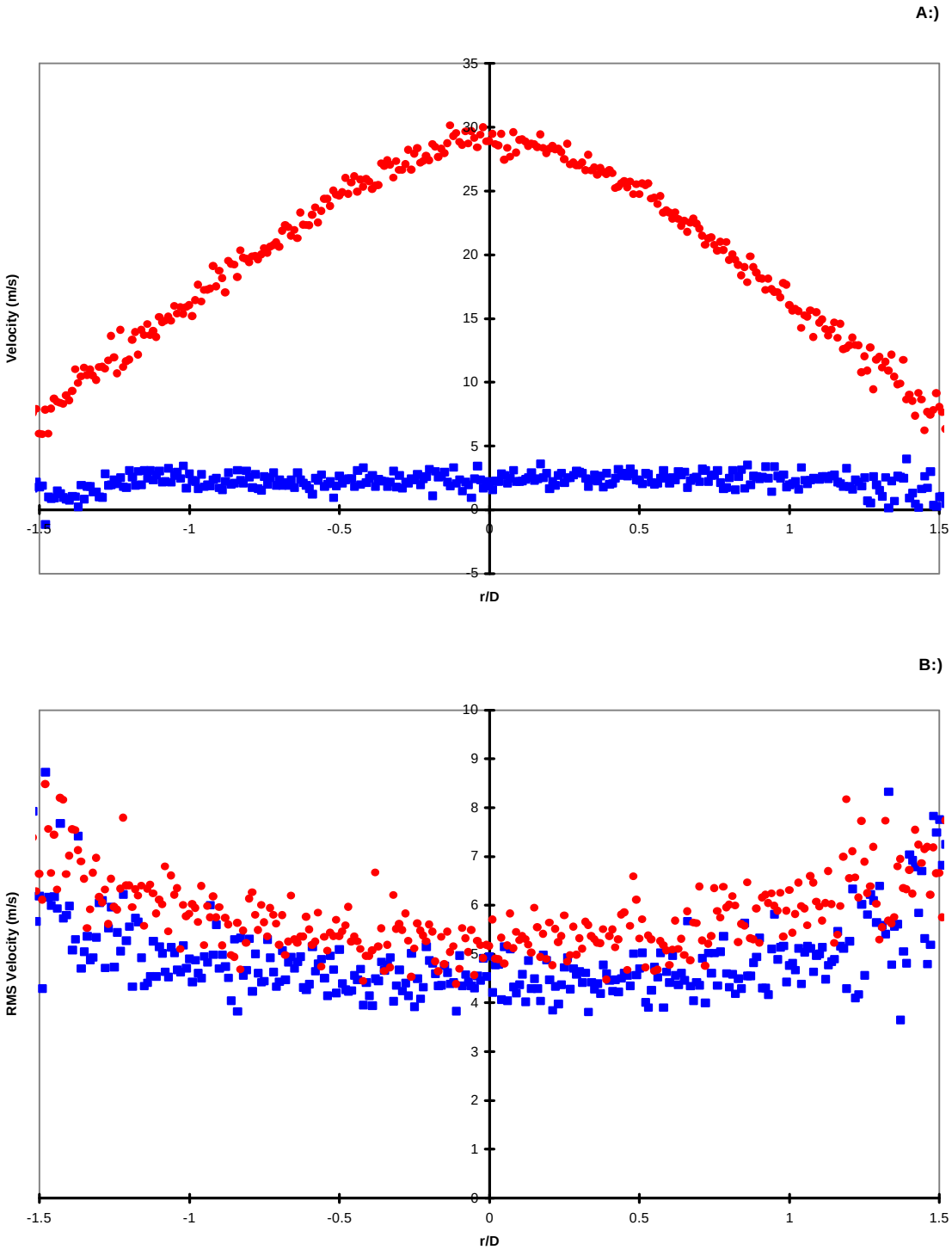

Figure 5.11. Radial cut of standard jet at X/D = 12
Circles -axial velocity; Squares -circumferential velocity
A.) Mean Velocities
B.) RMS Velocities

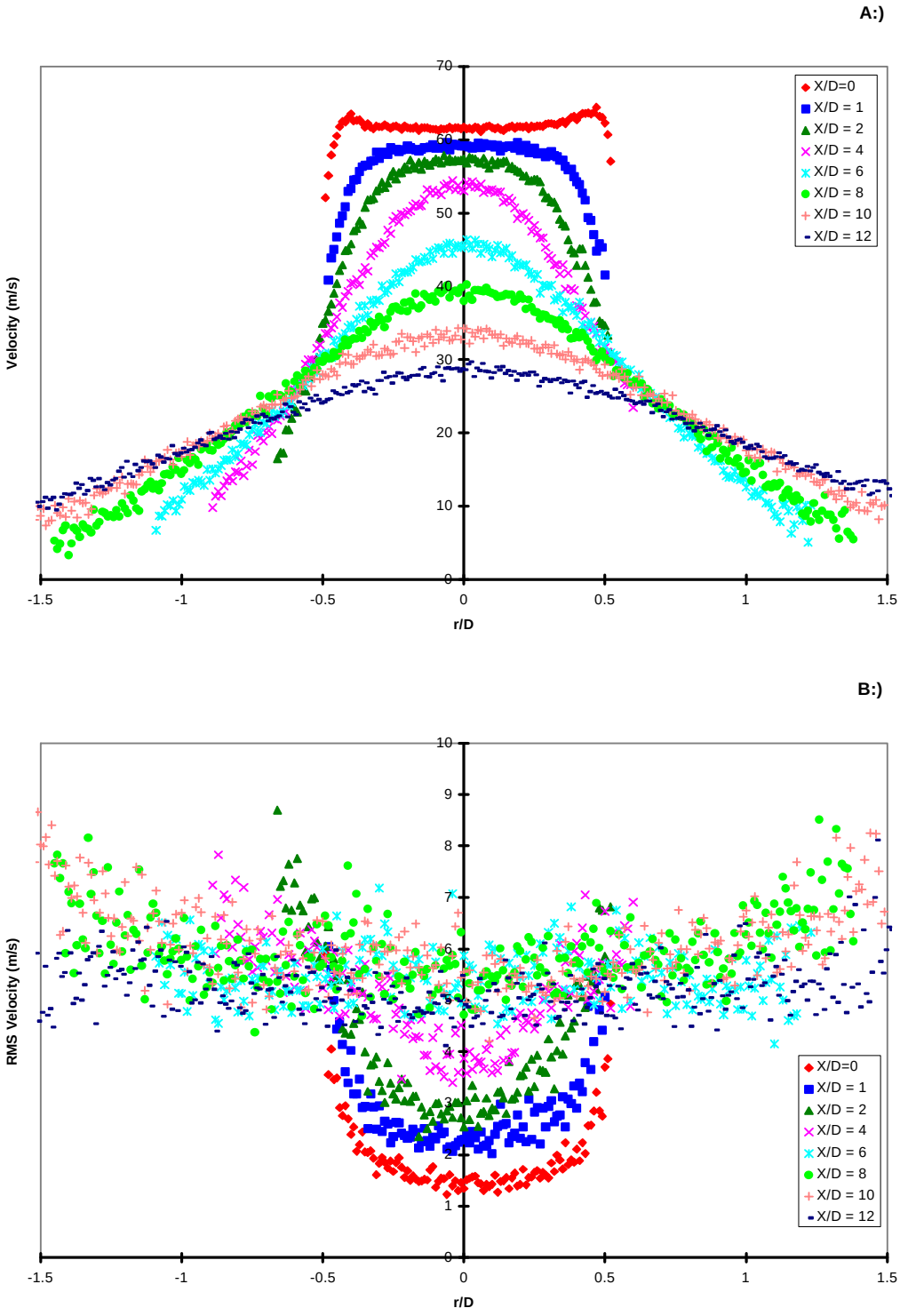

Figure 5.12. Axial composite results for standard jet, run 1
A.) Mean Velocities
B.) RMS Velocities

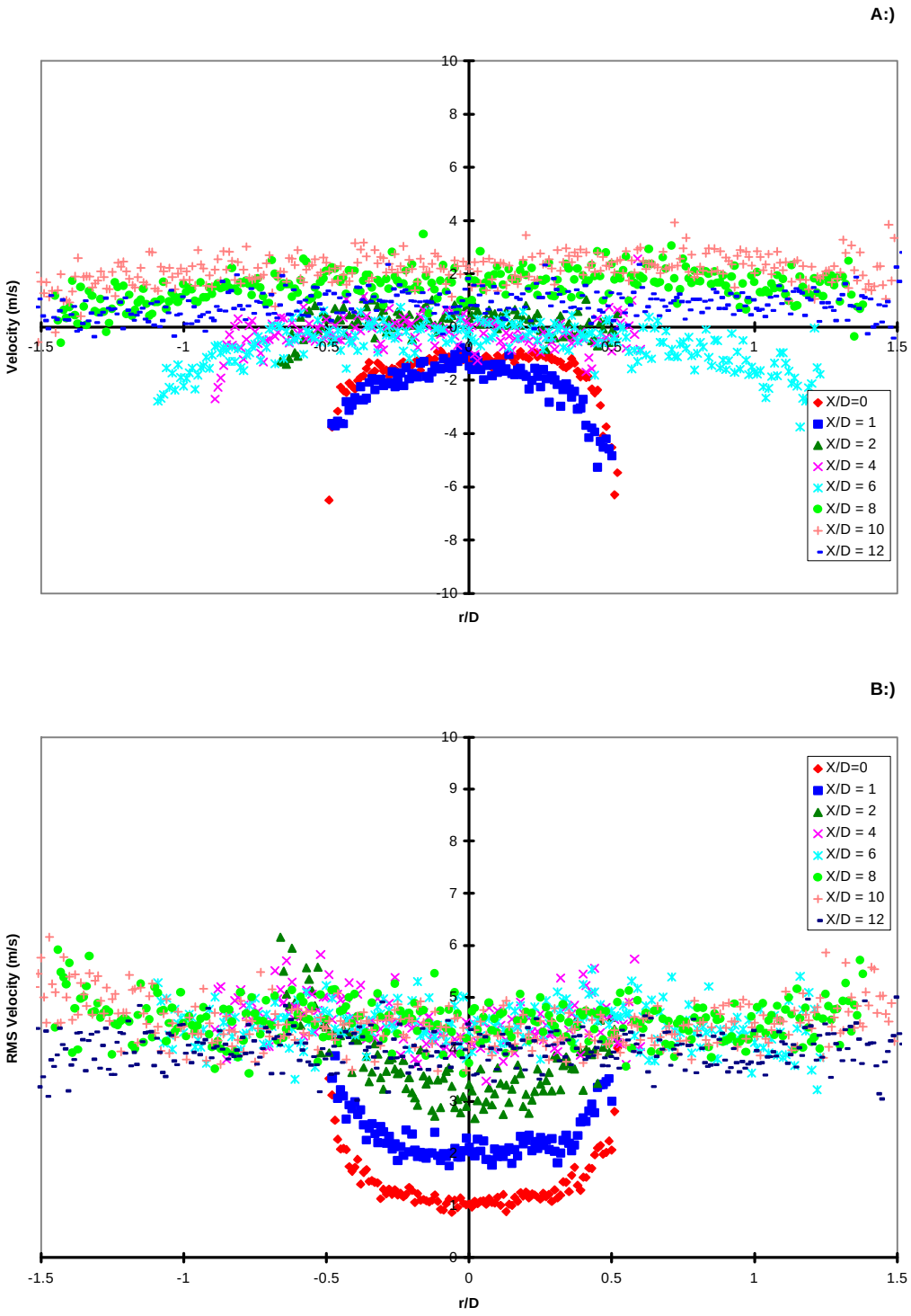

Figure 5.13. Circumferential composite results for standard jet, run 1
A.) Mean Velocities
B.) RMS Velocities

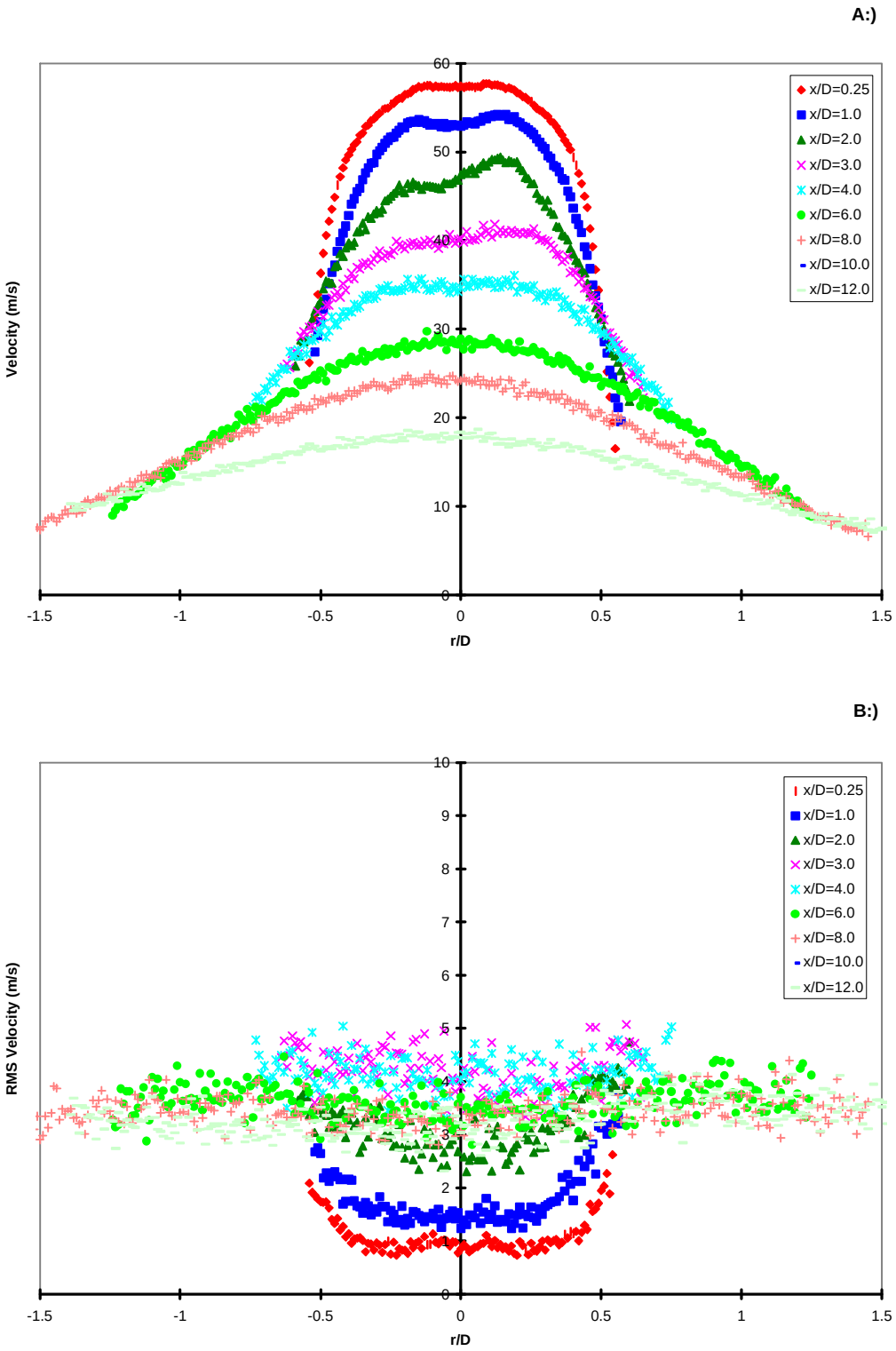

Figure 5.14. Axial composite results for swirling jet, run 1
A.) Mean Velocities
B.) RMS Velocities

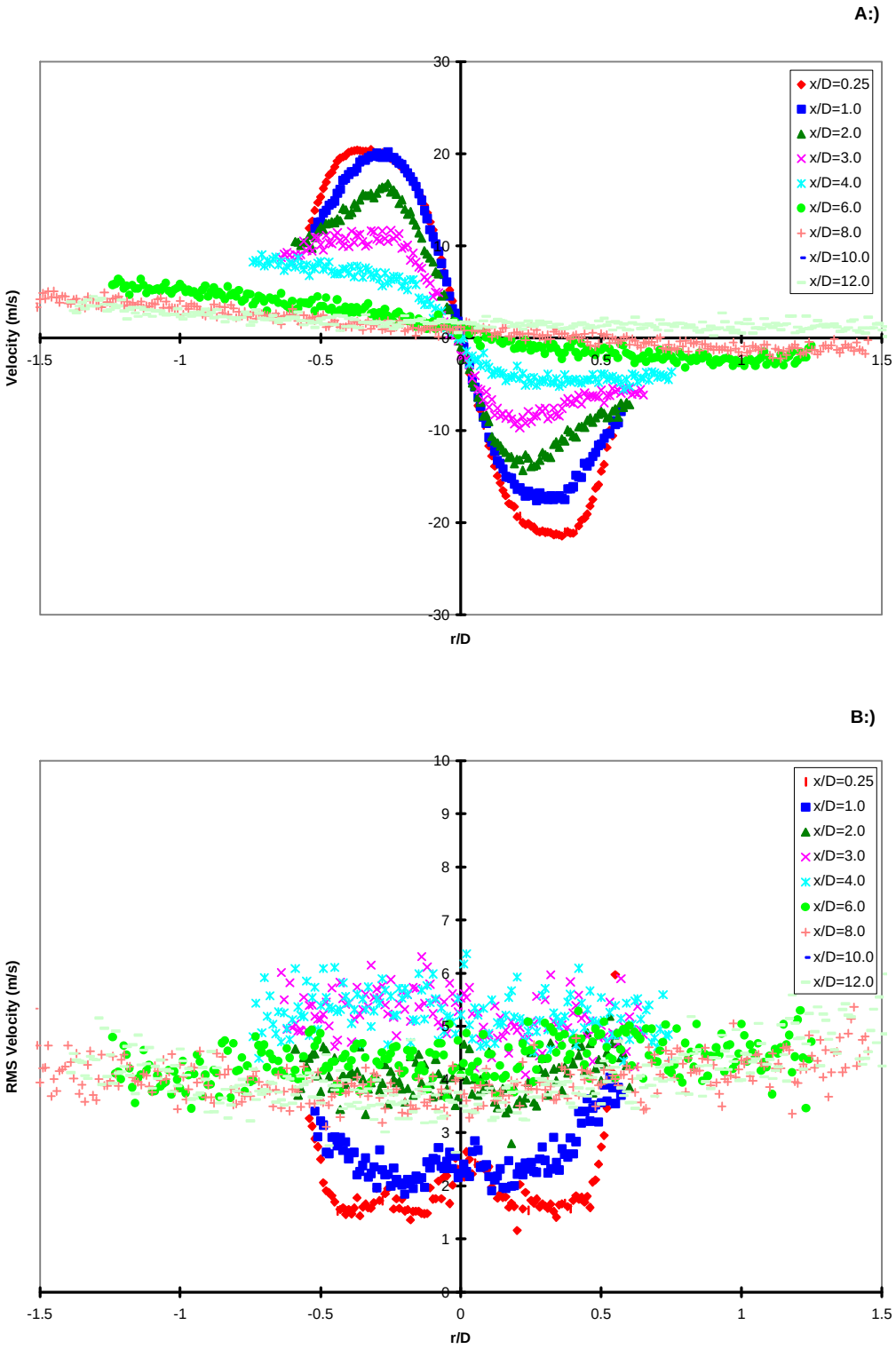

Figure 5.15. Circumferential composite results for swirling jet, run 1
A.) Mean Velocities
B.) RMS Velocities

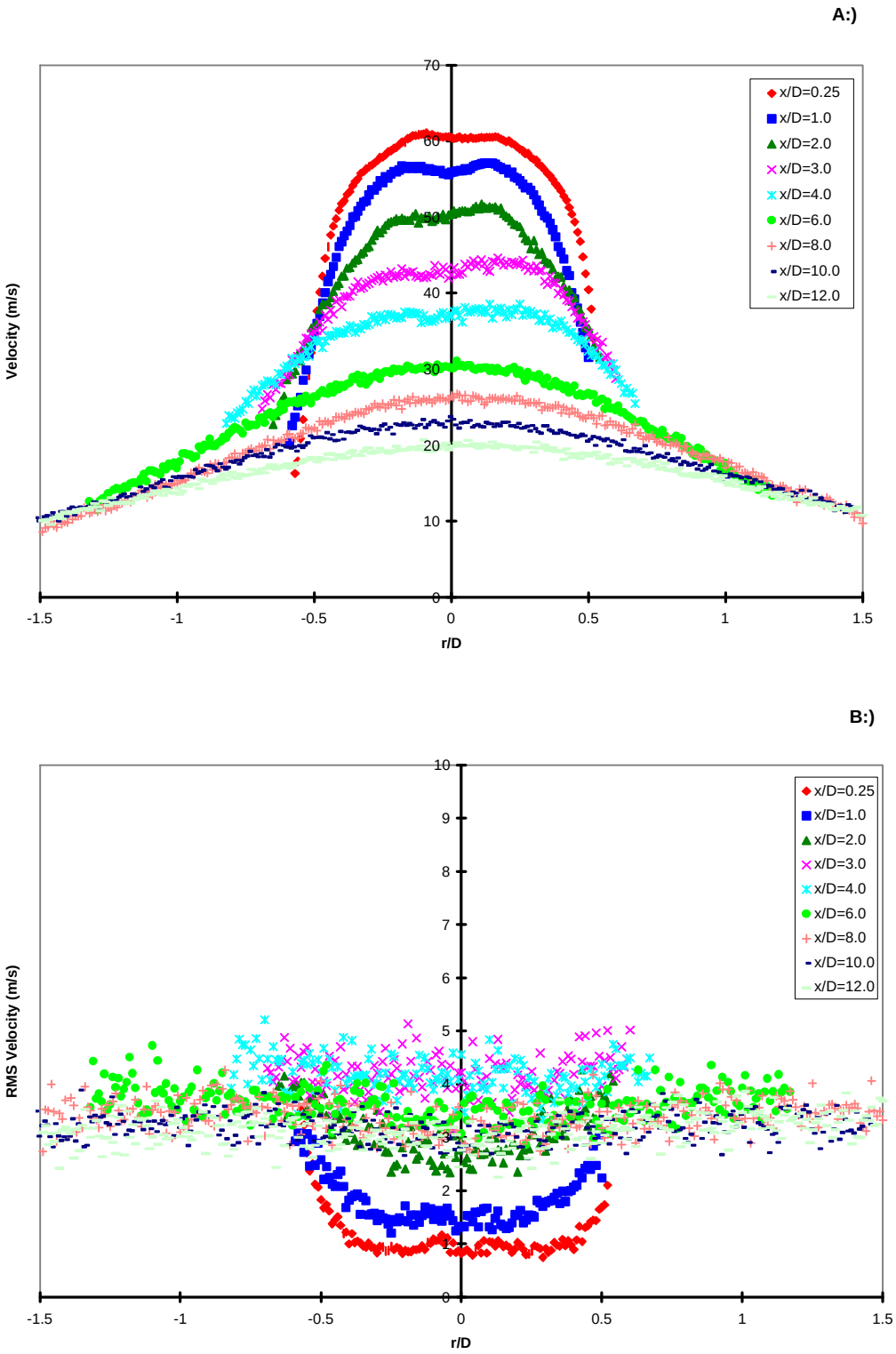

Figure 5.16. Axial composite results for swirling jet, run 2
A.) Mean Velocities
B.) RMS Velocities

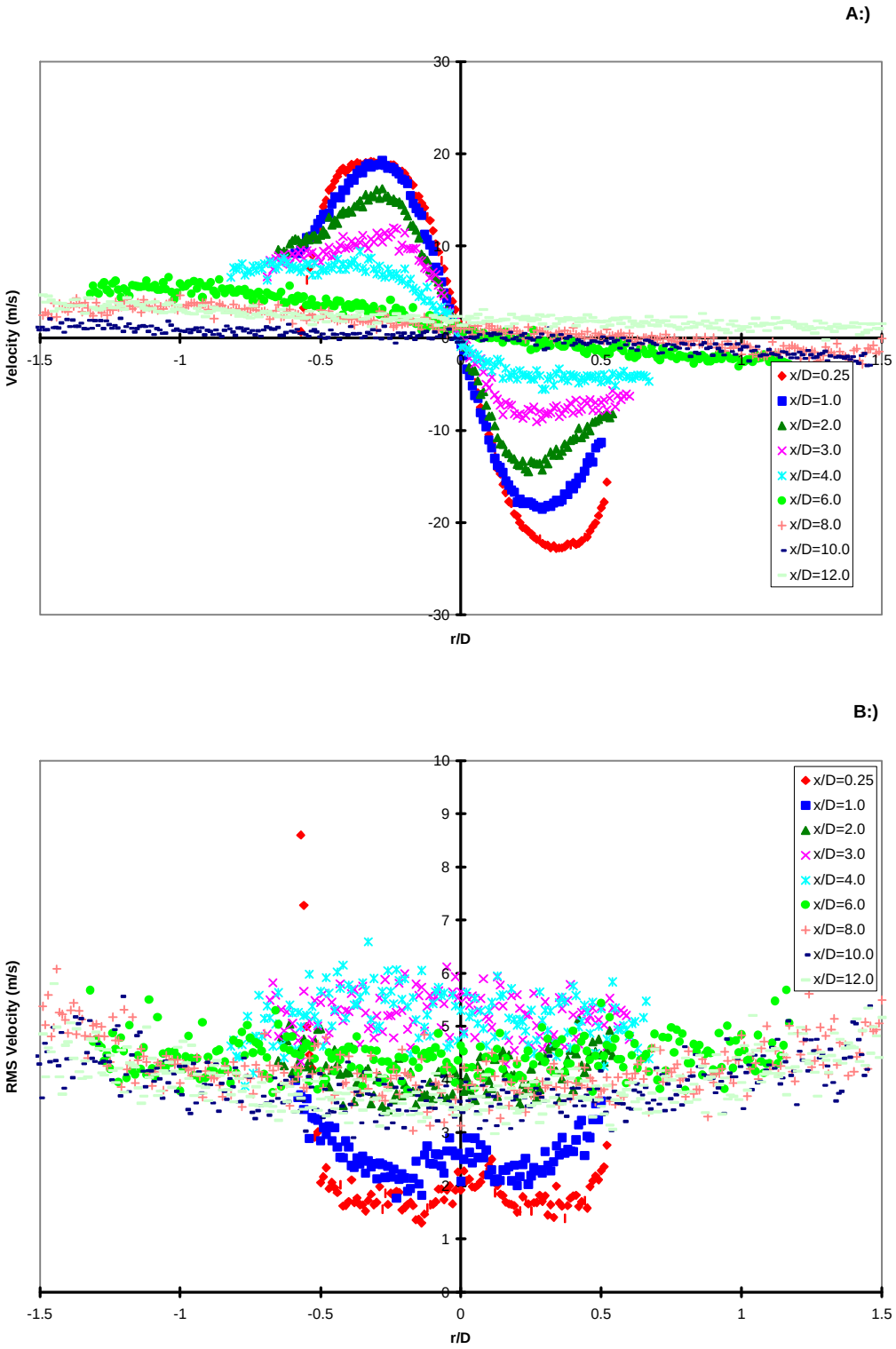

Figure 5.17. Circumferential composite results for swirling jet, run 2
A.) Mean Velocities
B.) RMS Velocities

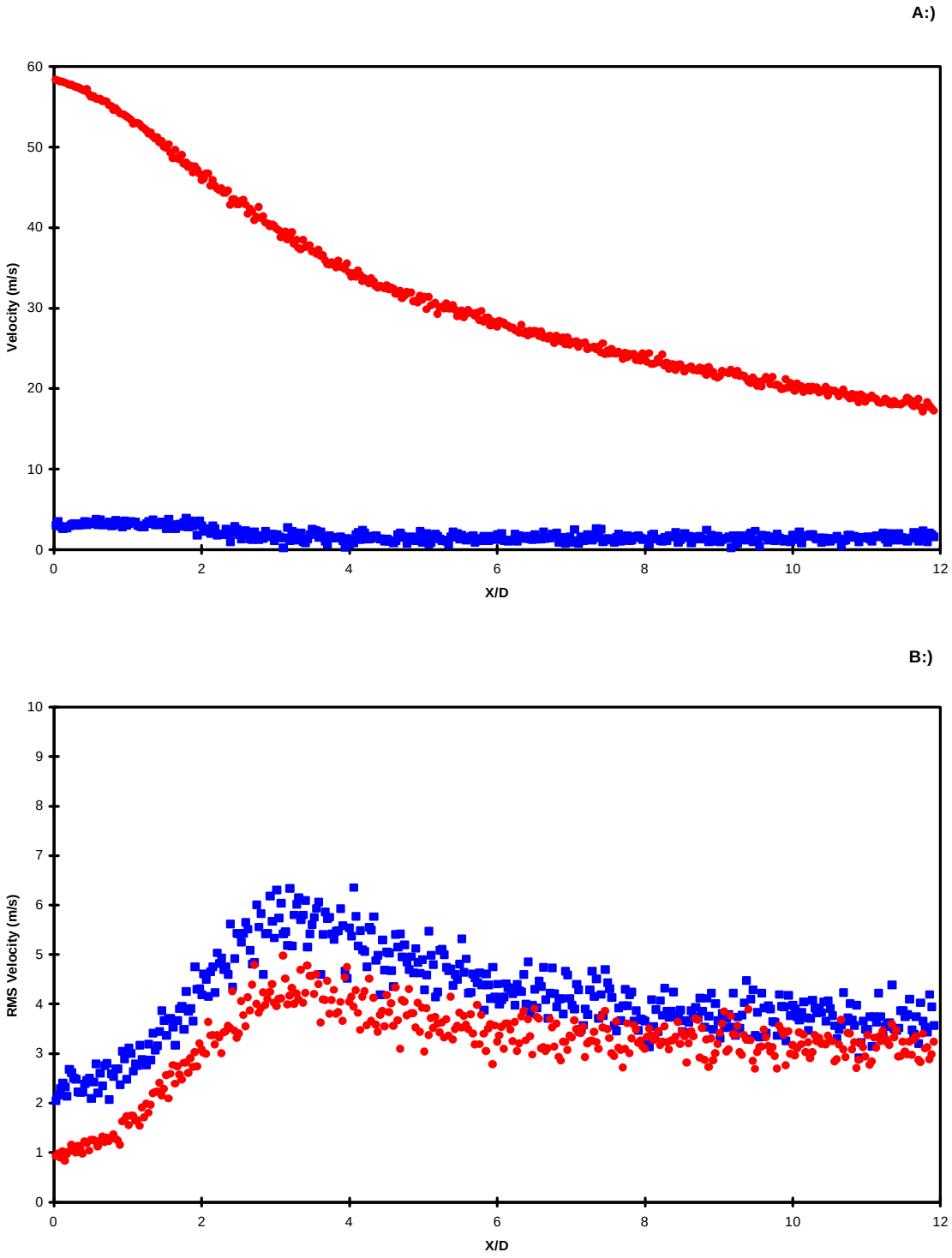

Figure 5.18. Swirling jet centerline velocity profiles, run 1
Circles -axial velocity; Squares - circumferential velocity
A.) Mean Velocities
B.) RMS Velocities

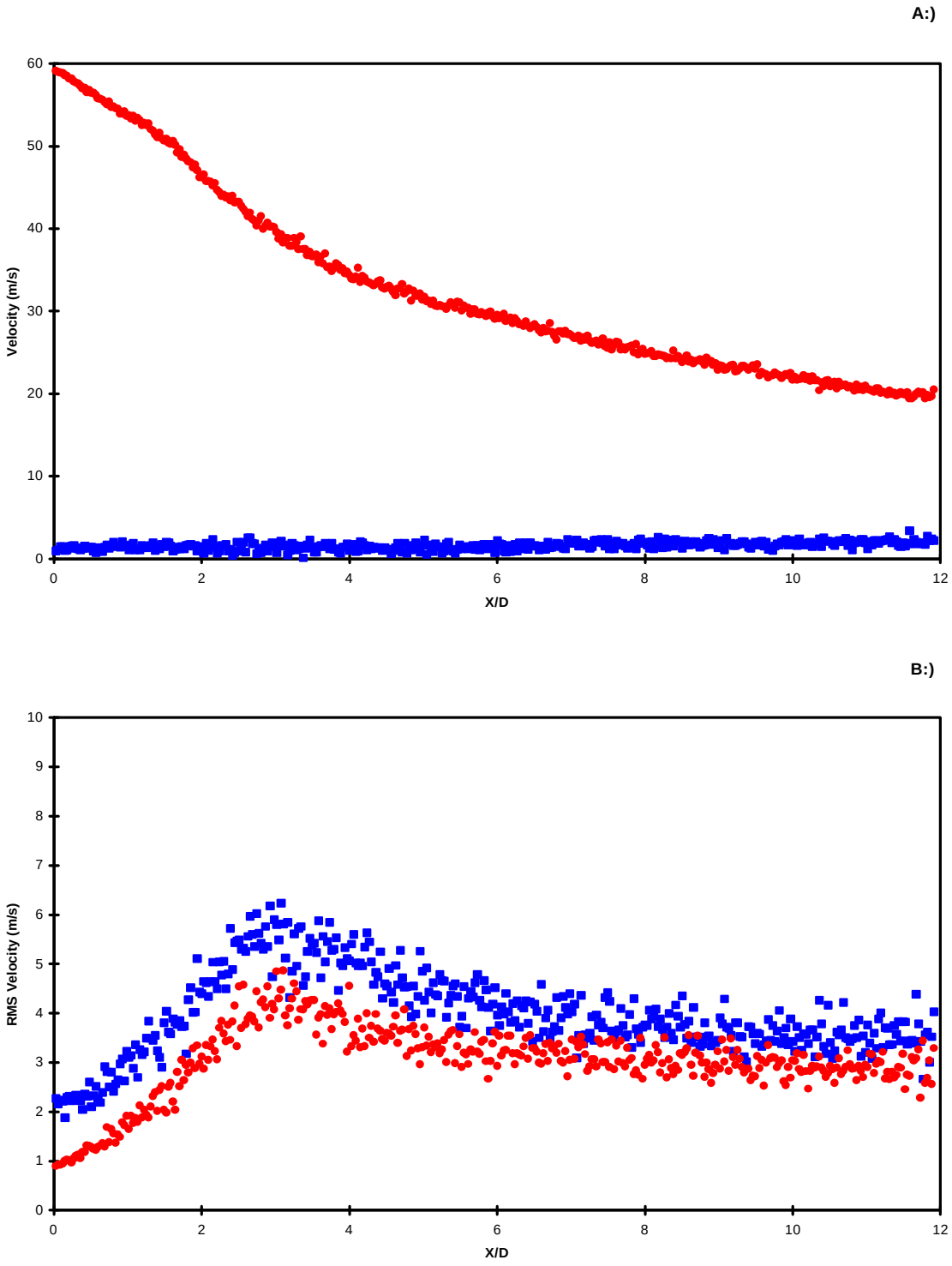

Figure 5.19. Swirling jet centerline velocity profiles, run 2
Circles -axial velocity; Squares - circumferential velocity
A.) Mean Velocities
B.) RMS Velocities

A:)

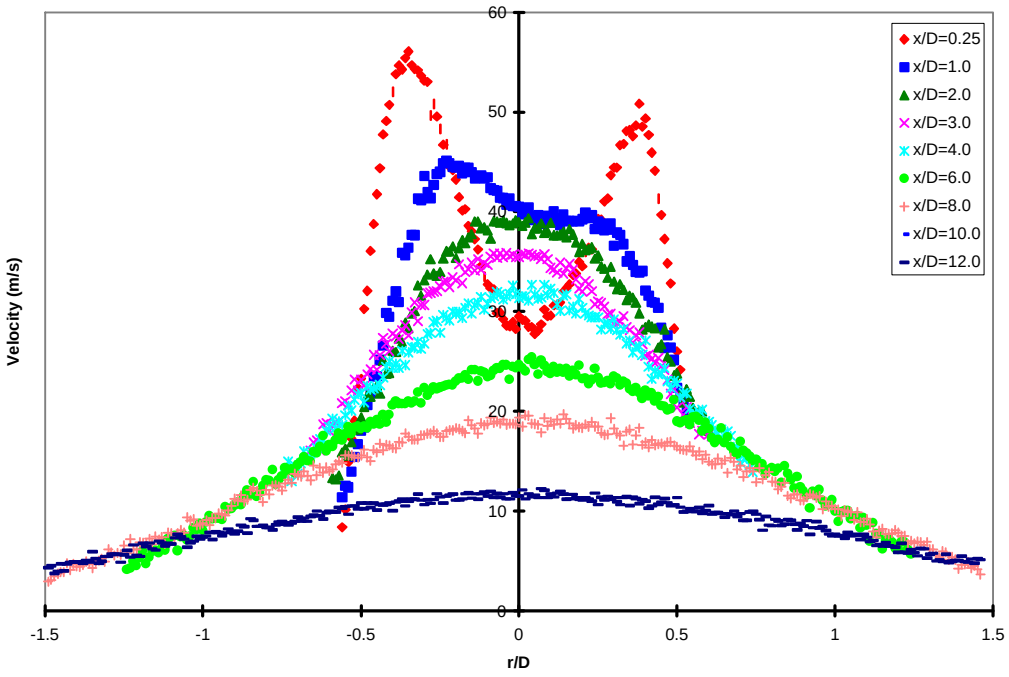

B:)

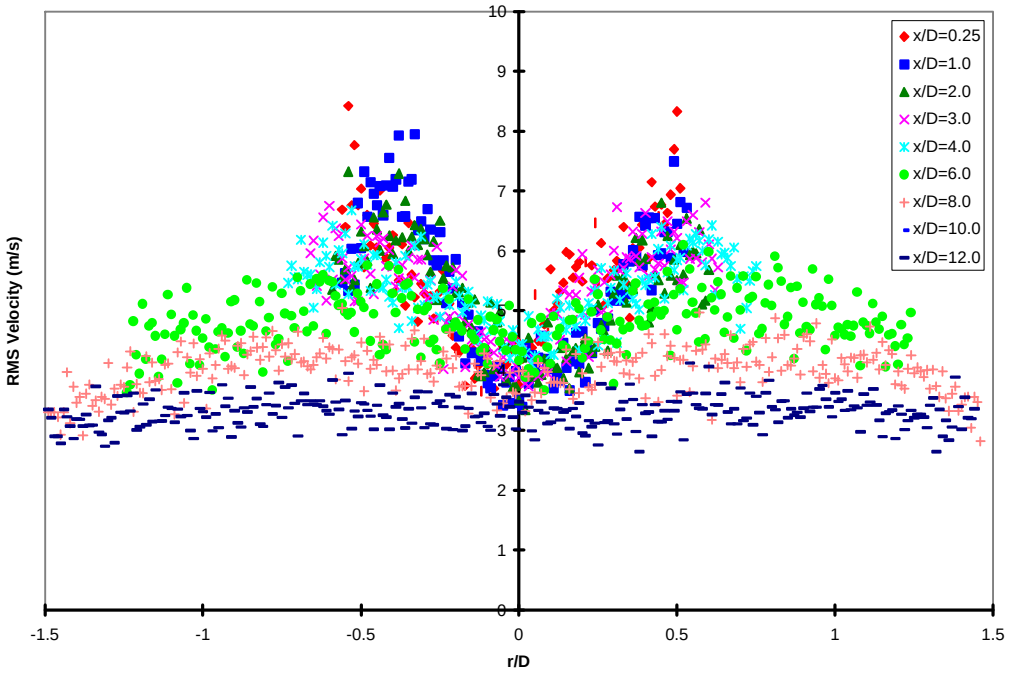

Figure 5.20. Axial composite results for annular jet, run 1
A.) Mean Velocities
B.) RMS Velocities

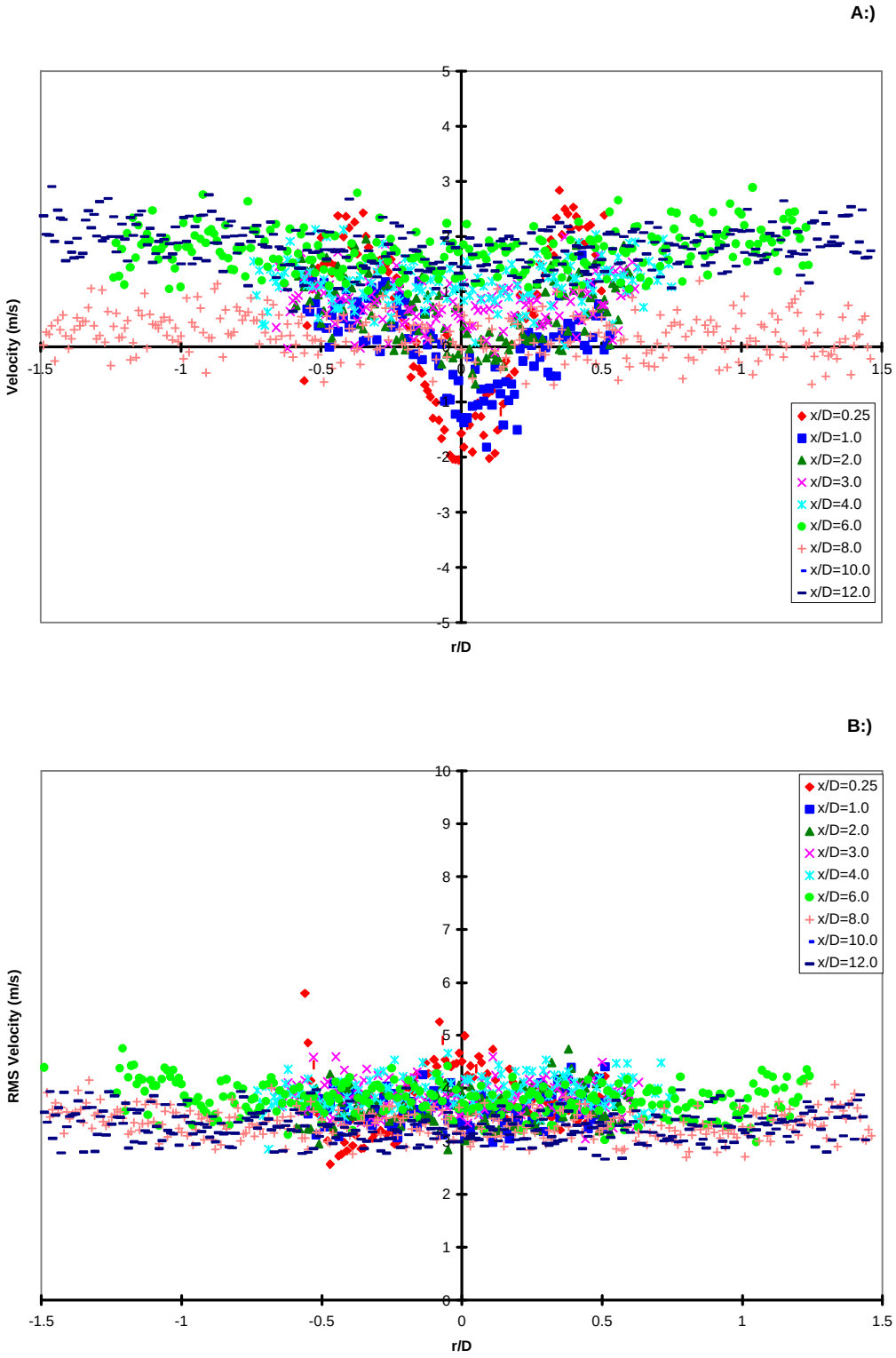

Figure 5.21. Circumferential composite results for annular jet, run 1
A.) Mean Velocities
B.) RMS Velocities

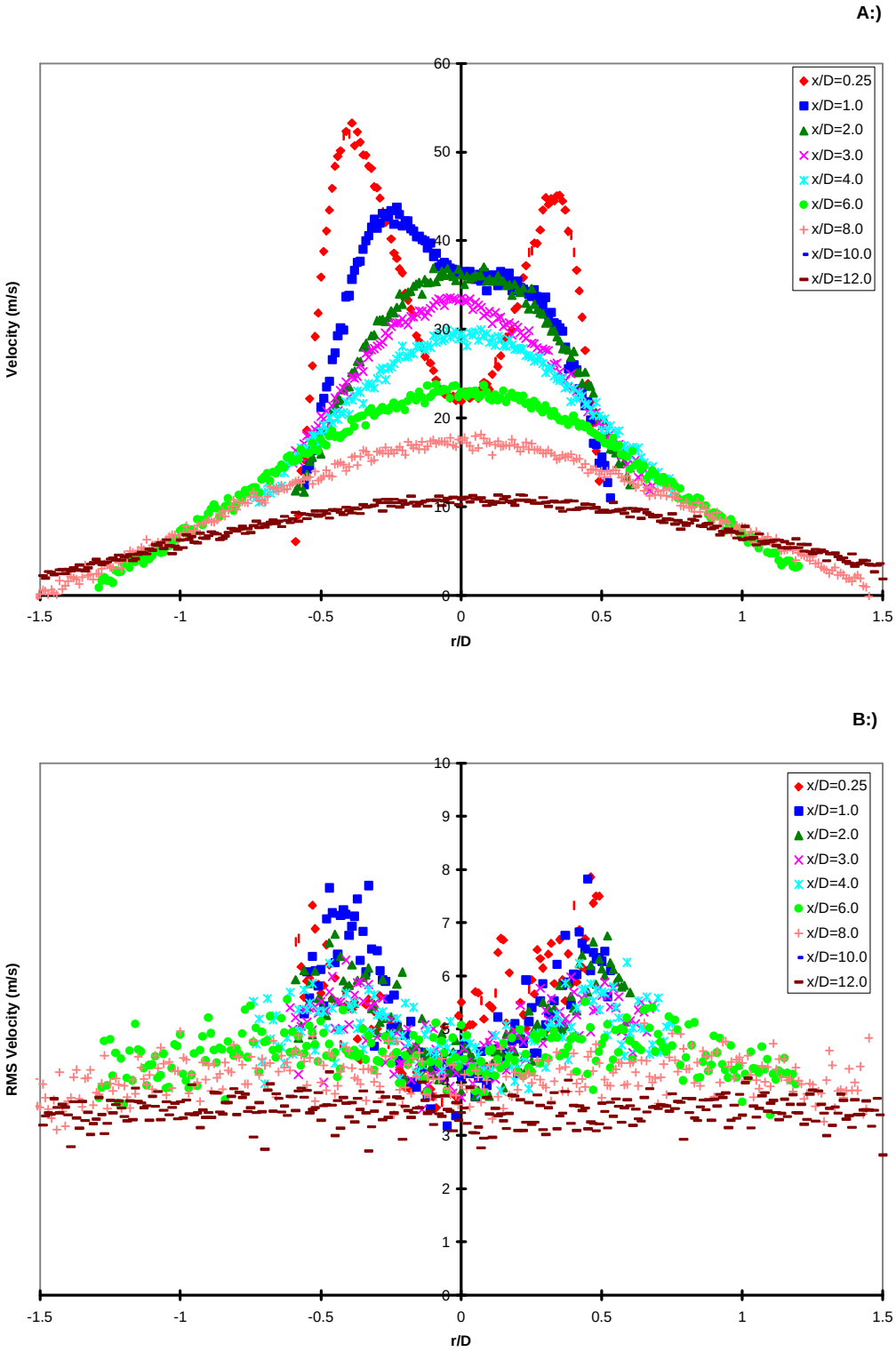

Figure 5.22. Axial composite results for annular jet, run 2
A.) Mean Velocities
B.) RMS Velocities

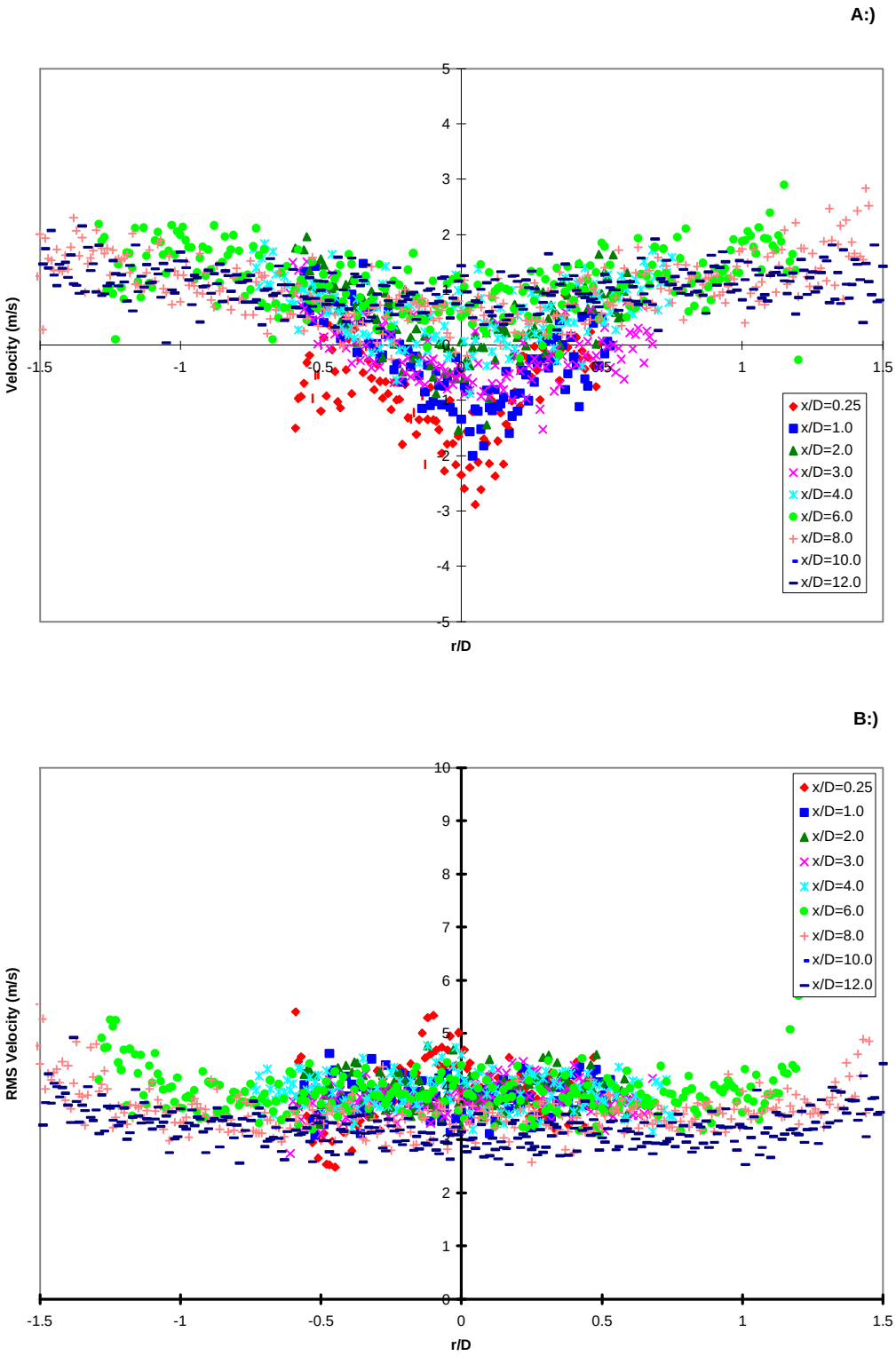

Figure 5.23. Circumferential composite results for annular jet, run 2
A.) Mean Velocities
B.) RMS Velocities

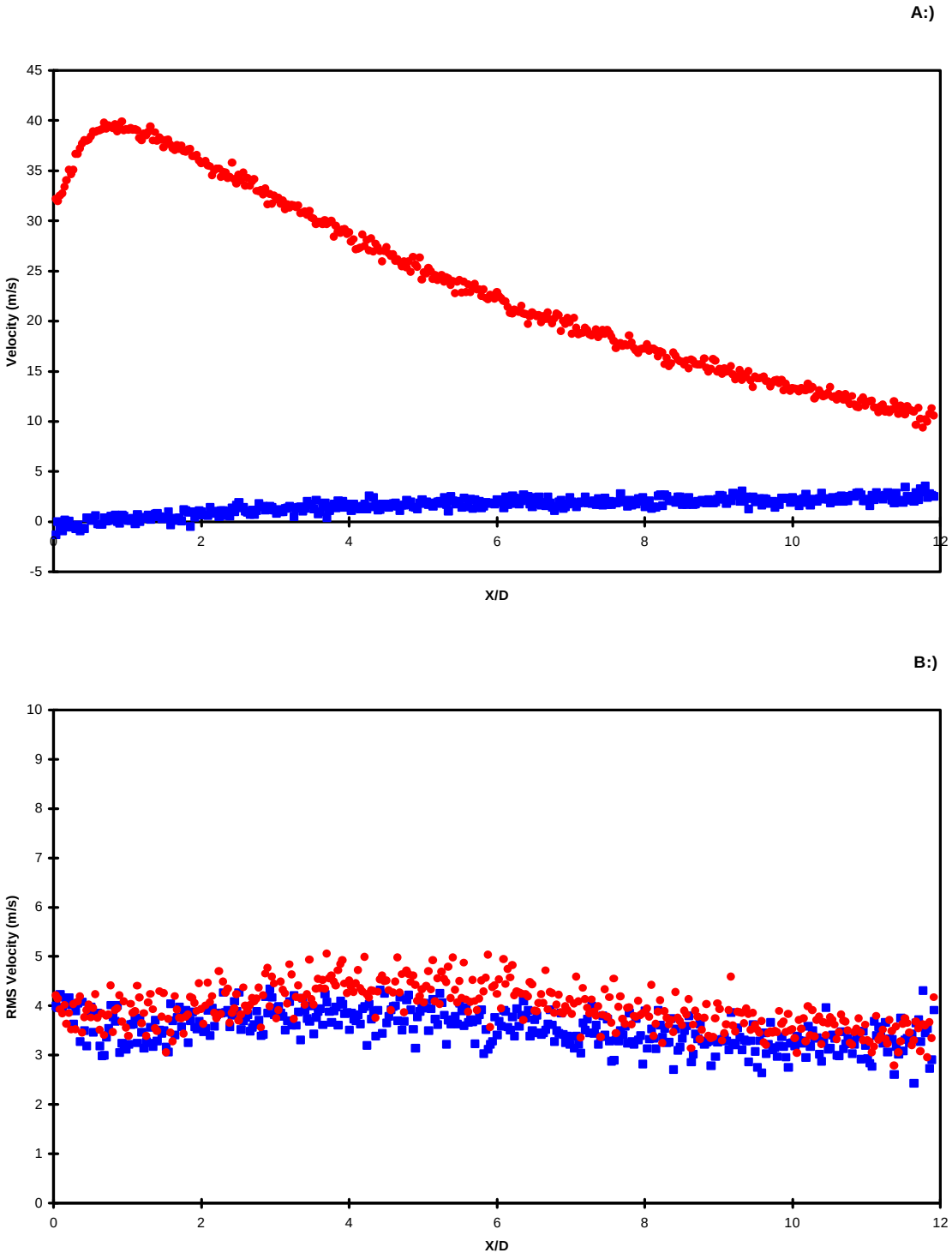

Figure 5.24. Annular jet centerline velocity profiles, run 1
Circles -axial velocity; Squares - circumferential velocity
A.) Mean Velocities
B.) RMS Velocities

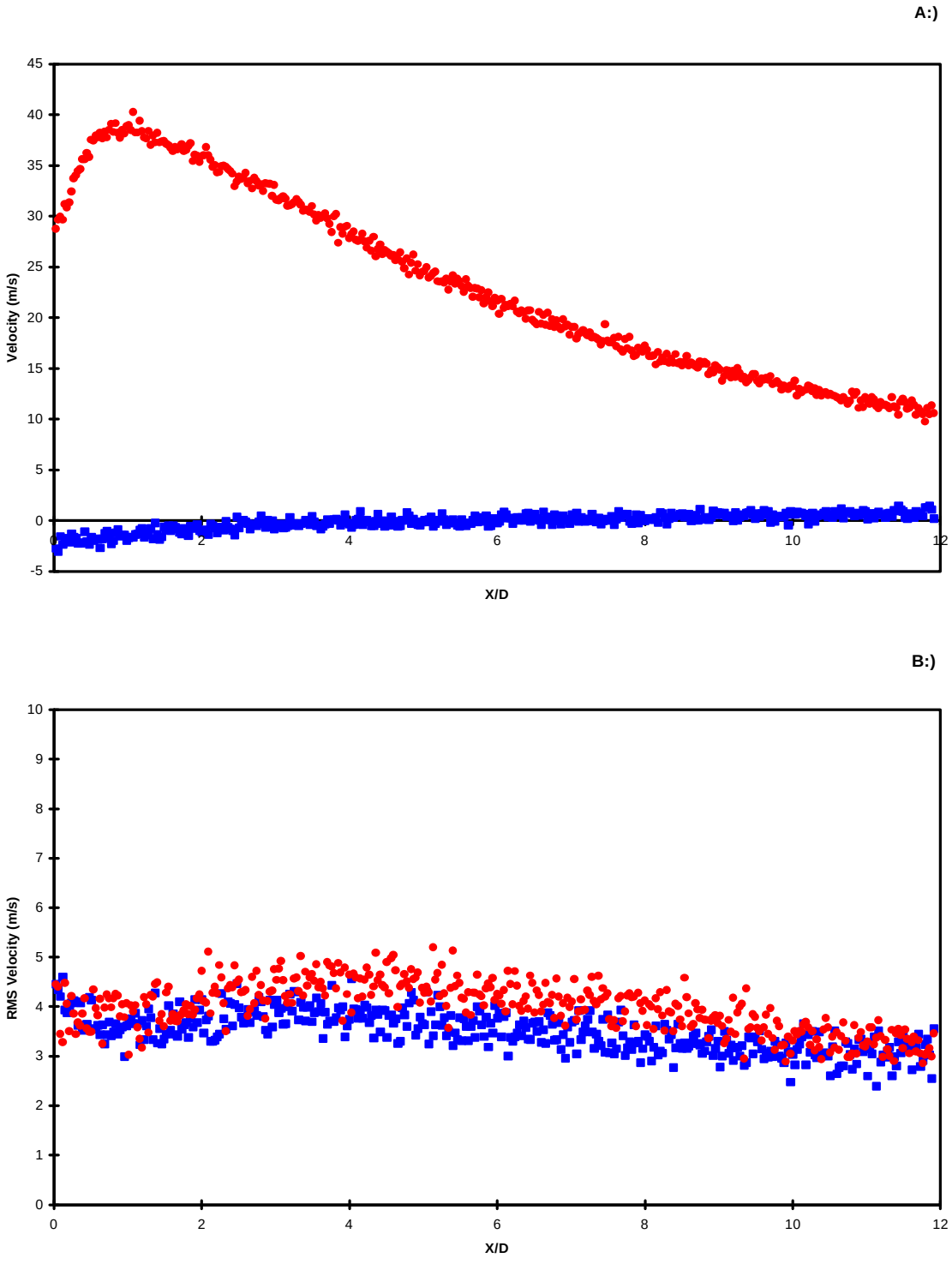

Figure 5.25. Annular jet centerline velocity profiles, run 2
Circles -axial velocity; Squares - circumferential velocity
A.) Mean Velocities
B.) RMS Velocities

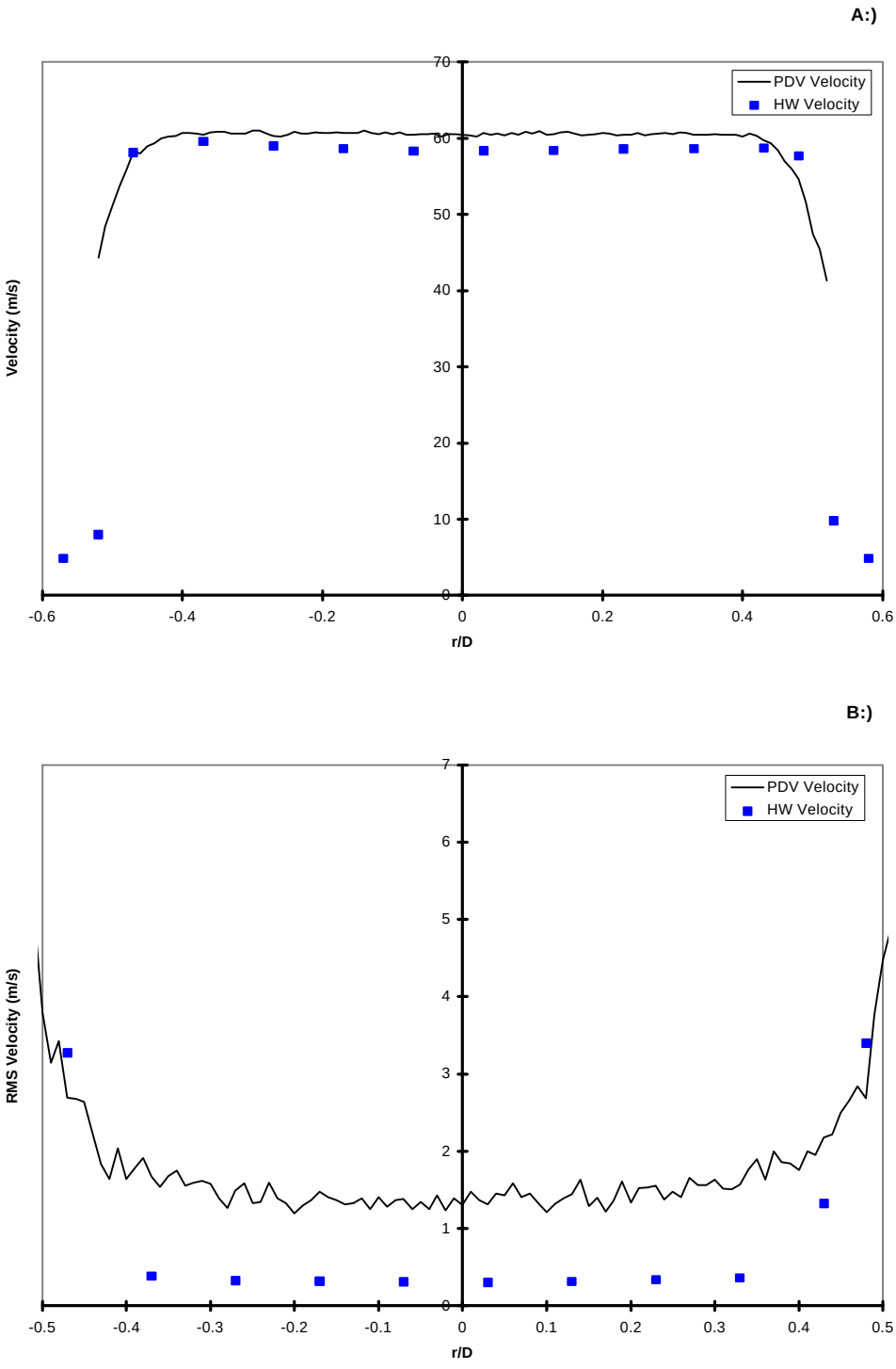

Figure 5.26. Comparisons between hot wire and PDV data for standard jet at jet exit.
A.) axial mean velocity
B.) axial RMS velocity

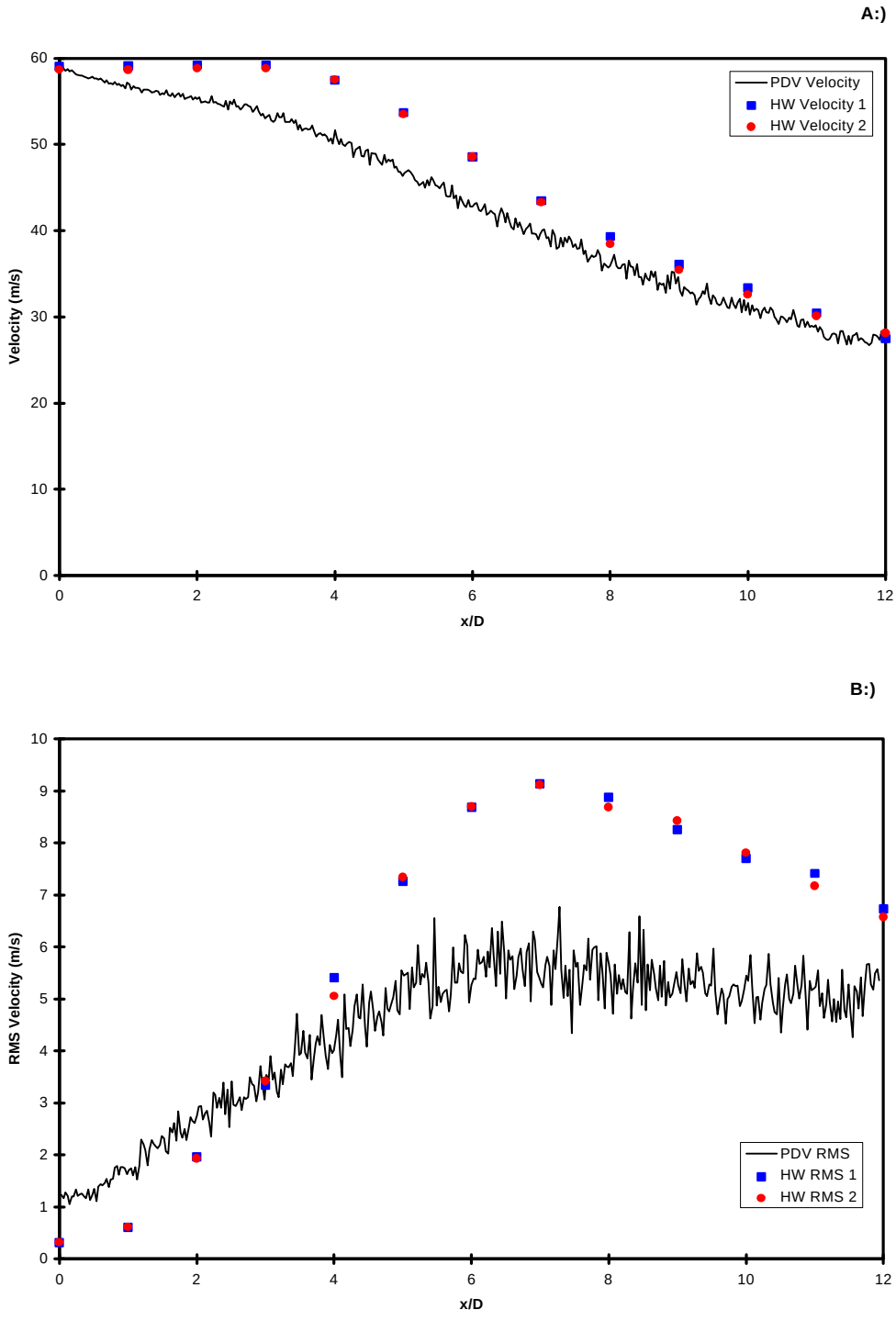

Figure 5.27. Comparisons between hot wire and PDV data for standard jet centerline profile
A.) axial mean velocity
B.) axial RMS velocity

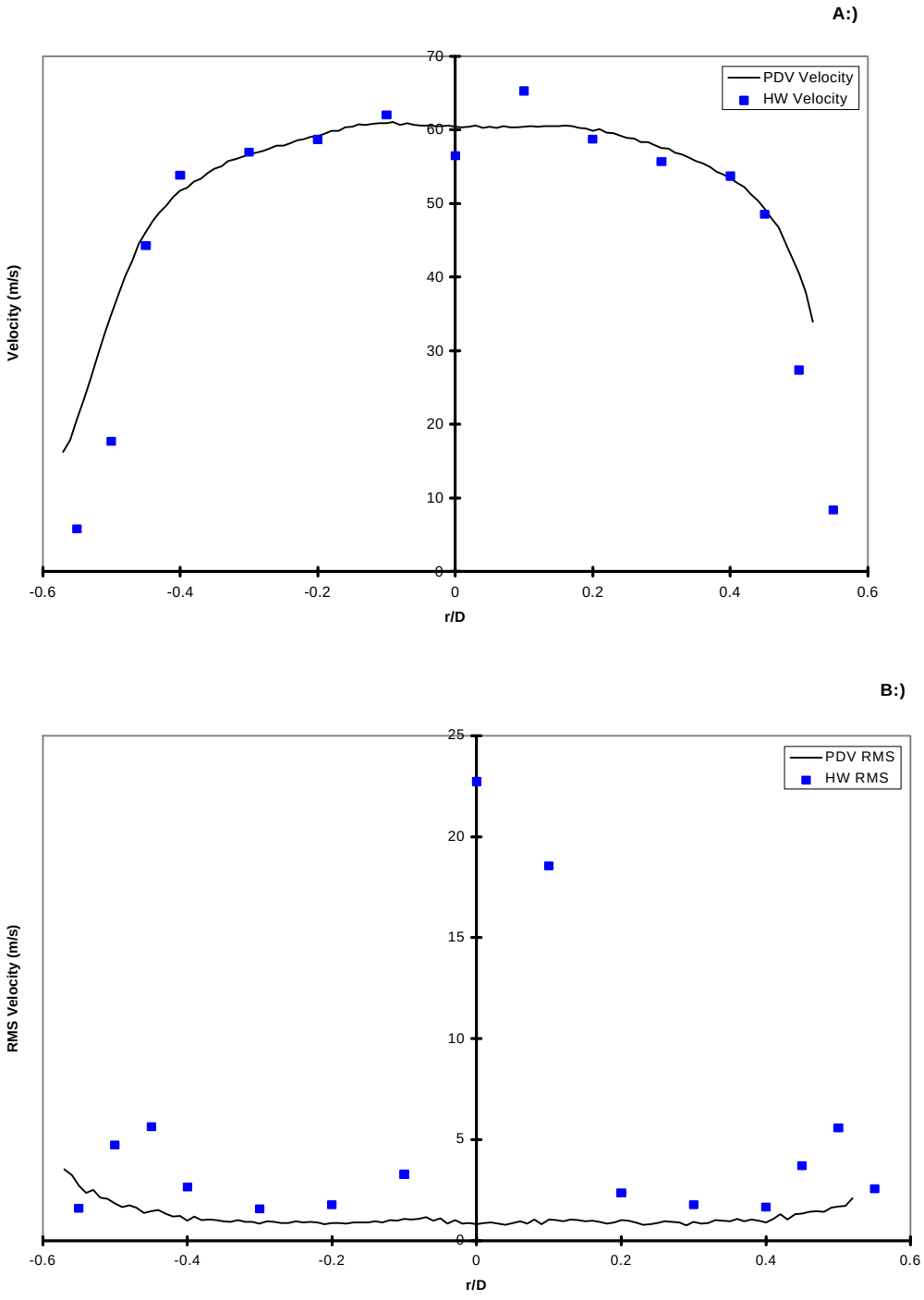

Figure 5.28. Comparisons between hot wire and PDV data for swirling jet at jet exit.
A.) axial mean velocity
B.) axial RMS velocity

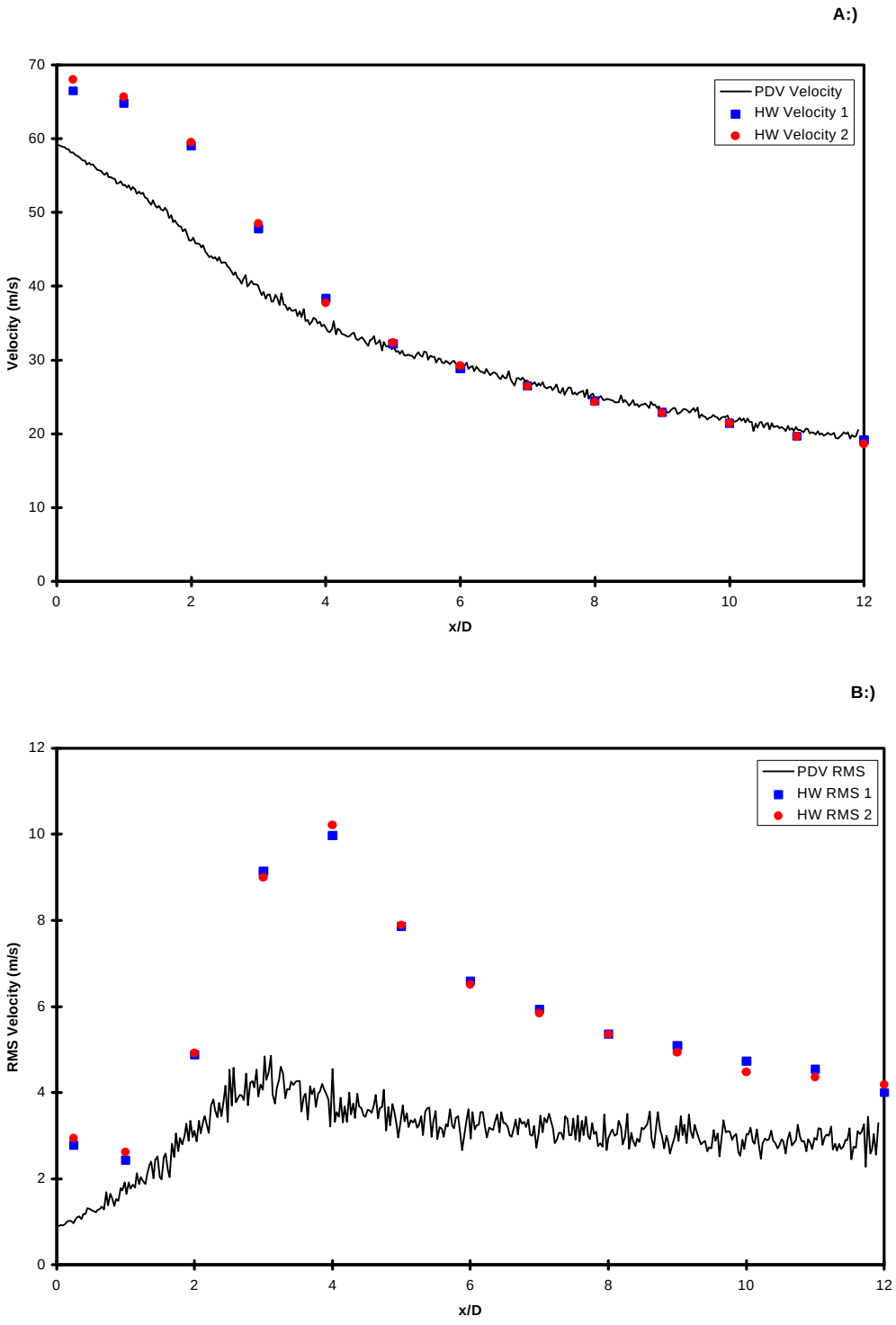

Figure 5.29. Comparisons between hot wire and PDV data for swirling jet centerline profile
A.) axial mean velocity
B.) axial RMS velocity

Appendix A

Radial Profiles of PDV mean and RMS Velocity Data

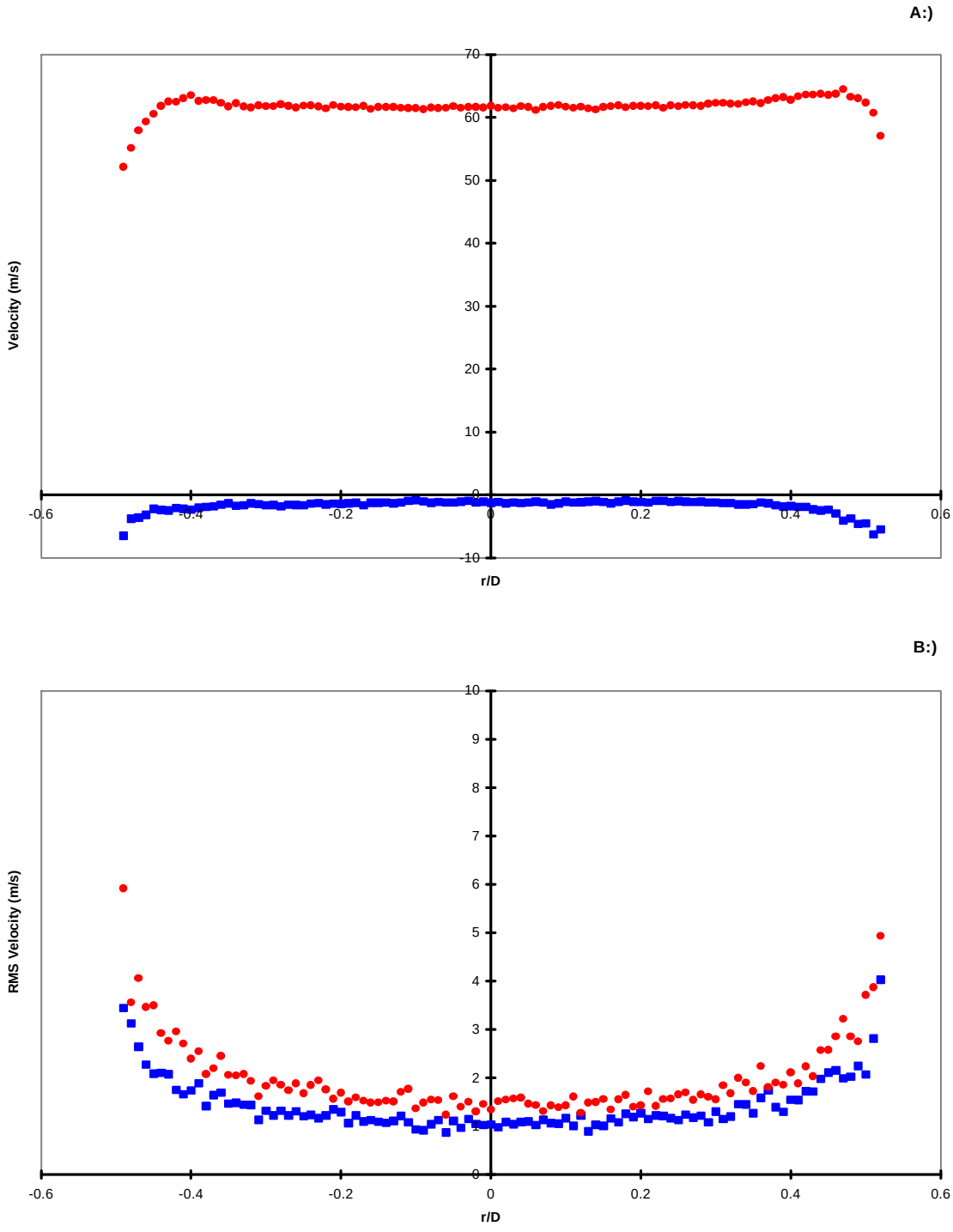

Figure A.1. Radial cut of standard jet at jet exit, run 1
Circles -axial velocity; Squares -circumferential velocity
a.) Mean Velocities
b.) RMS Velocities

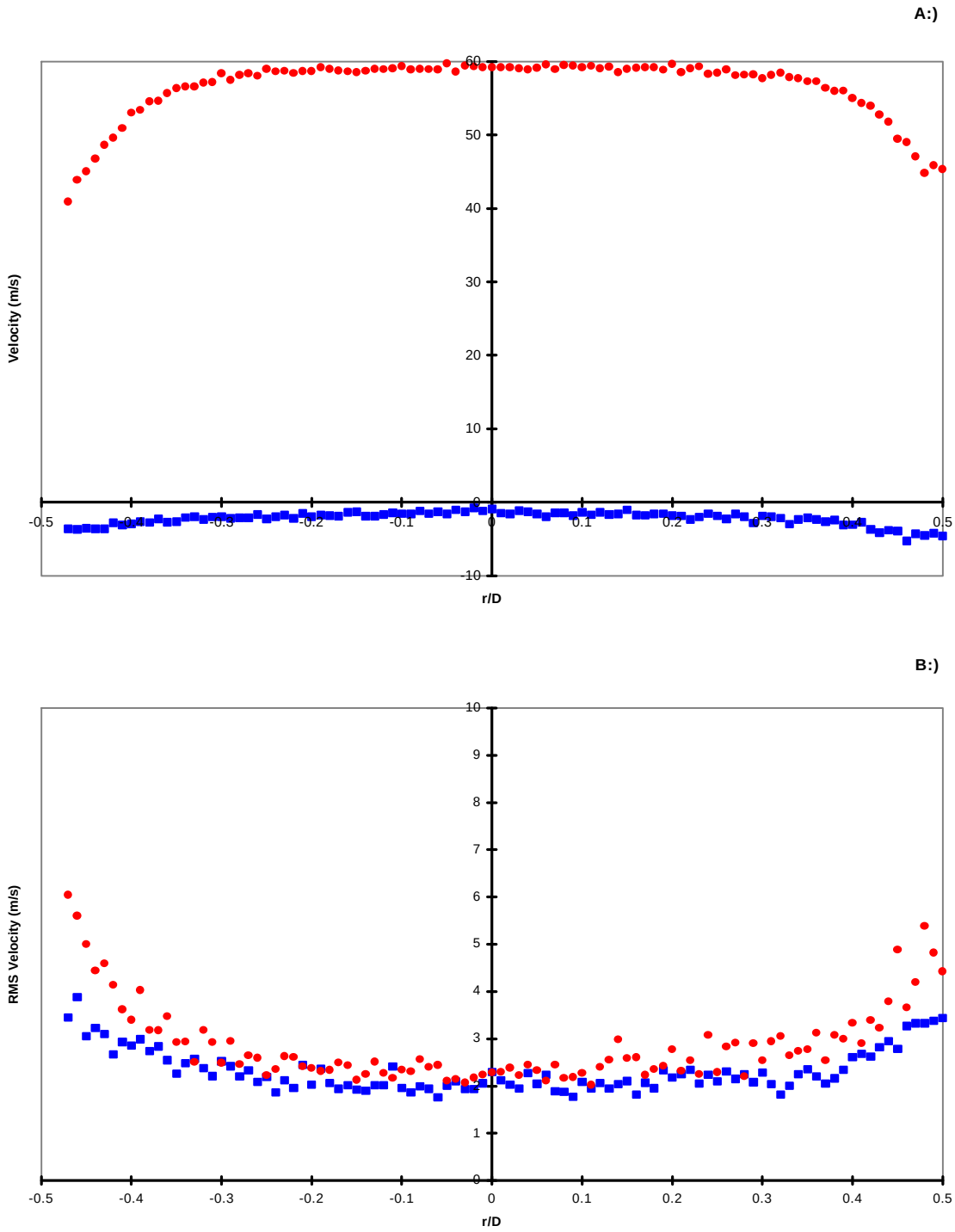

Figure A.2. Radial cut of standard jet at X/D=1, run 1
Circles -axial velocity; Squares -circumferential velocity
a.) Mean Velocities
b.) RMS Velocities

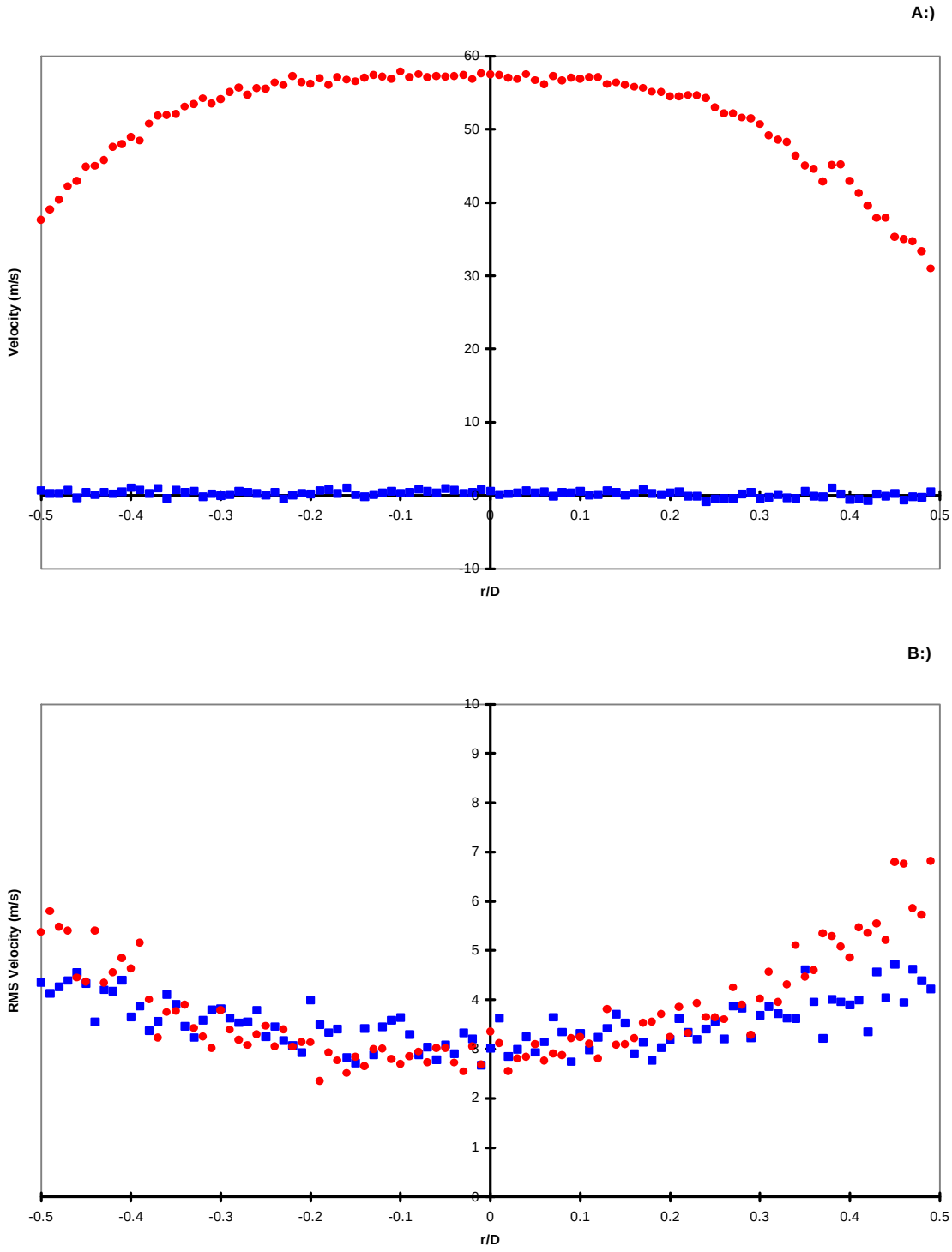

Figure A.3. Radial cut of standard jet at X/D=2, run 1
Circles -axial velocity; Squares -circumferential velocity
a.) Mean Velocities
b.) RMS Velocities

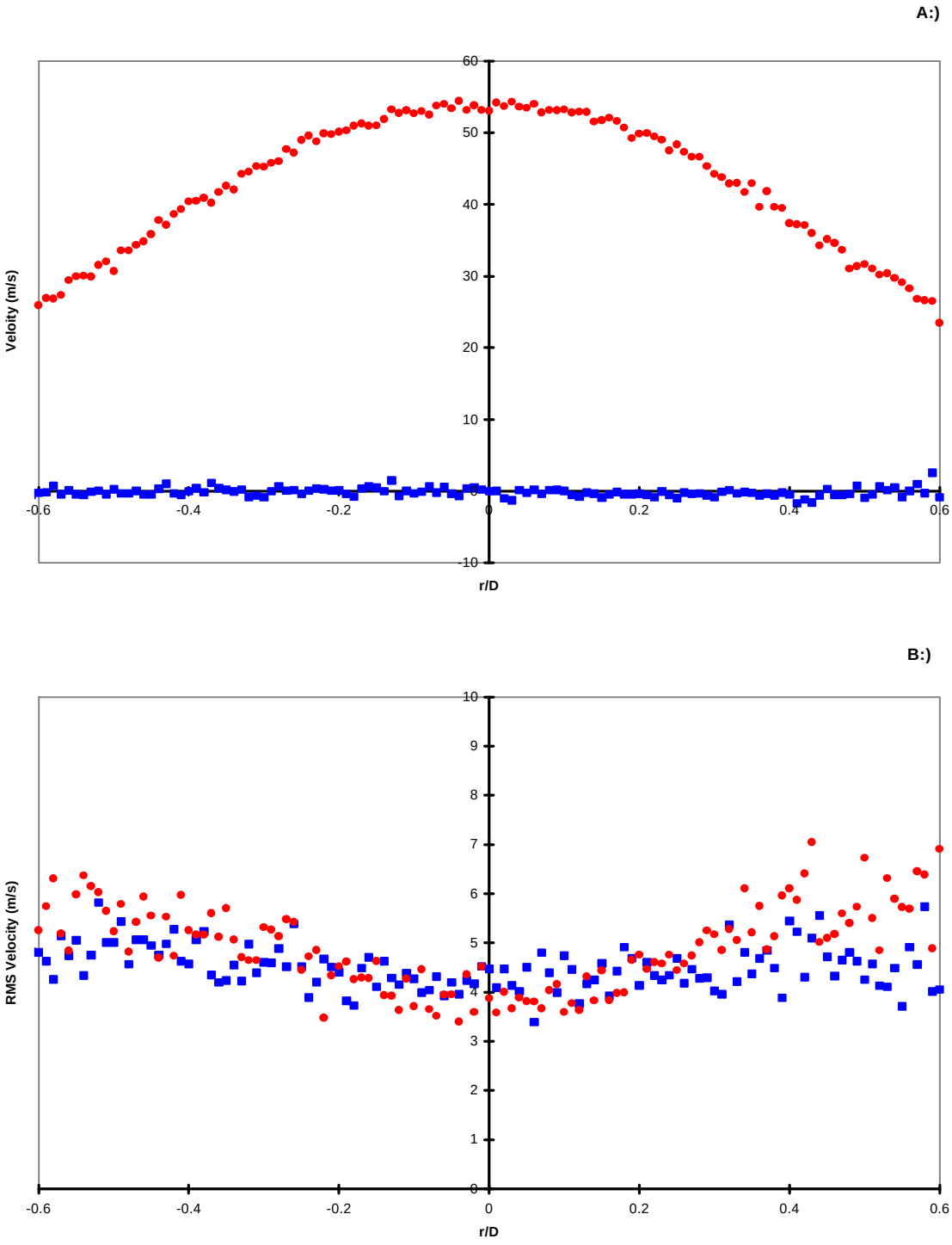

Figure A.4. Radial cut of standard jet at X/D=4, run 1
Circles -axial velocity; Squares -circumferential velocity
a.) Mean Velocities
b.) RMS Velocities

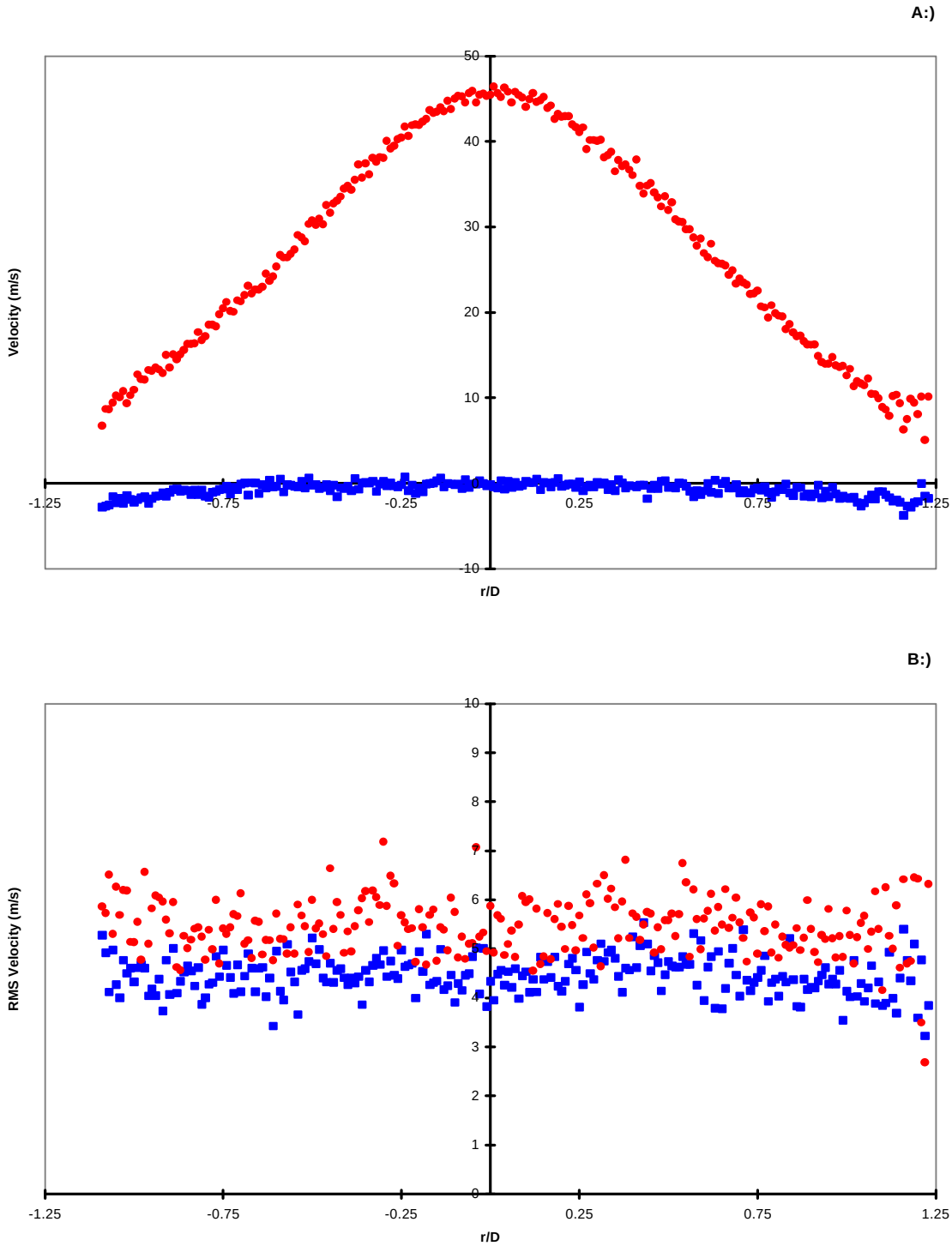

Figure A.5. Radial cut of standard jet at X/D=6, run 1
Circles -axial velocity; Squares -circumferential velocity
a.) Mean Velocities
b.) RMS Velocities

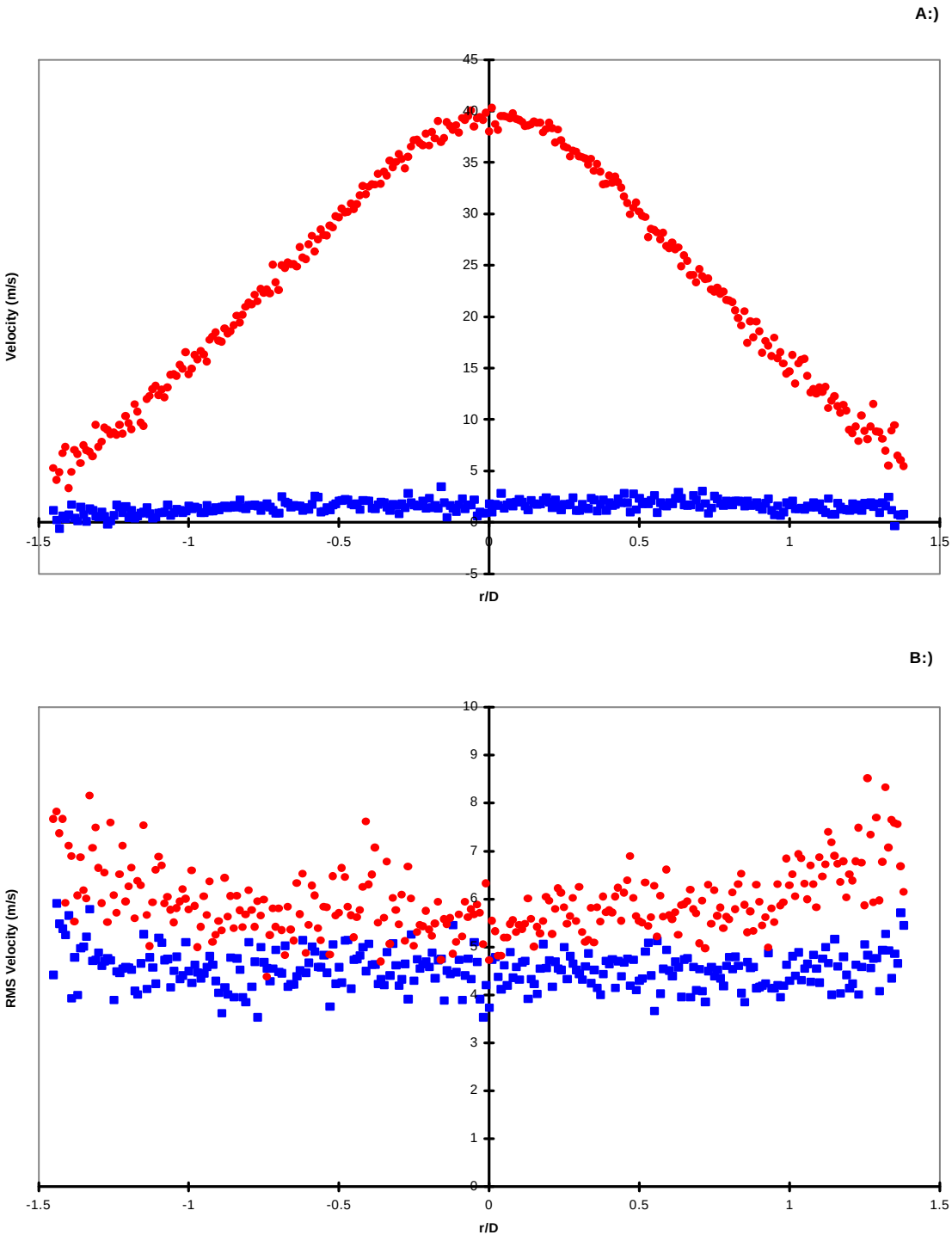

Figure A.6. Radial cut of standard jet at X/D=8, run 1
Circles -axial velocity; Squares -circumferential velocity
a.) Mean Velocities
b.) RMS Velocities

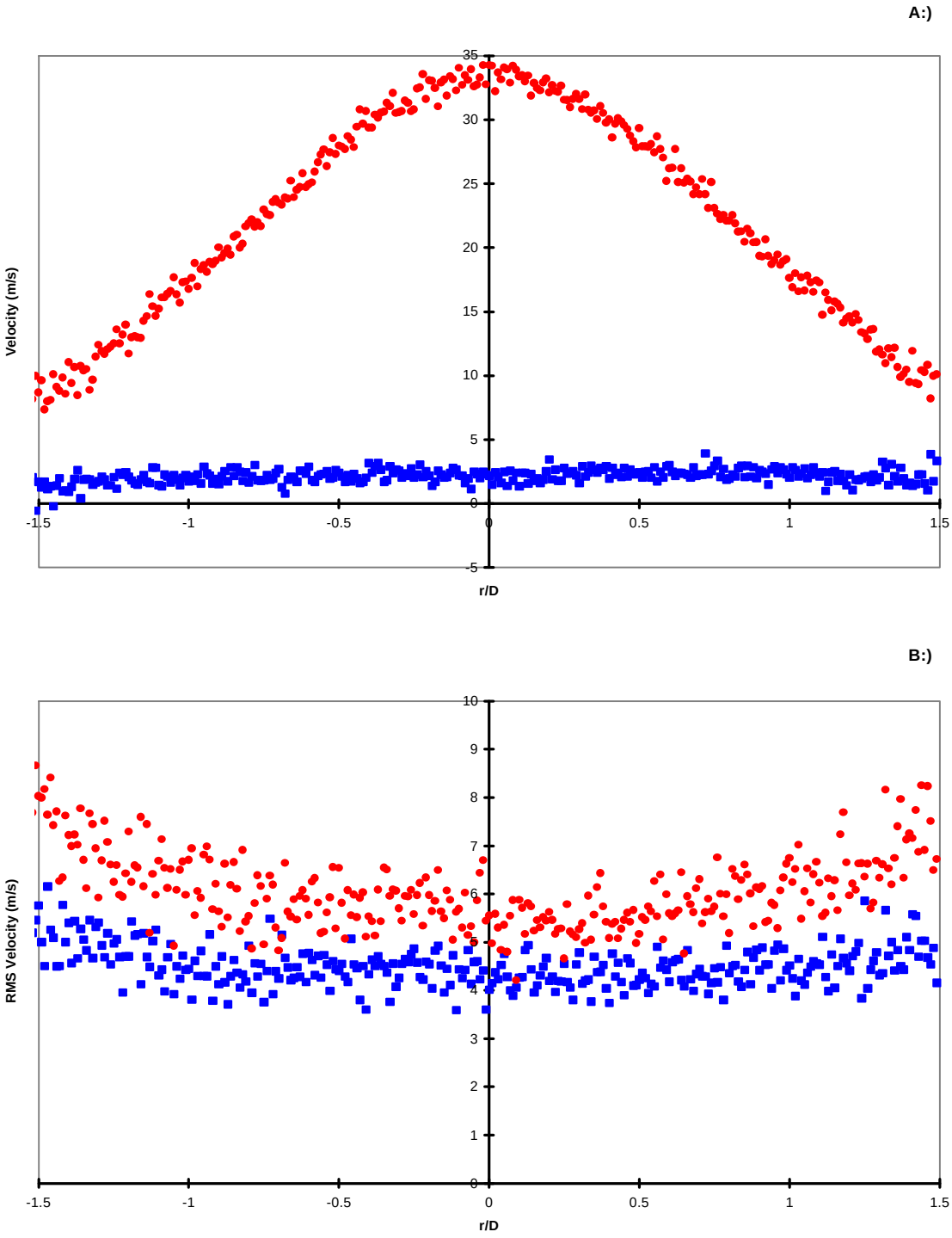

Figure A.7. Radial cut of standard jet at X/D=10, run 1
Circles -axial velocity; Squares -circumferential velocity
a.) Mean Velocities
b.) RMS Velocities

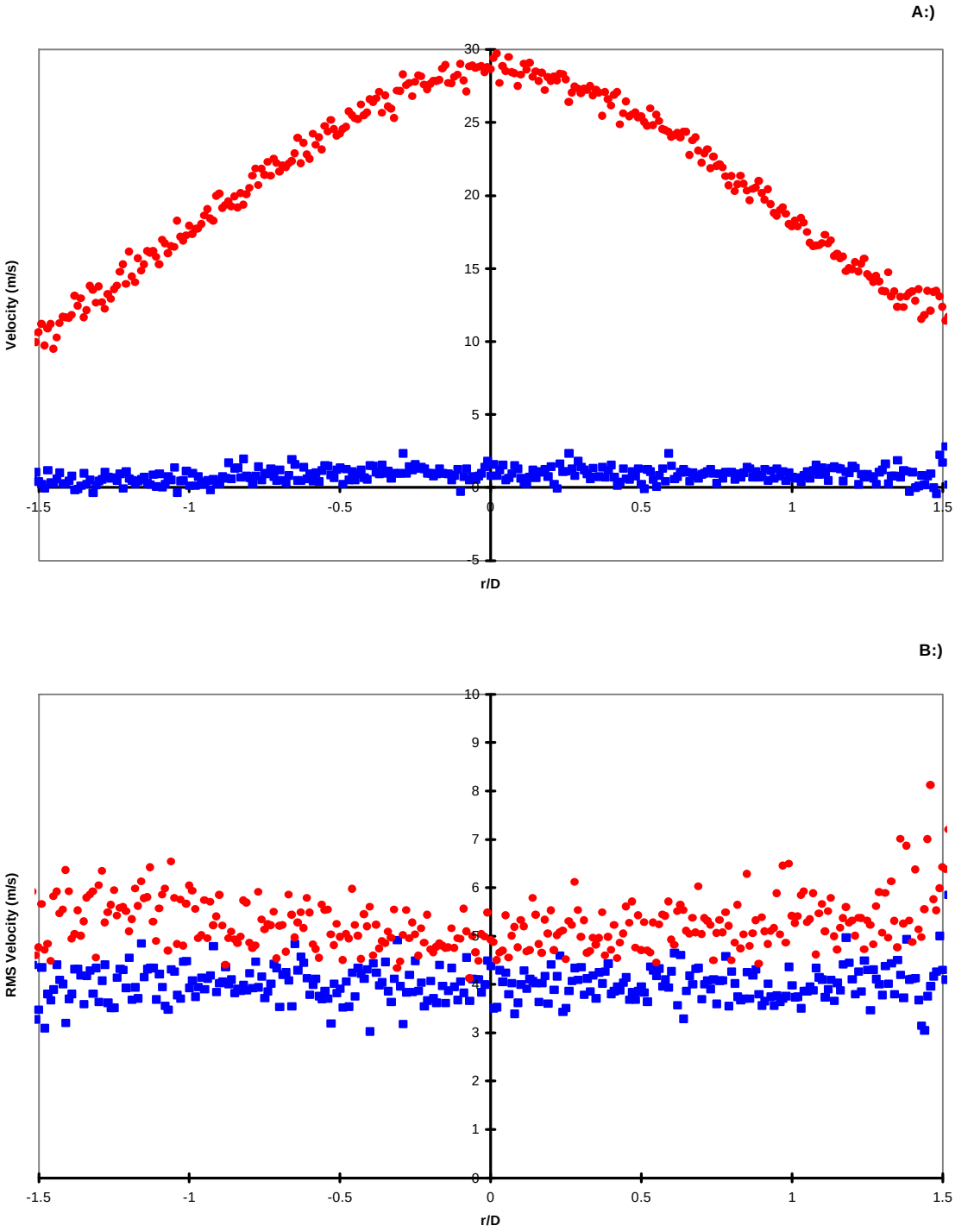

Figure A.8. Radial cut of standard jet at X/D=12, run 1
Circles -axial velocity; Squares -circumferential velocity
a.) Mean Velocities
b.) RMS Velocities

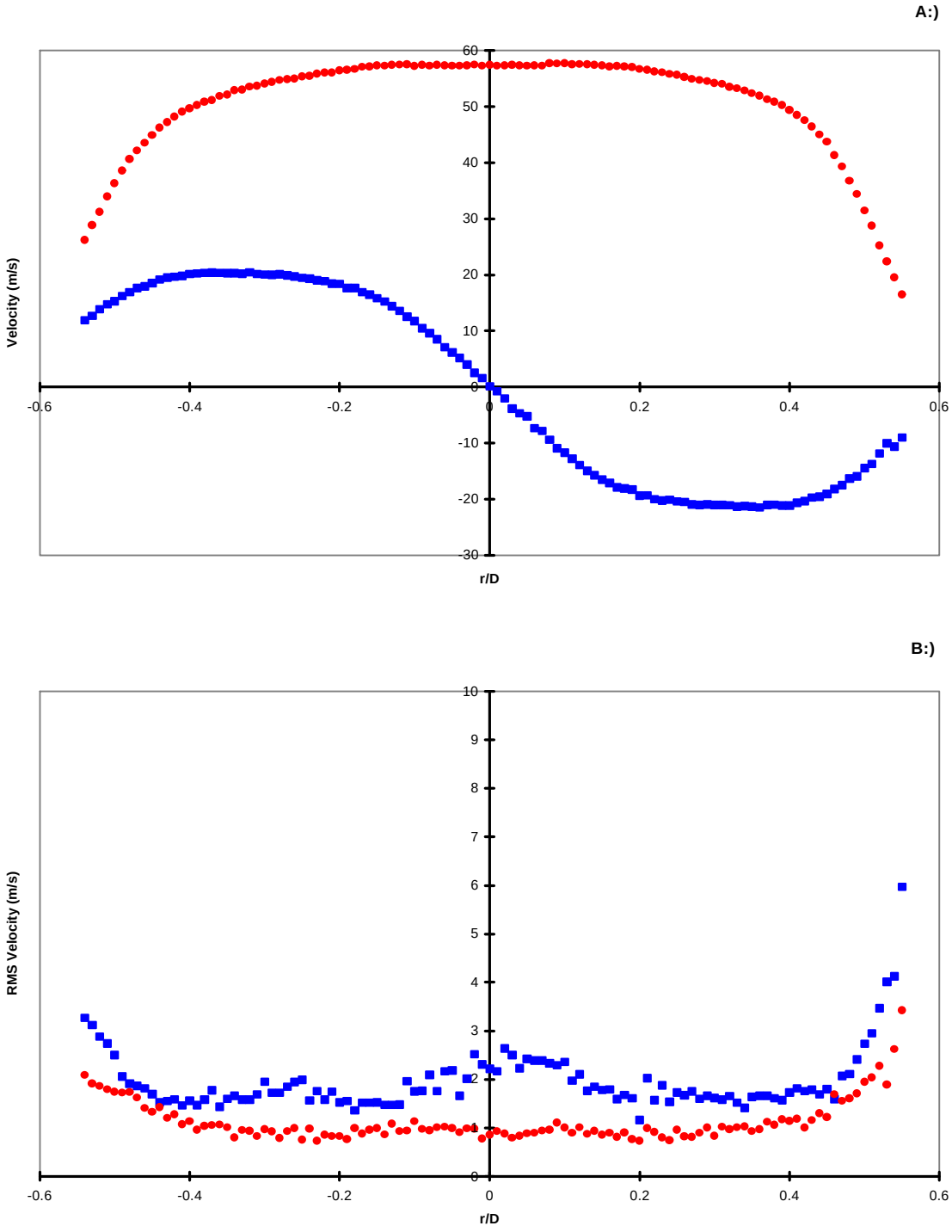

Figure A.9. Radial cut of swirling jet at jet exit, run 1
Circles -axial velocity; Squares -circumferential velocity
a.) Mean Velocities
b.) RMS Velocities

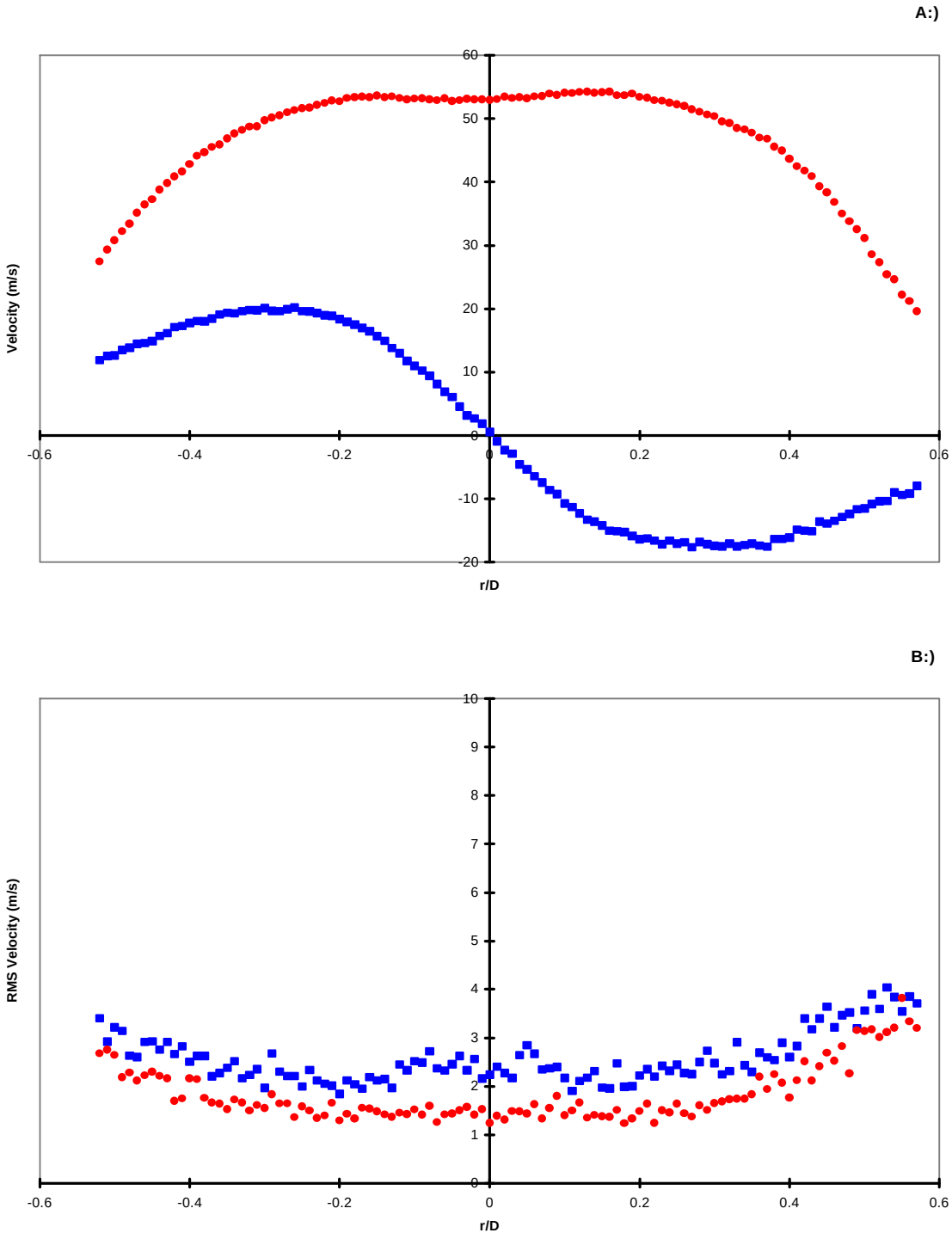

Figure A.10. Radial cut of swirling jet at X/D=1, run 1
Circles -axial velocity; Squares -circumferential velocity
a.) Mean Velocities
b.) RMS Velocities

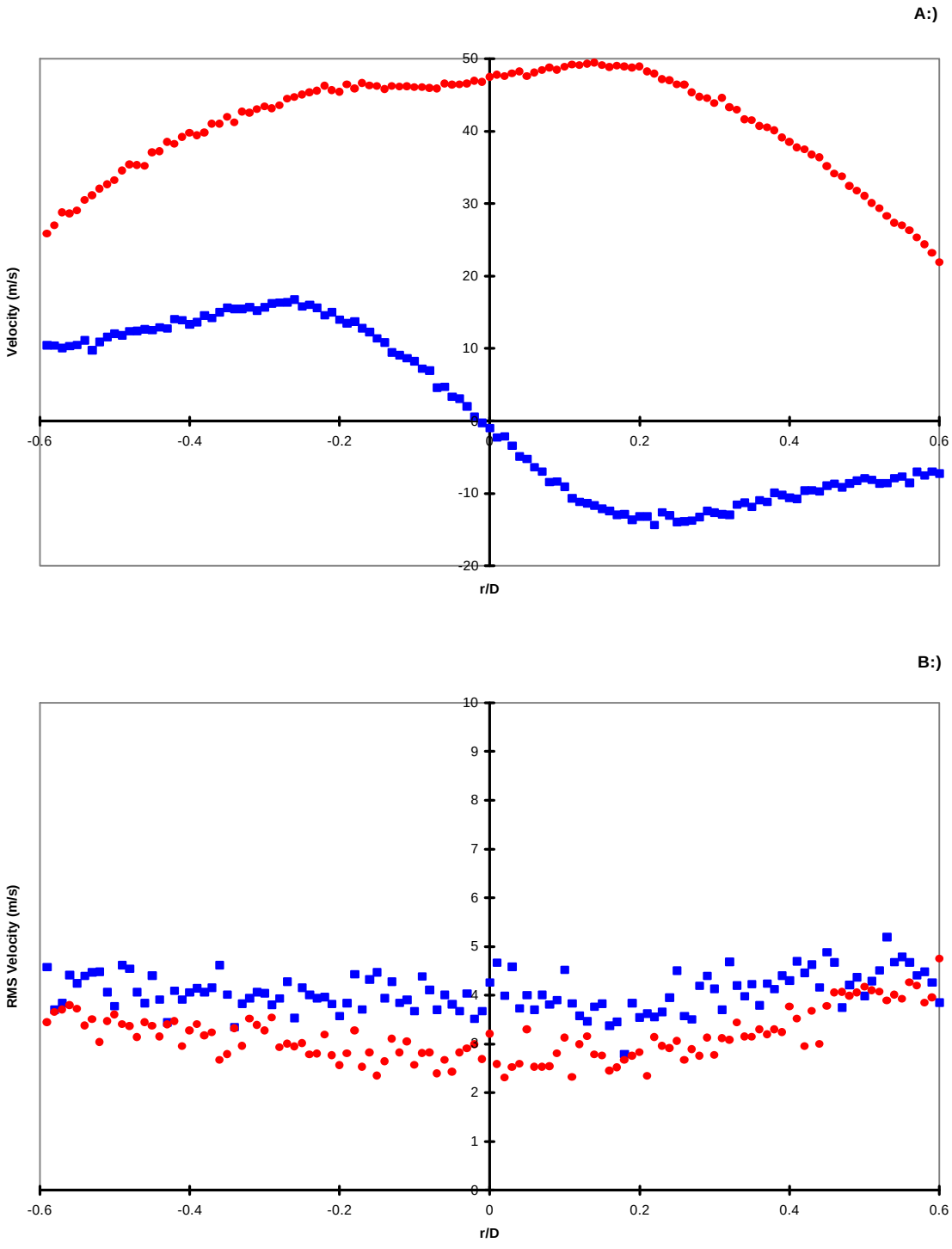

Figure A.11. Radial cut of swirling jet at X/D=2, run 1
Circles -axial velocity; Squares -circumferential velocity
a.) Mean Velocities
b.) RMS Velocities

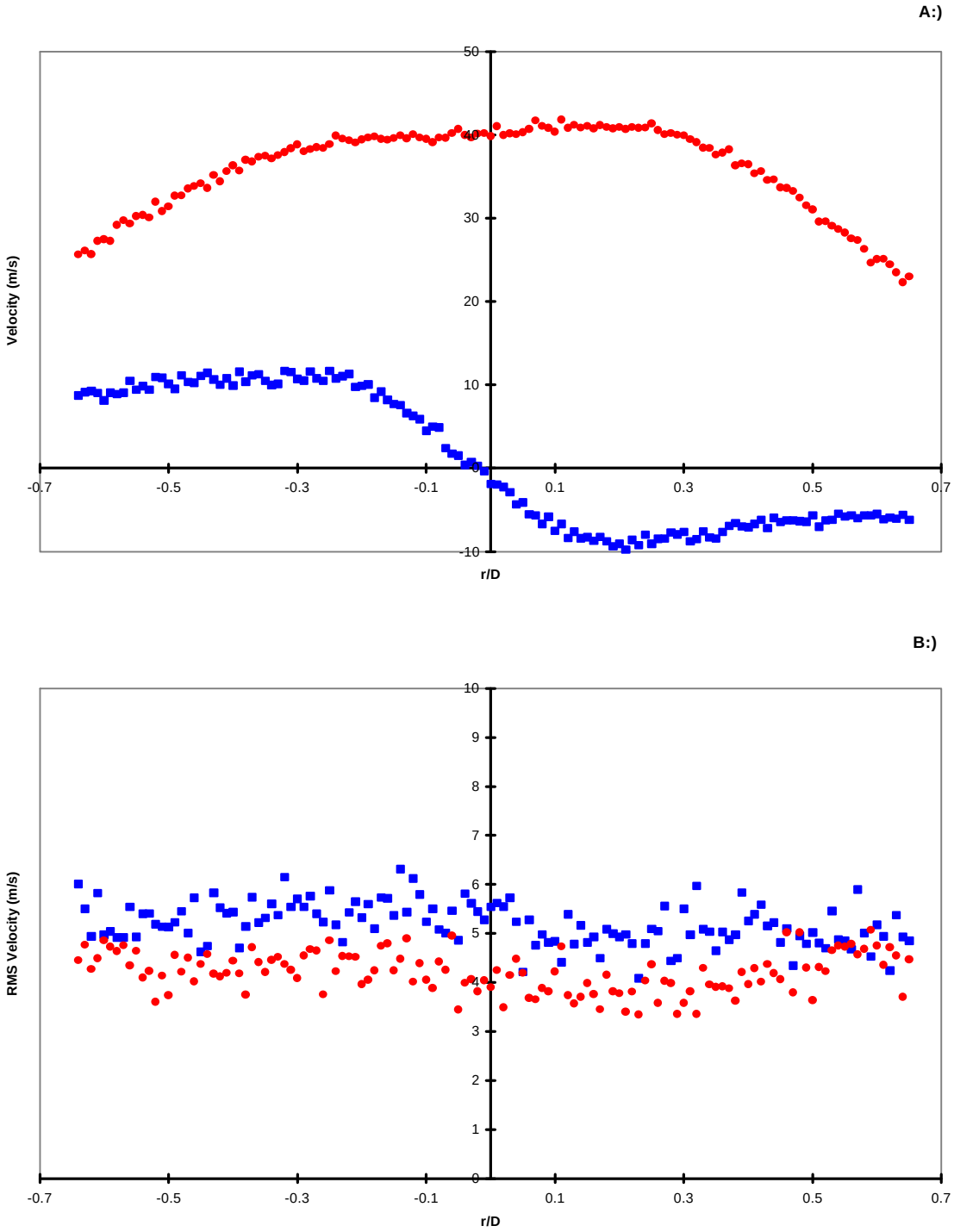

Figure A.12. Radial cut of swirling jet at X/D=3, run 1
Circles -axial velocity; Squares -circumferential velocity
a.) Mean Velocities
b.) RMS Velocities

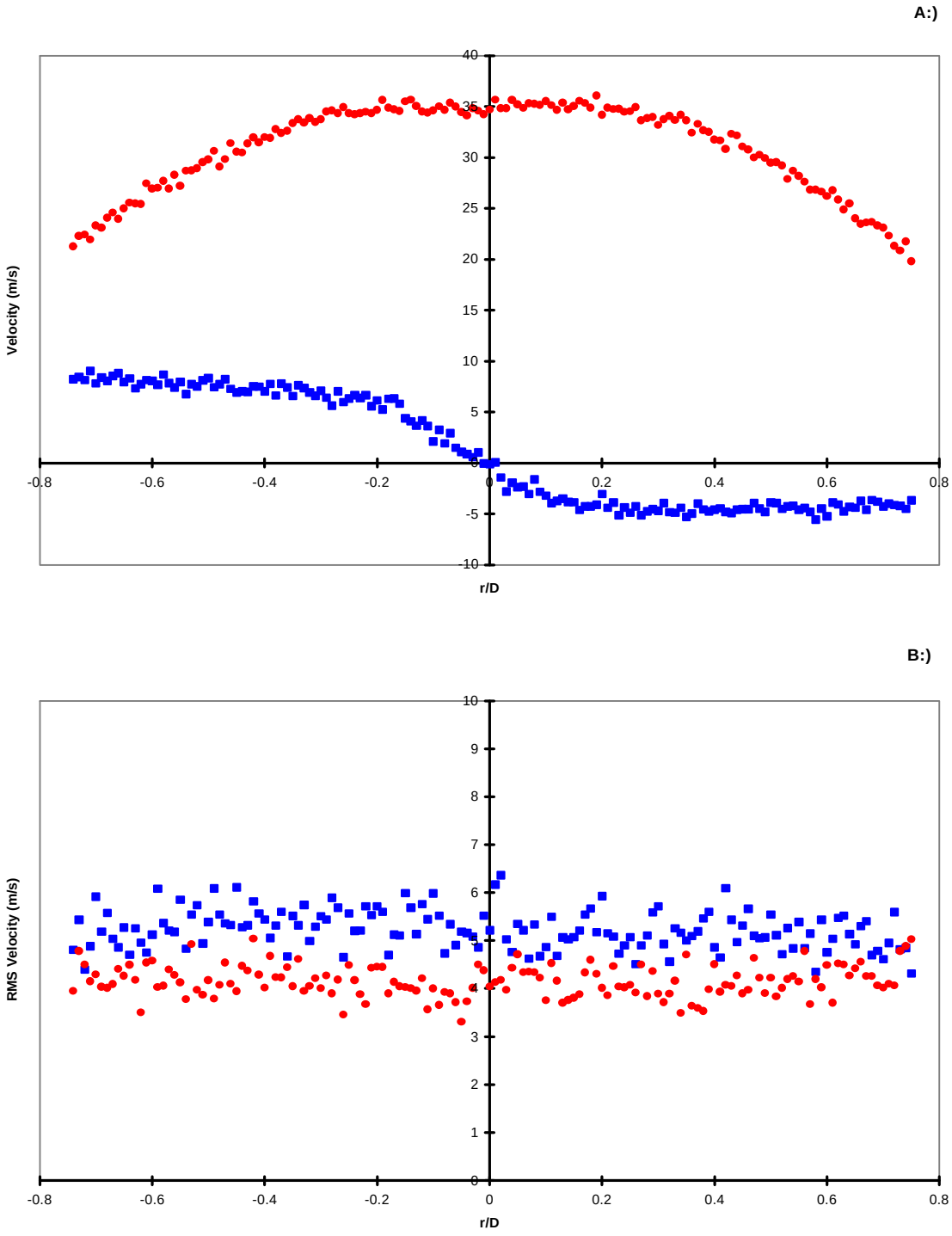

Figure A.13. Radial cut of swirling jet at X/D=4, run 1
Circles -axial velocity; Squares -circumferential velocity
a.) Mean Velocities
b.) RMS Velocities

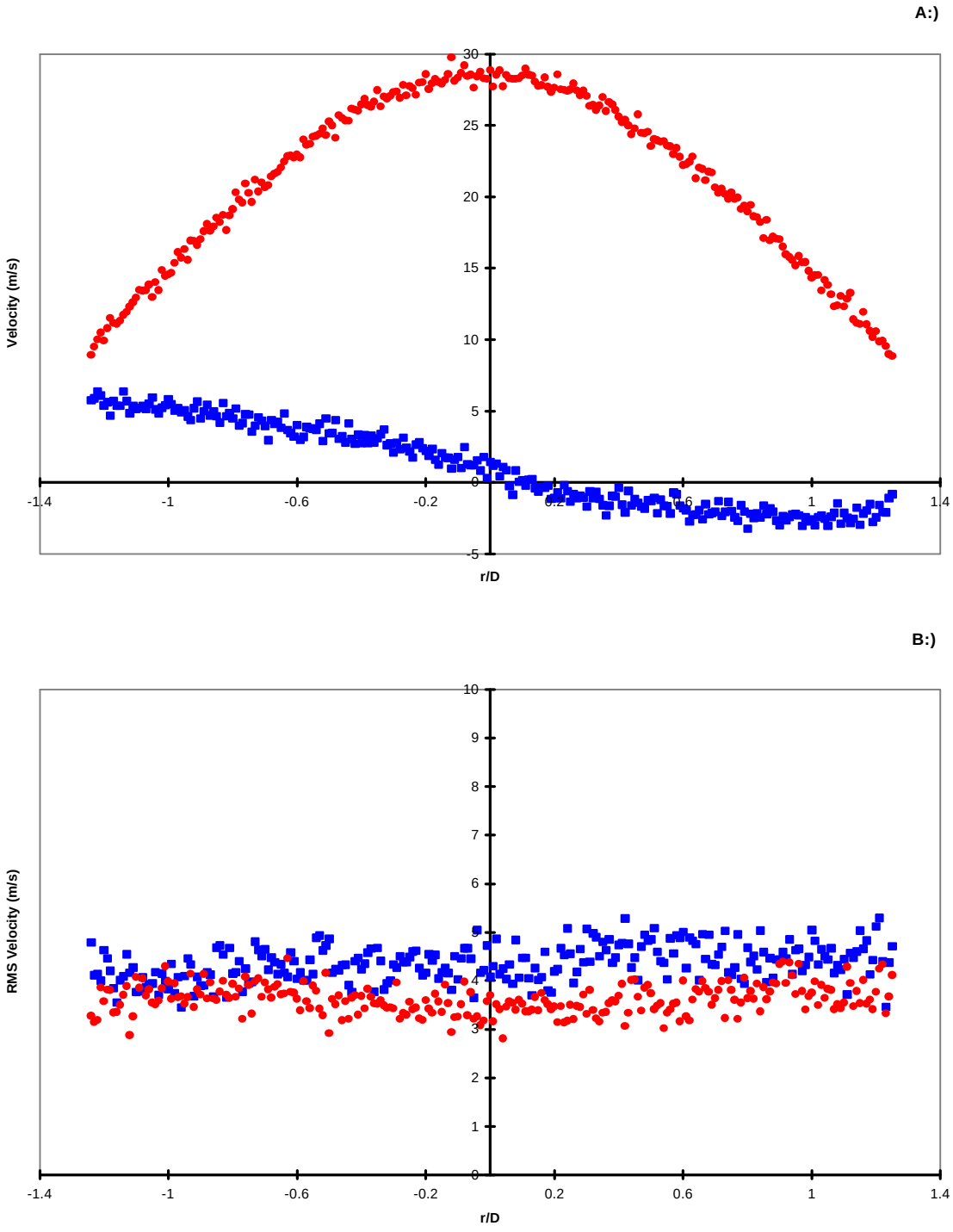

Figure A.14. Radial cut of swirling jet at X/D=6, run 1
Circles -axial velocity; Squares -circumferential velocity
a.) Mean Velocities
b.) RMS Velocities

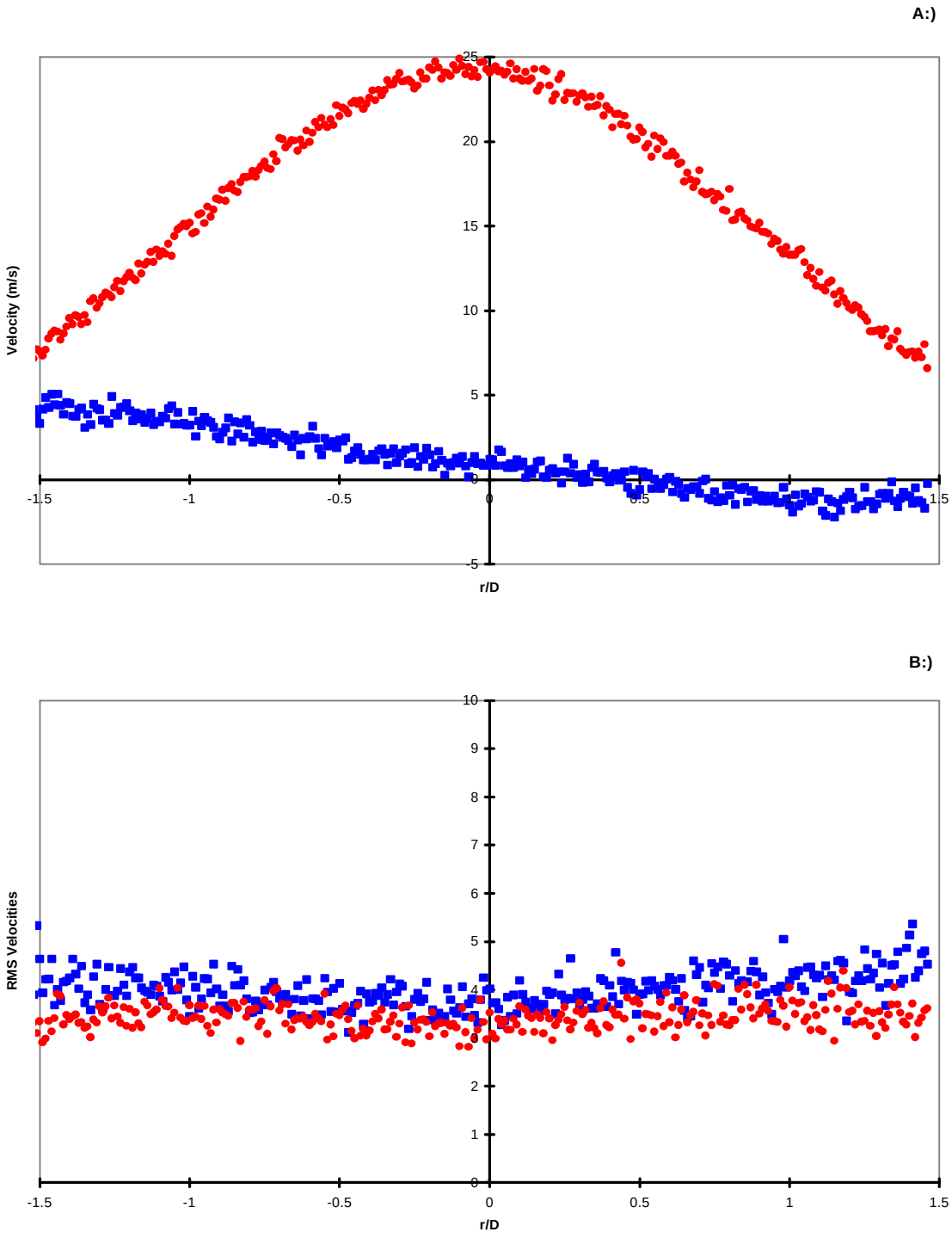

Figure A.15. Radial cut of swirling jet at X/D=8, run 1
Circles -axial velocity; Squares -circumferential velocity
a.) Mean Velocities
b.) RMS Velocities

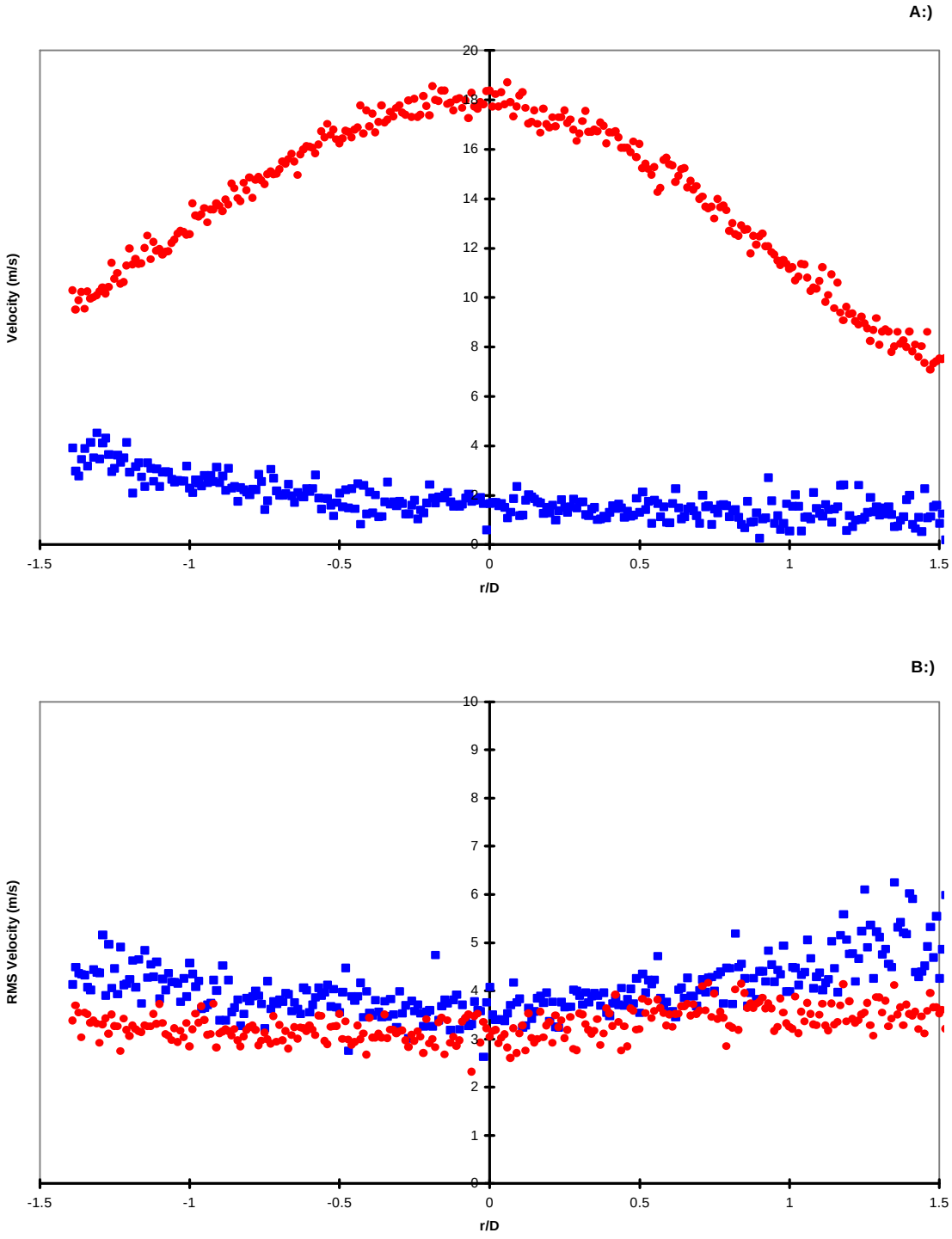

Figure A.16. Radial cut of swirling jet at X/D=12, run 1
Circles -axial velocity; Squares -circumferential velocity
a.) Mean Velocities
b.) RMS Velocities

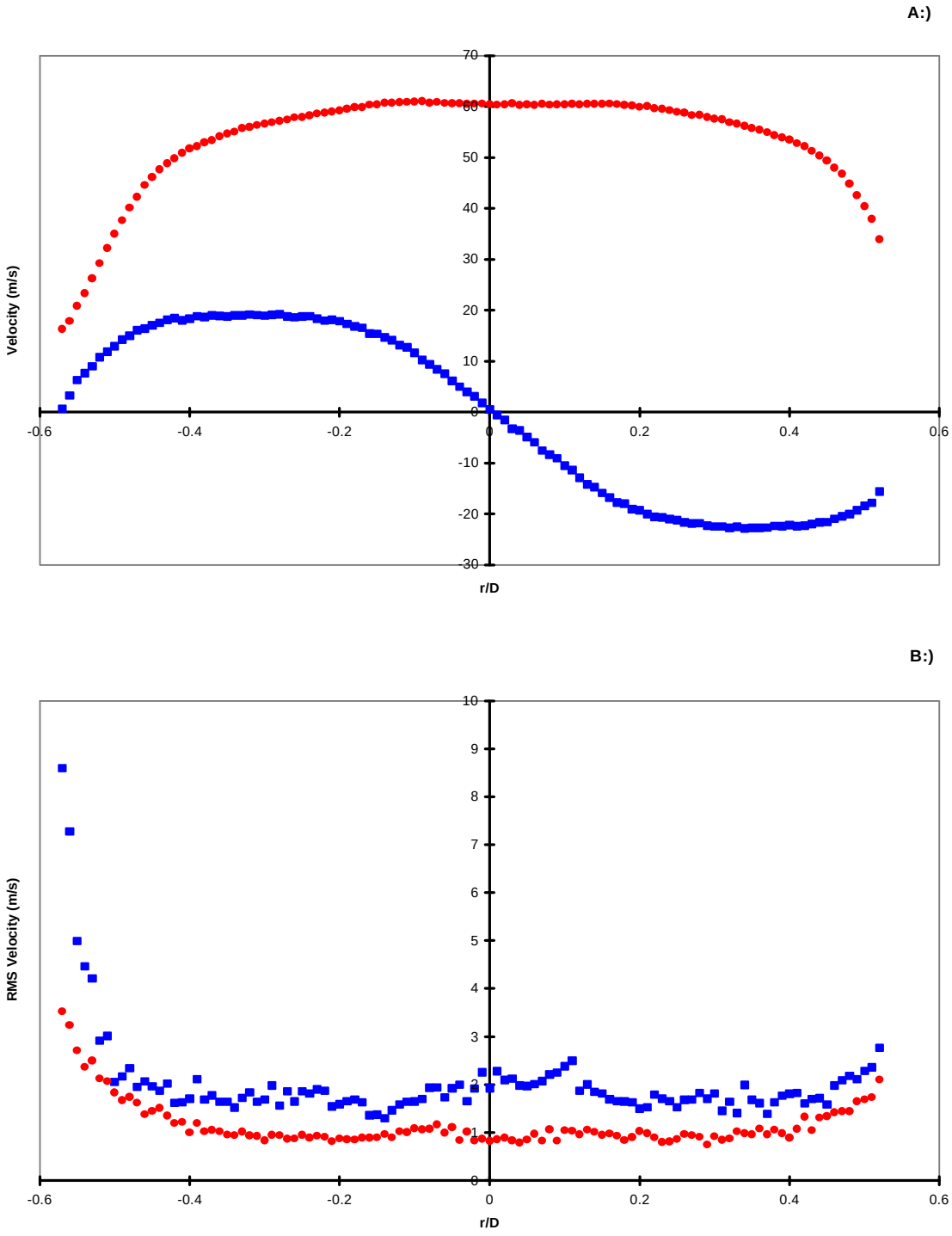

Figure A.17. Radial cut of swirling jet at jet exit, run 2
Circles -axial velocity; Squares -circumferential velocity
a.) Mean Velocities
b.) RMS Velocities

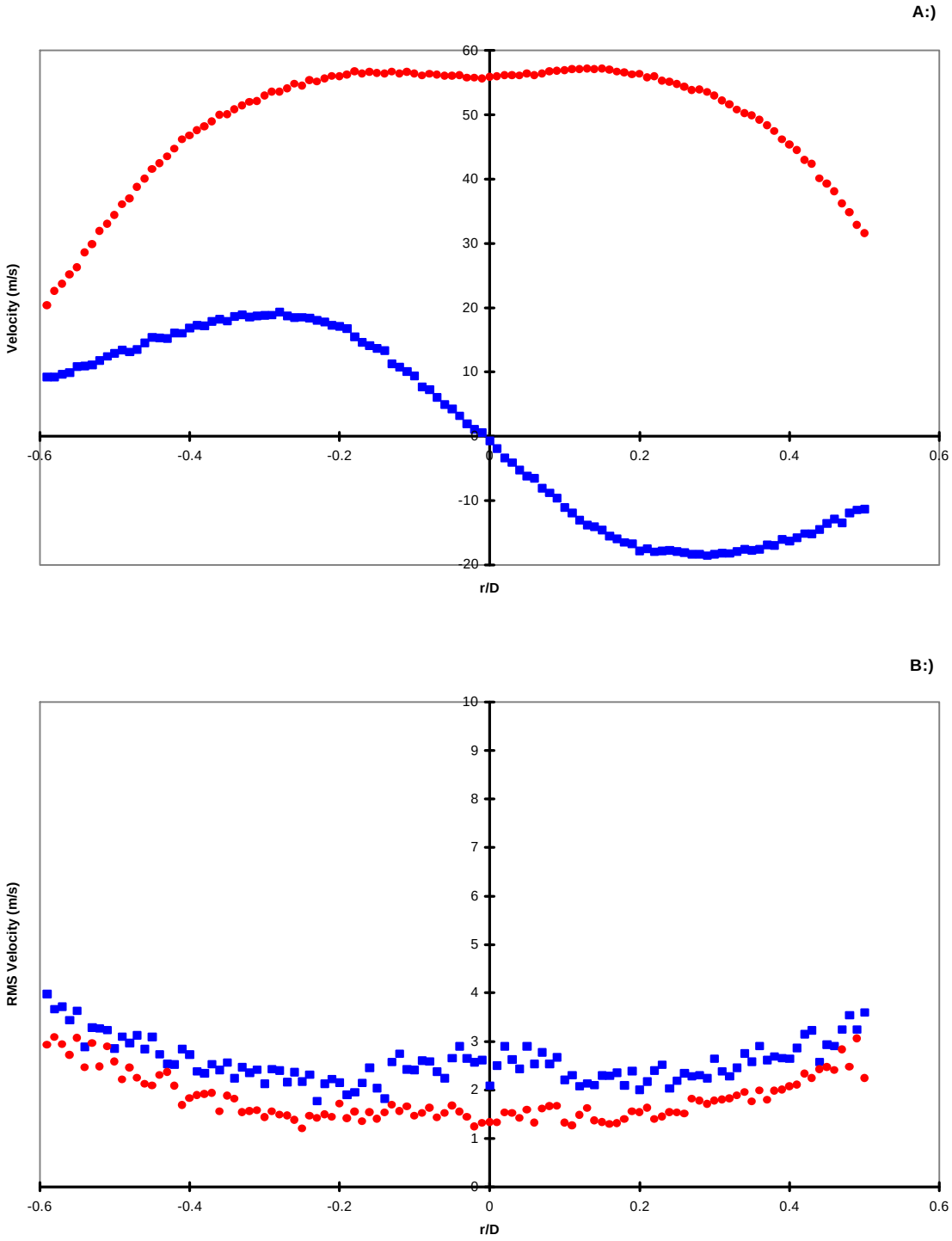

Figure A.18. Radial cut of swirling jet at X/D=1, run 2
Circles -axial velocity; Squares -circumferential velocity
a.) Mean Velocities
b.) RMS Velocities

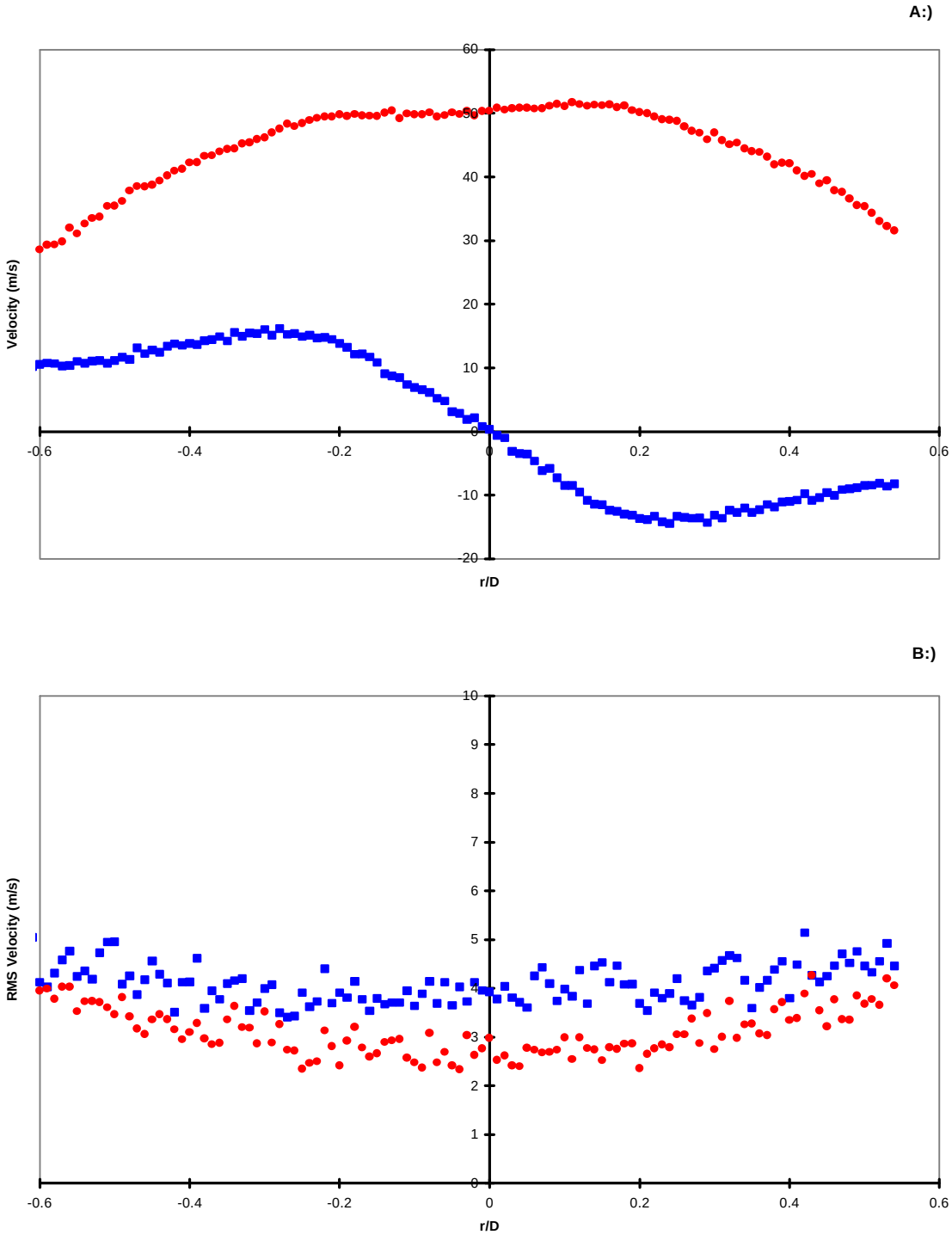

Figure A.19. Radial cut of swirling jet at X/D=2, run 2
Circles -axial velocity; Squares -circumferential velocity
a.) Mean Velocities
b.) RMS Velocities

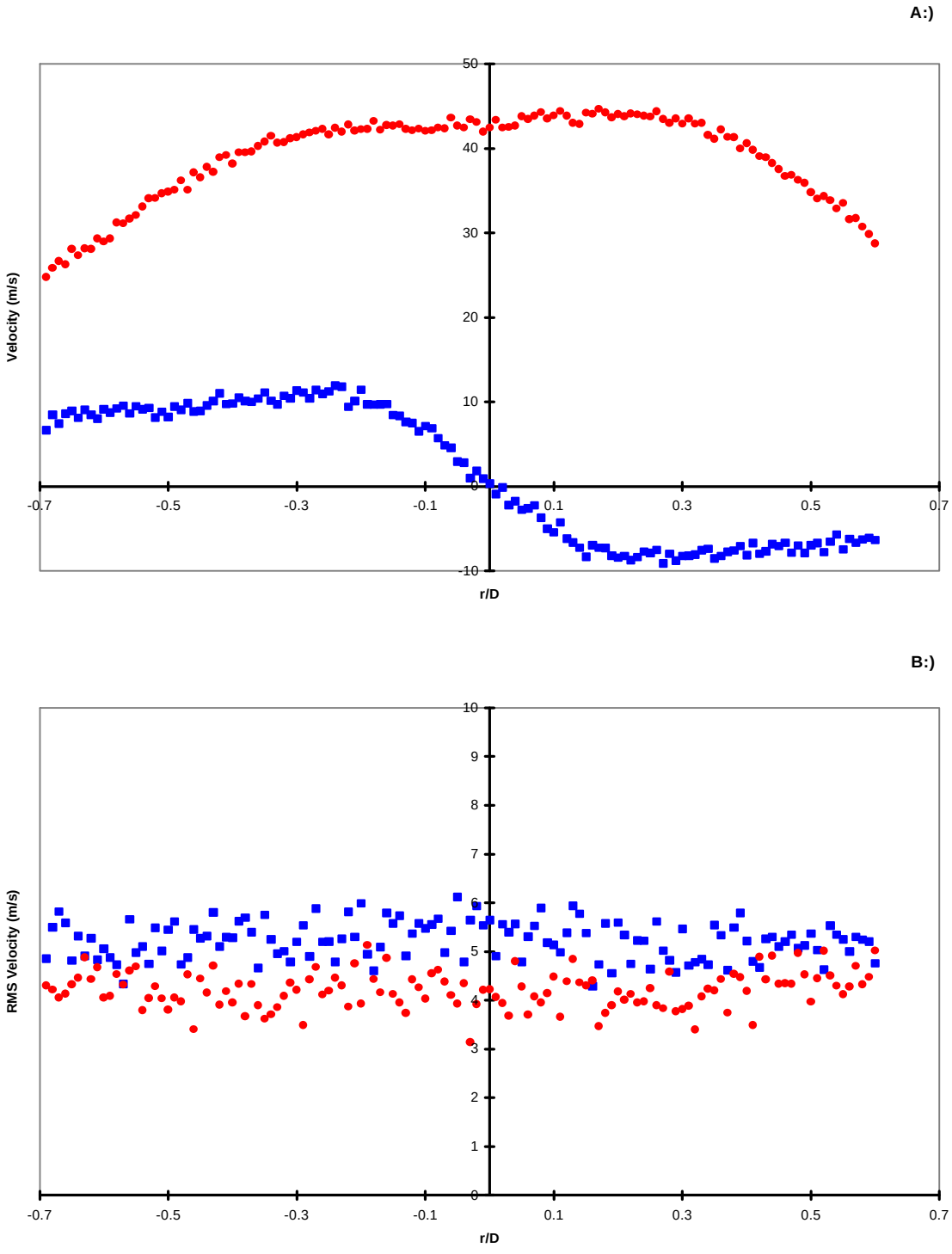

Figure A.20. Radial cut of swirling jet at X/D=3, run 2
Circles -axial velocity; Squares -circumferential velocity
a.) Mean Velocities
b.) RMS Velocities

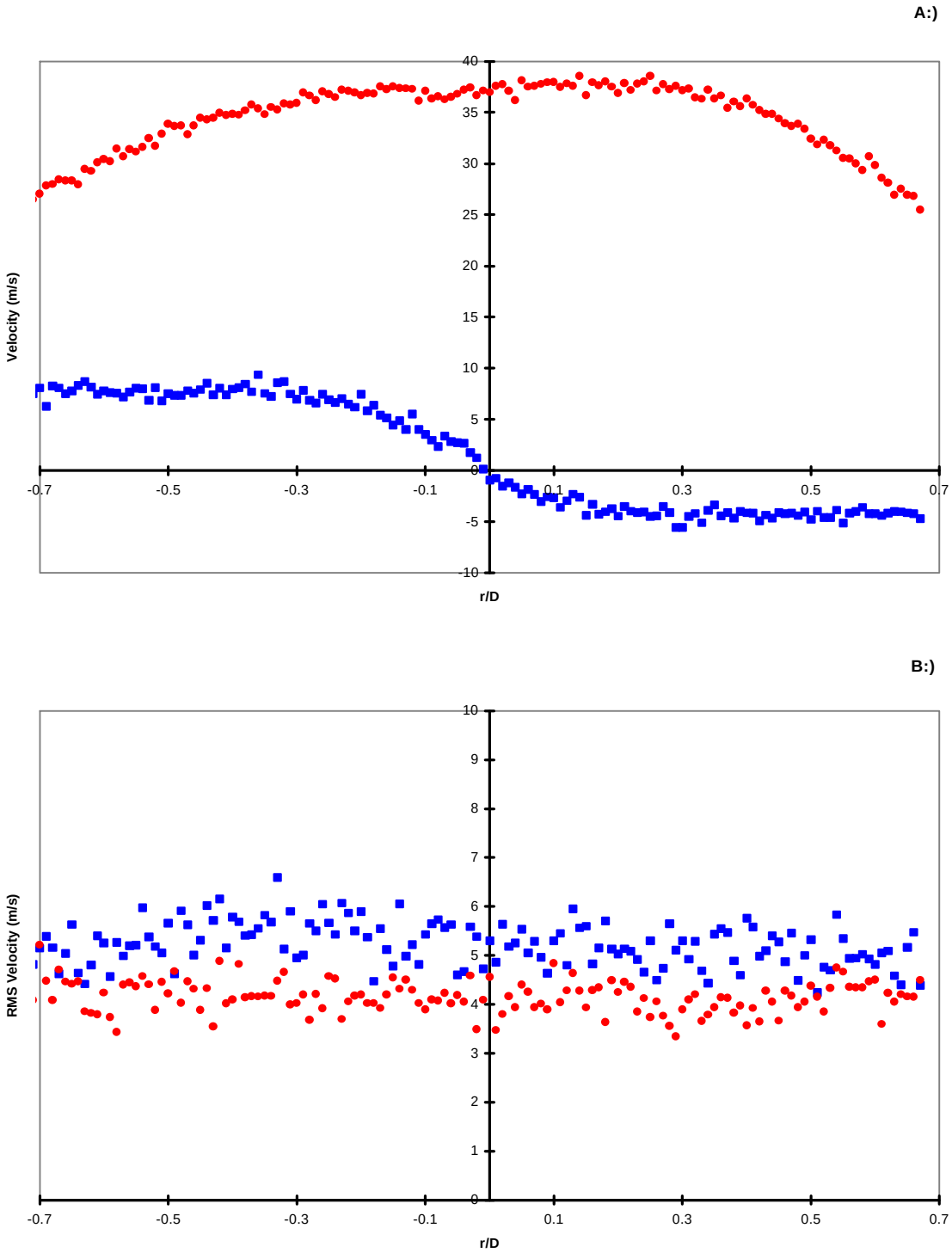

Figure A.21. Radial cut of swirling jet at X/D=4, run 2
Circles -axial velocity; Squares -circumferential velocity
a.) Mean Velocities
b.) RMS Velocities

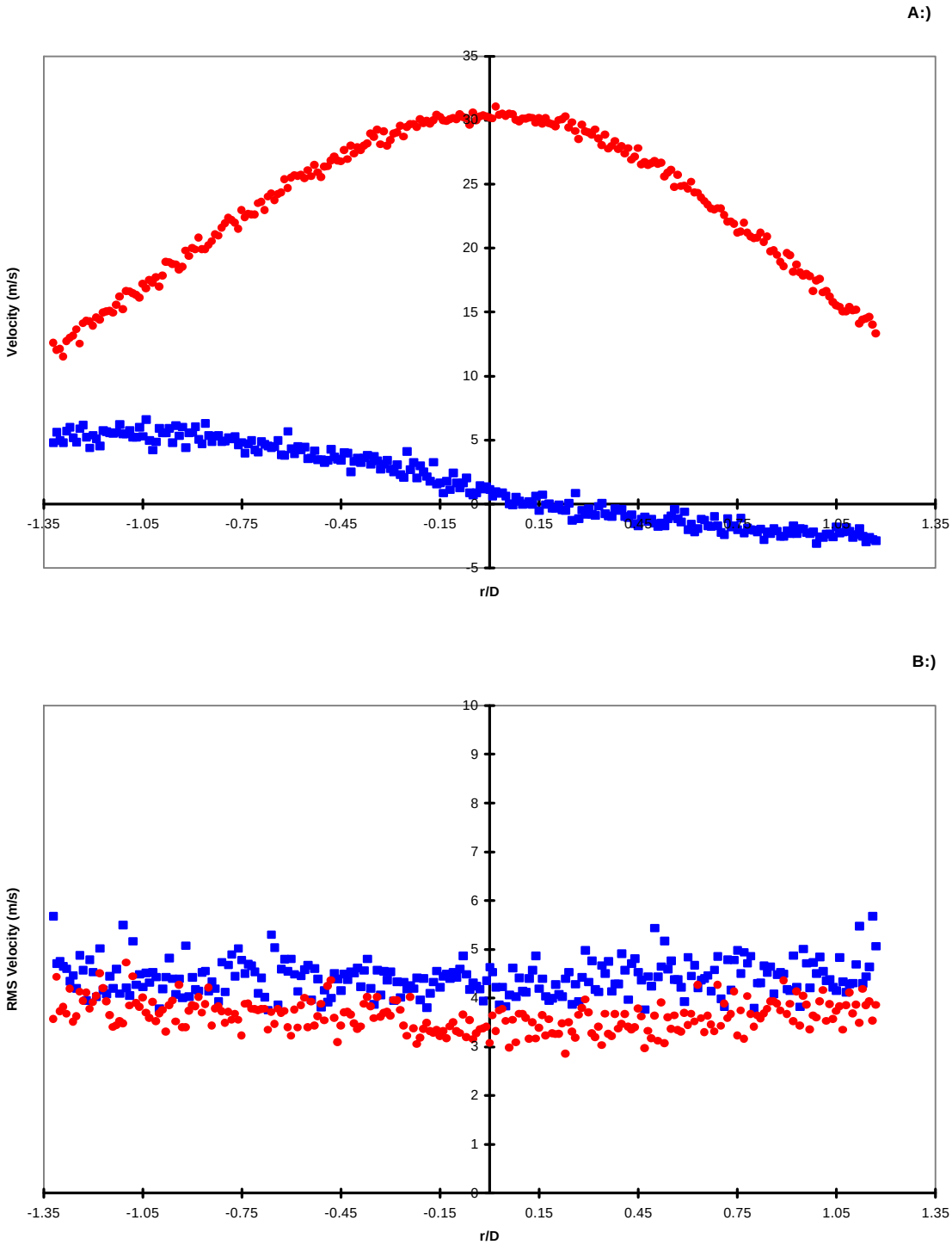

Figure A.22. Radial cut of swirling jet at X/D=6, run 2
Circles -axial velocity; Squares -circumferential velocity
a.) Mean Velocities
b.) RMS Velocities

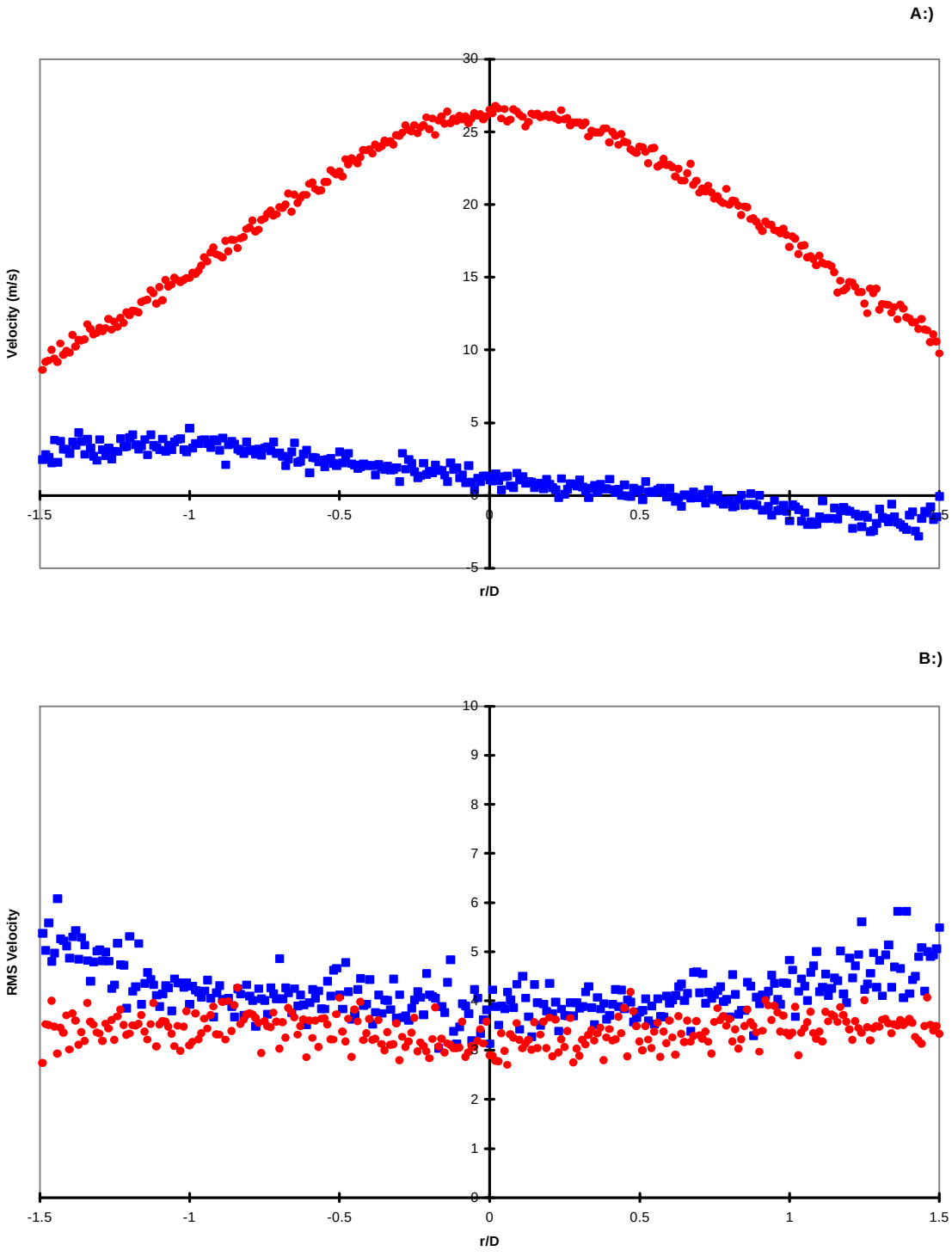

Figure A.23. Radial cut of swirling jet at X/D=8, run 2
Circles -axial velocity; Squares -circumferential velocity
a.) Mean Velocities
b.) RMS Velocities

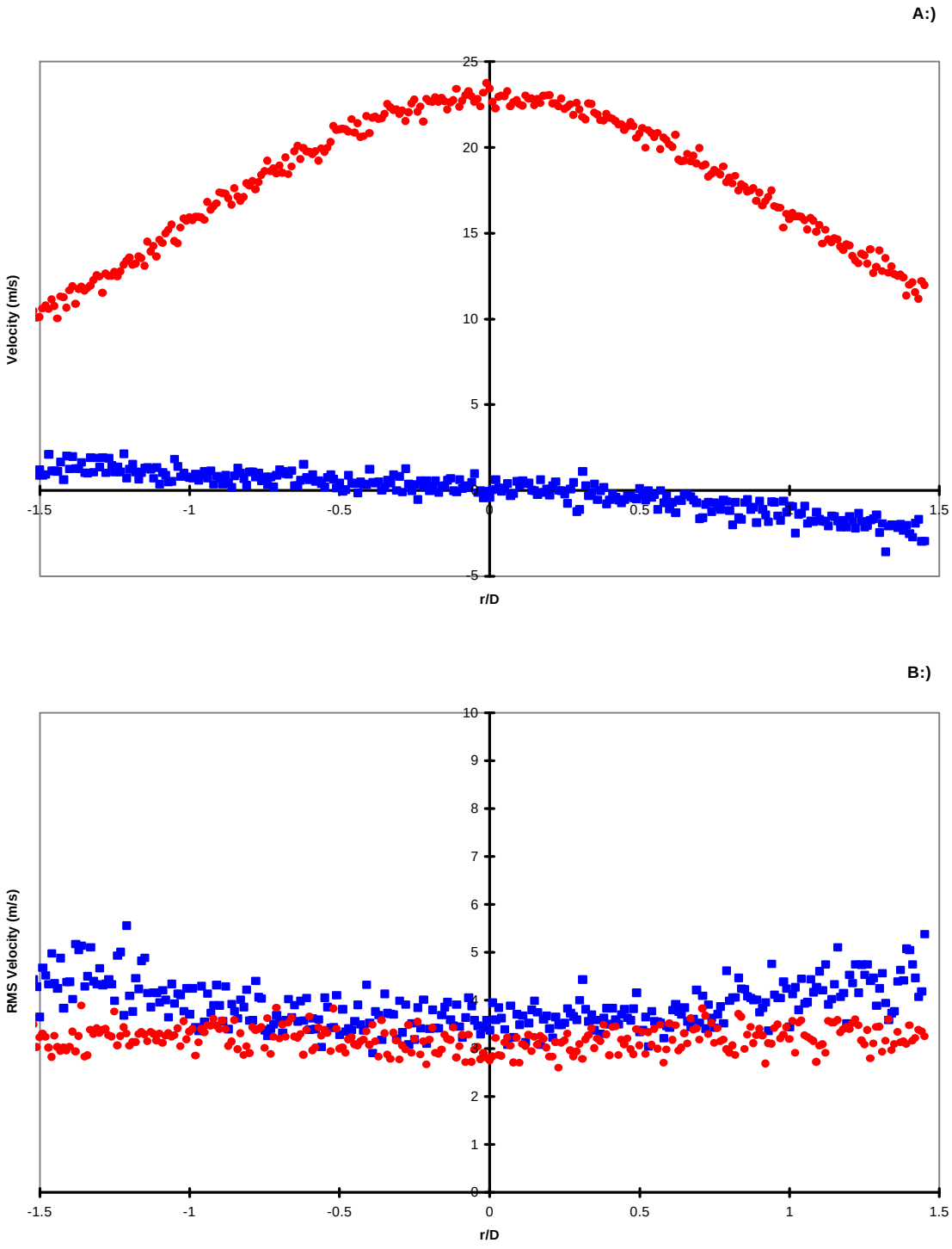

Figure A.24. Radial cut of swirling jet at X/D=10, run 2
Circles -axial velocity; Squares -circumferential velocity
a.) Mean Velocities
b.) RMS Velocities

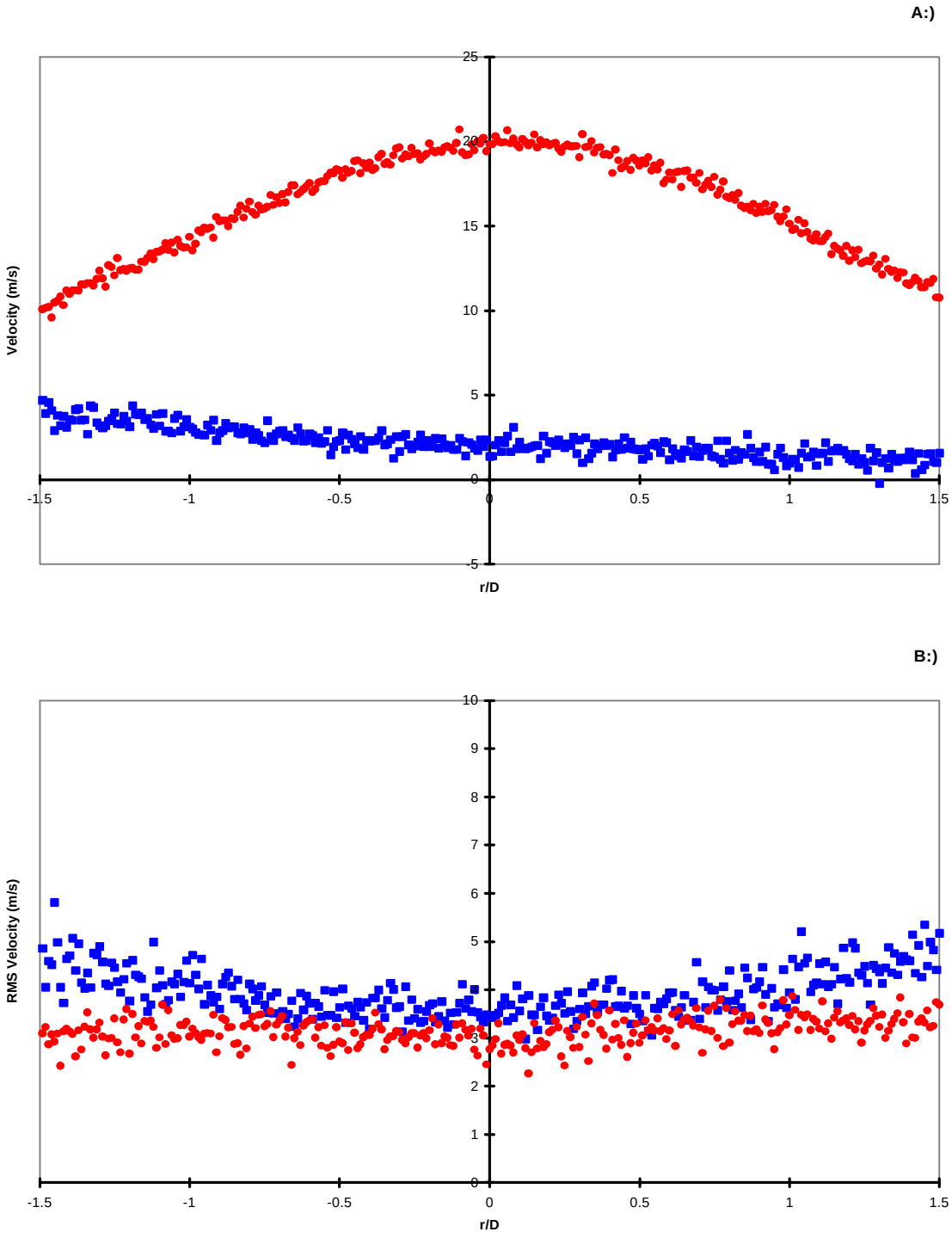

Figure A.25. Radial cut of swirling jet at X/D=12, run 2
Circles -axial velocity; Squares -circumferential velocity
a.) Mean Velocities
b.) RMS Velocities

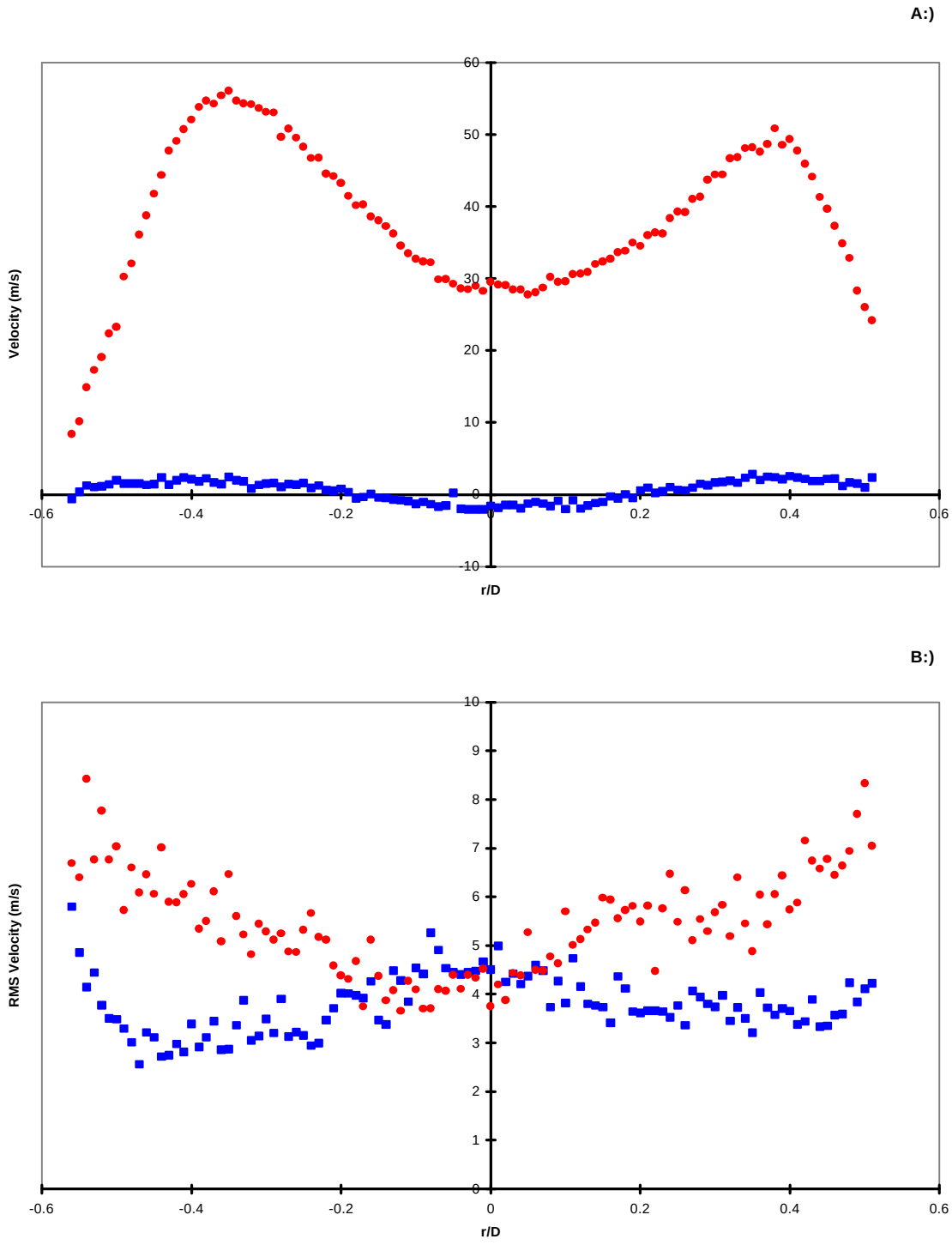

Figure A.26. Radial cut of annular jet at jet exit, run 1
Circles -axial velocity; Squares -circumferential velocity
a.) Mean Velocities
b.) RMS Velocities

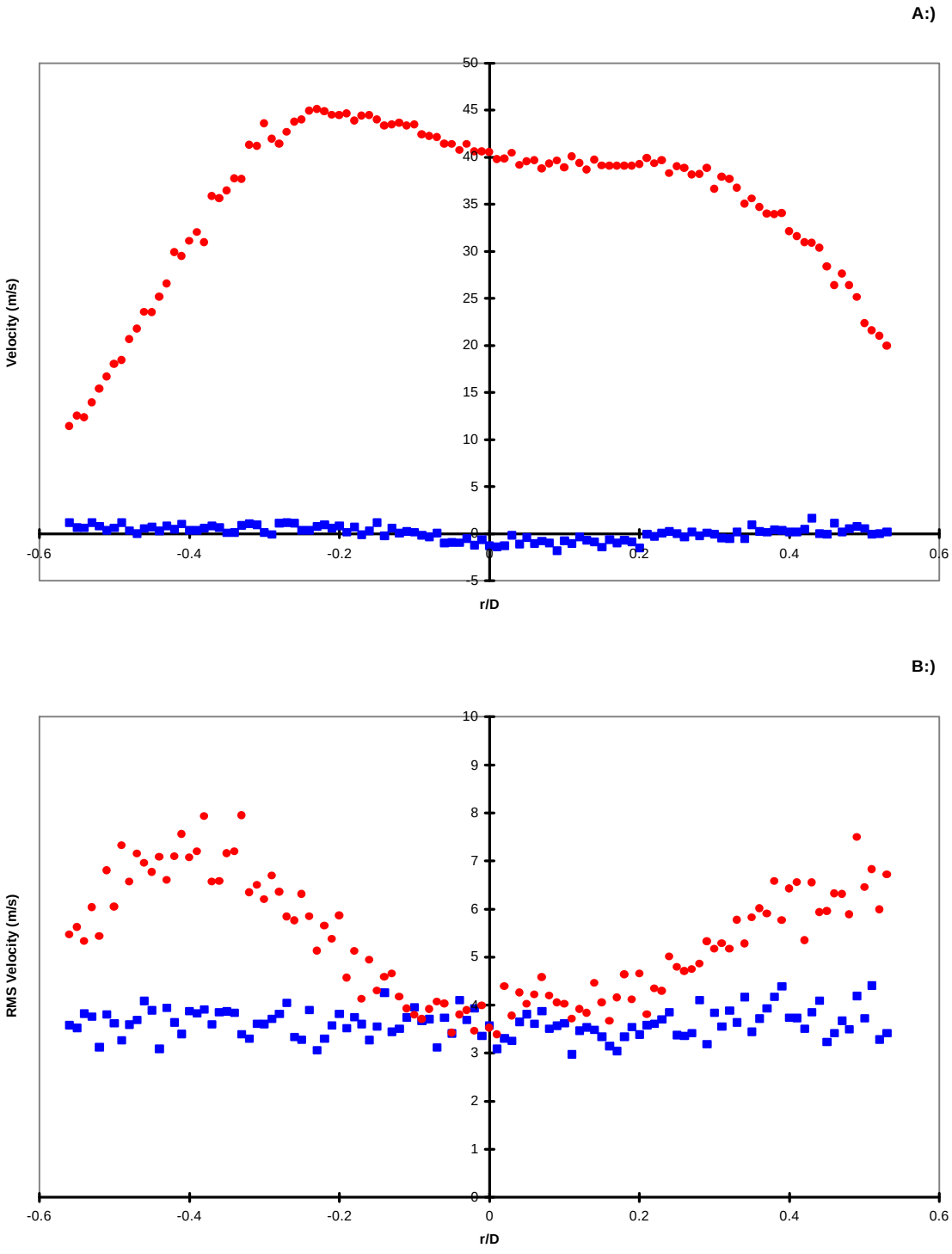

Figure A.27. Radial cut of annular jet at X/D=1, run 1
Circles -axial velocity; Squares -circumferential velocity
a.) Mean Velocities
b.) RMS Velocities

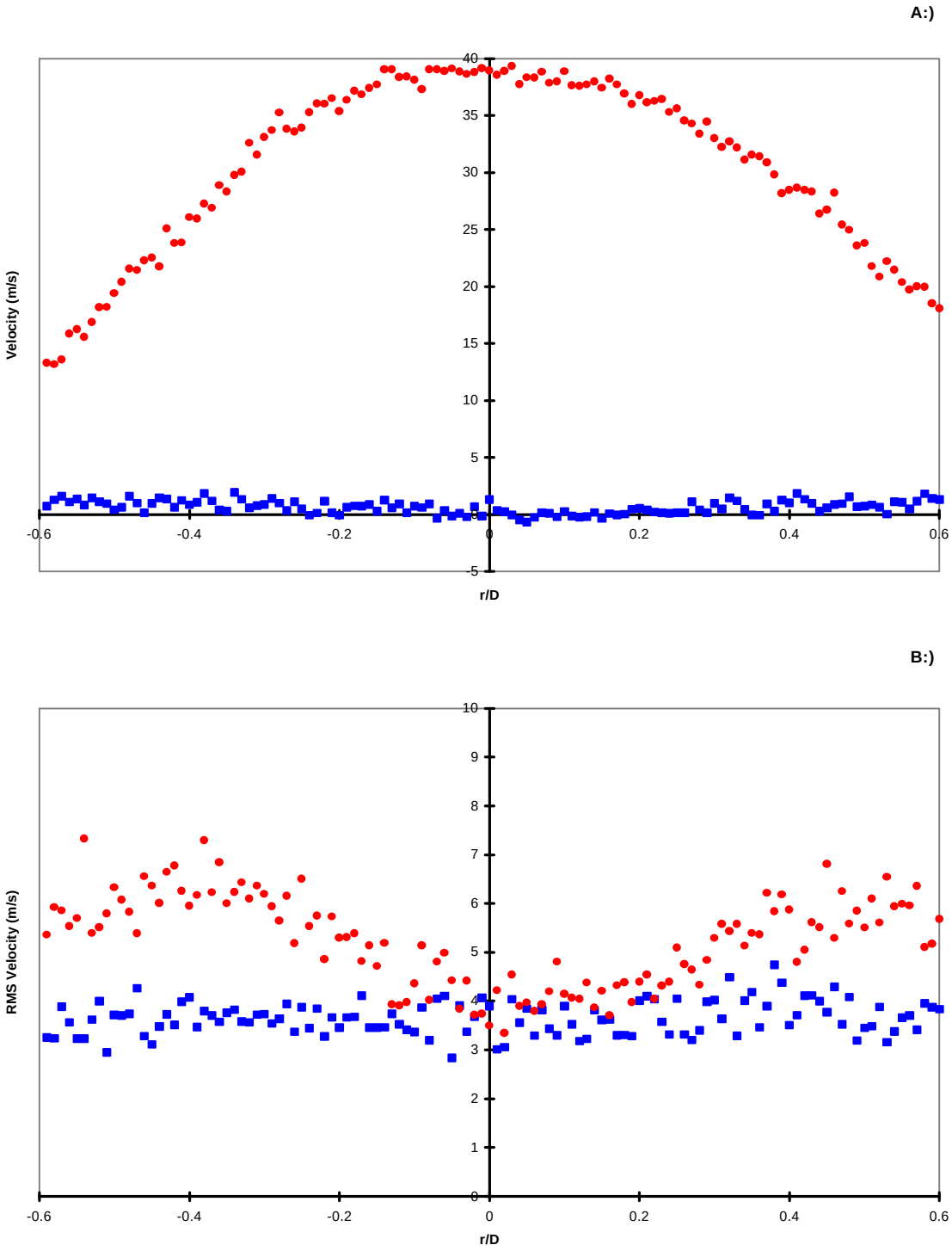

Figure A.28. Radial cut of annular jet at X/D=2, run 1
Circles -axial velocity; Squares -circumferential velocity
a.) Mean Velocities
b.) RMS Velocities

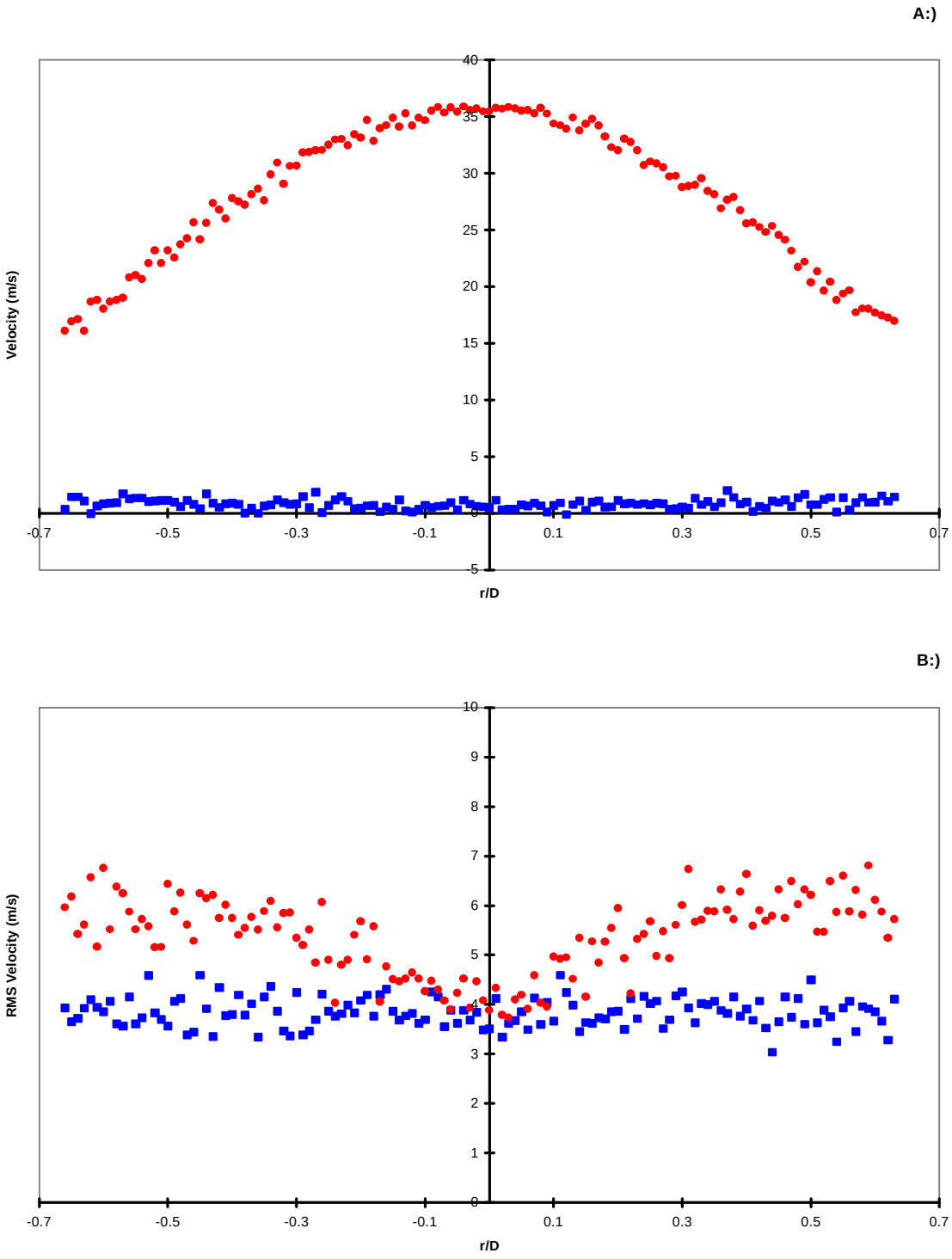

Figure A.29. Radial cut of annular jet at X/D=3, run 1
Circles -axial velocity; Squares -circumferential velocity
a.) Mean Velocities
b.) RMS Velocities

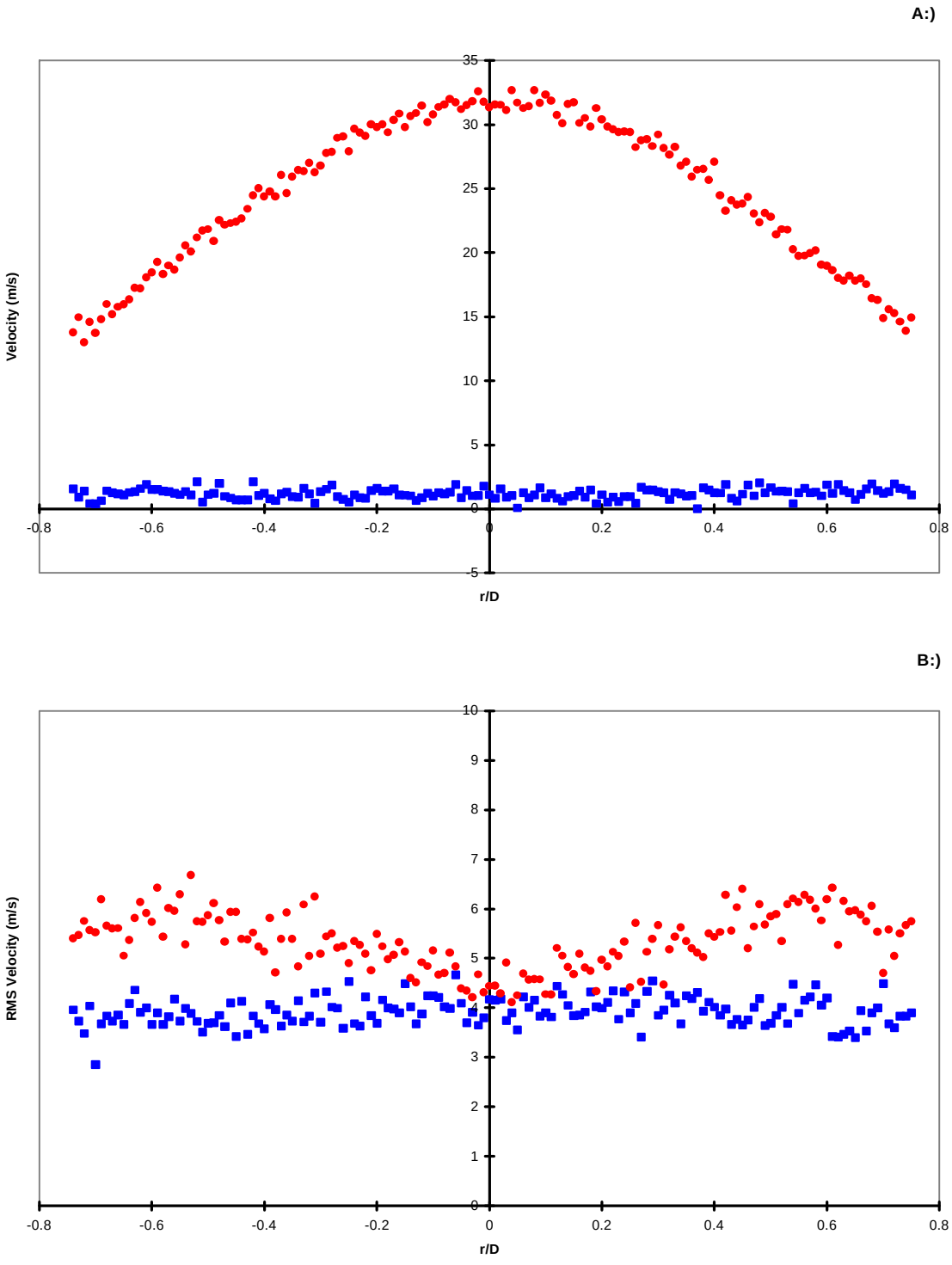

Figure A.30. Radial cut of annular jet at X/D=4, run 1
Circles -axial velocity; Squares -circumferential velocity
a.) Mean Velocities
b.) RMS Velocities

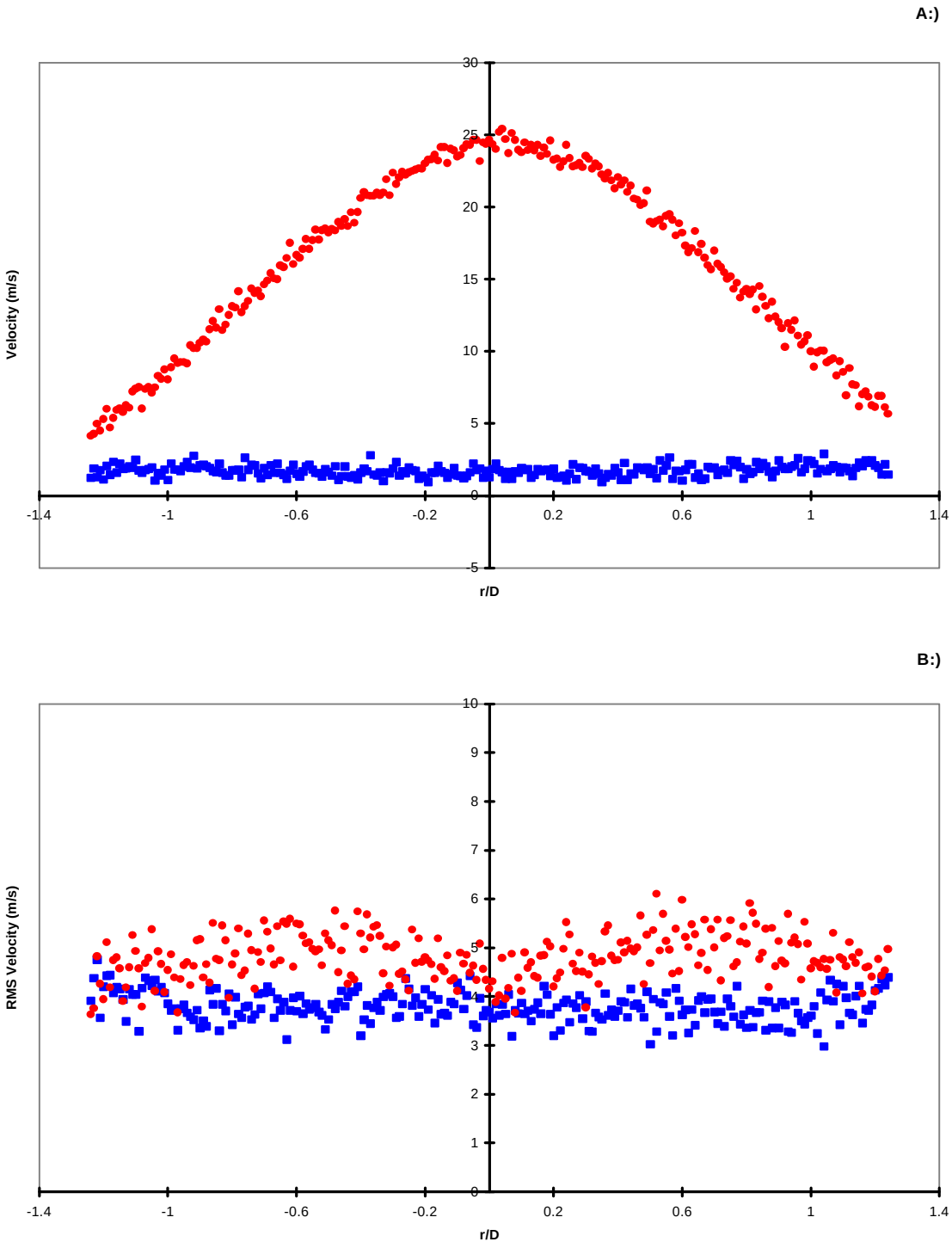

Figure A.31. Radial cut of annular jet at X/D=6, run 1
Circles -axial velocity; Squares -circumferential velocity
a.) Mean Velocities
b.) RMS Velocities

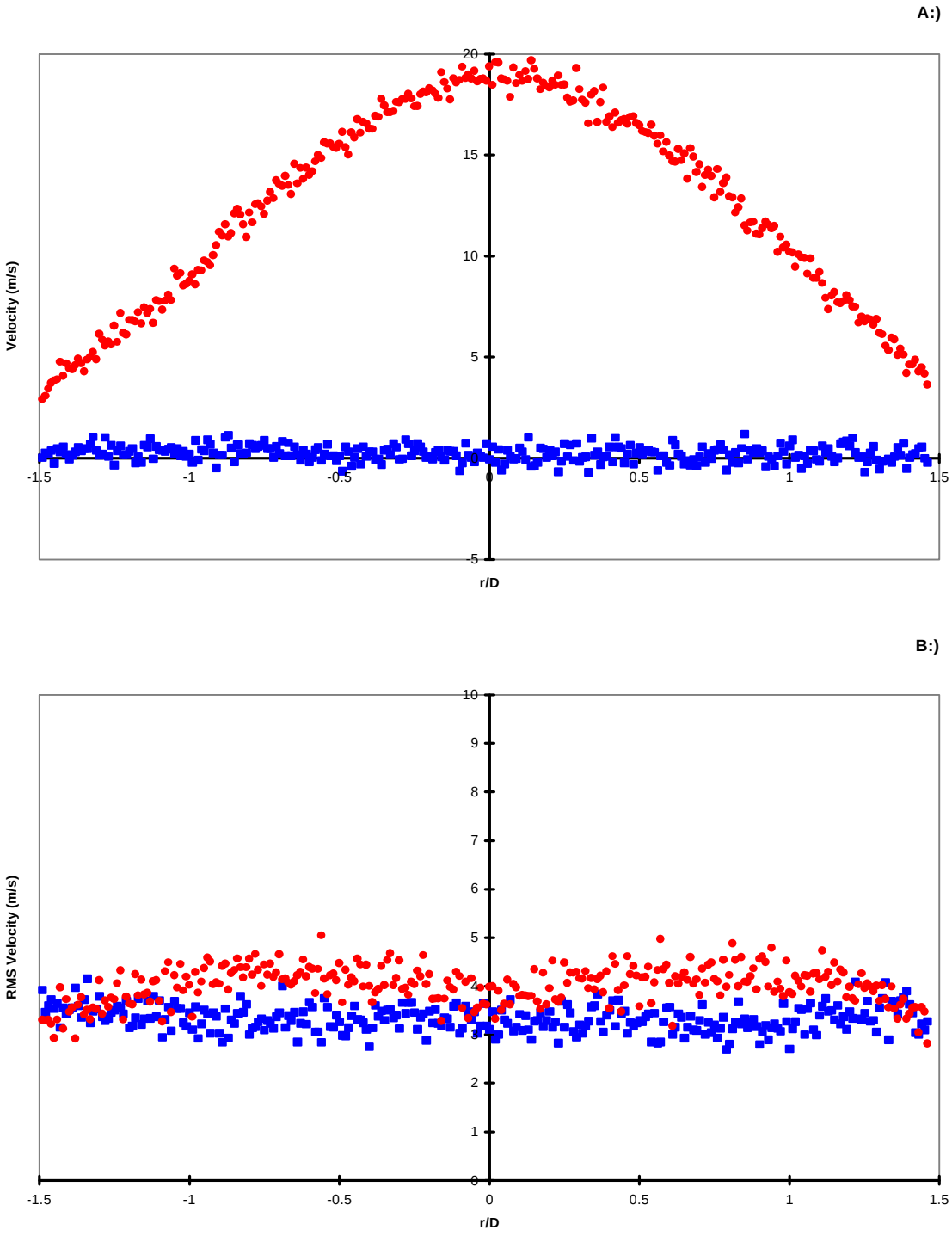

Figure A.32. Radial cut of annular jet at X/D=8, run 1
Circles -axial velocity; Squares -circumferential velocity
a.) Mean Velocities
b.) RMS Velocities

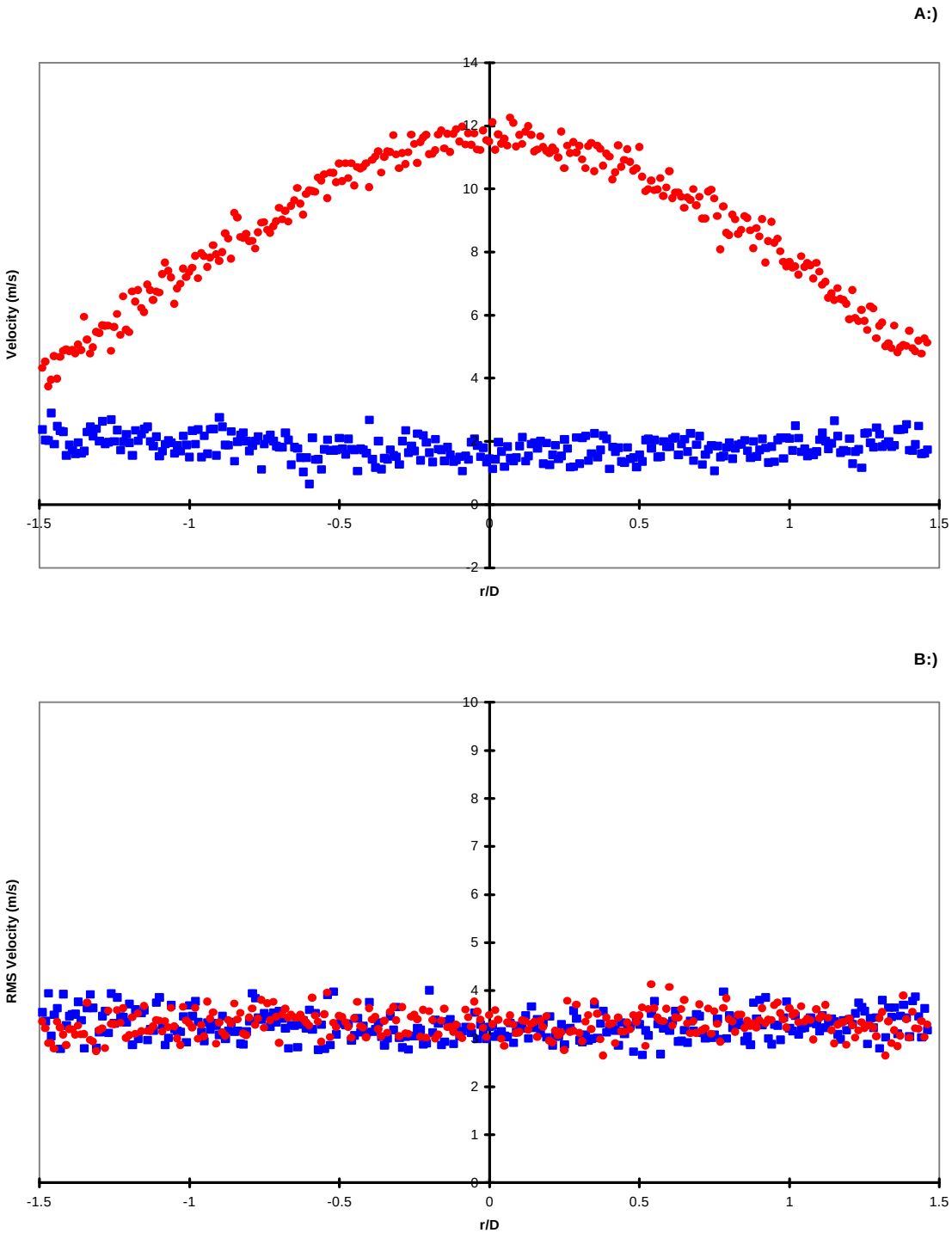

Figure A.33. Radial cut of annular jet at X/D=12, run 1
Circles -axial velocity; Squares -circumferential velocity
a.) Mean Velocities
b.) RMS Velocities

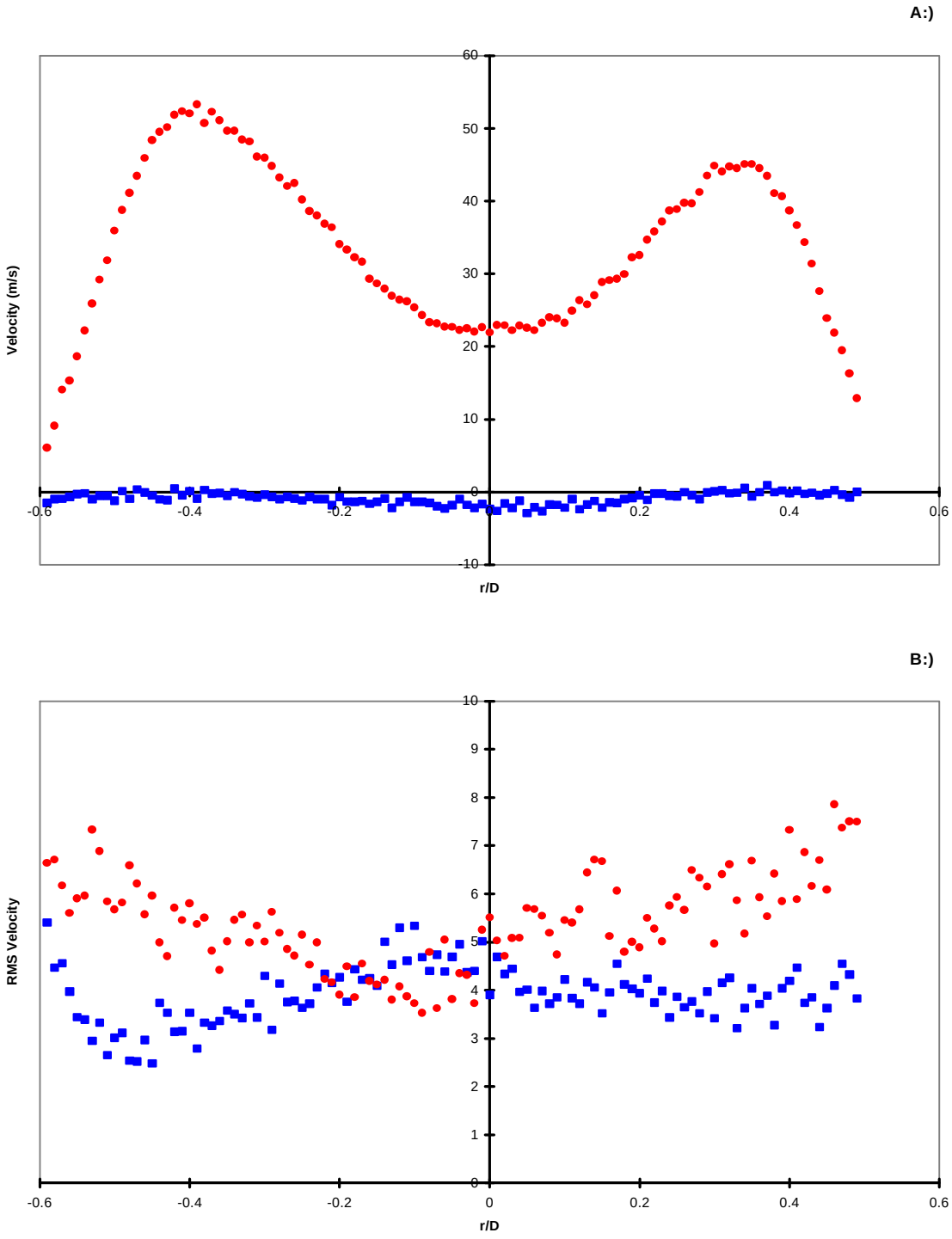

Figure A.34. Radial cut of annular jet at jet exit, run 2
Circles -axial velocity; Squares -circumferential velocity
a.) Mean Velocities
b.) RMS Velocities

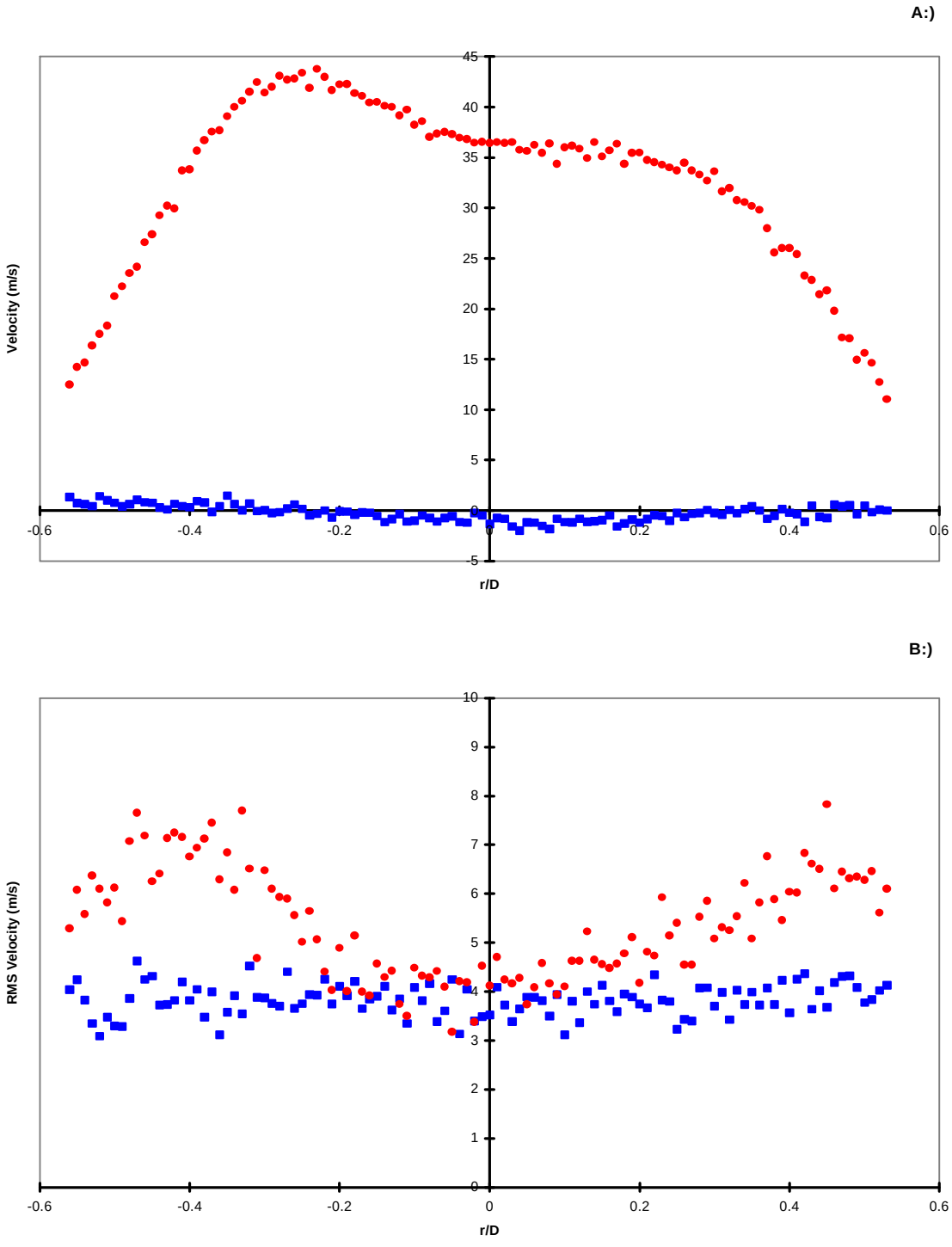

Figure A.35. Radial cut of annular jet at X/D=1, run 2
Circles -axial velocity; Squares -circumferential velocity
a.) Mean Velocities
b.) RMS Velocities

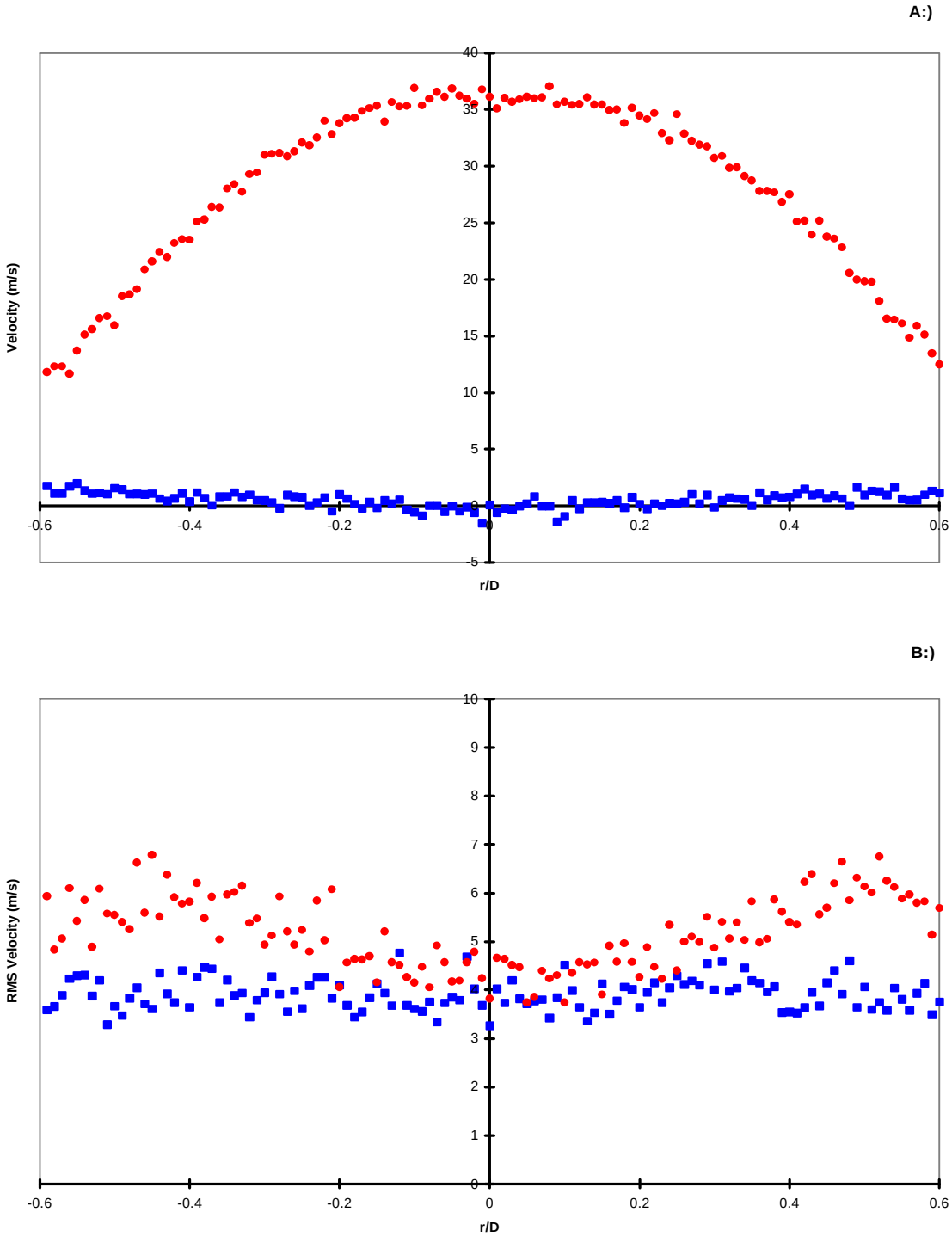

Figure A.36. Radial cut of annular jet at X/D=2, run 2
Circles -axial velocity; Squares -circumferential velocity
a.) Mean Velocities
b.) RMS Velocities

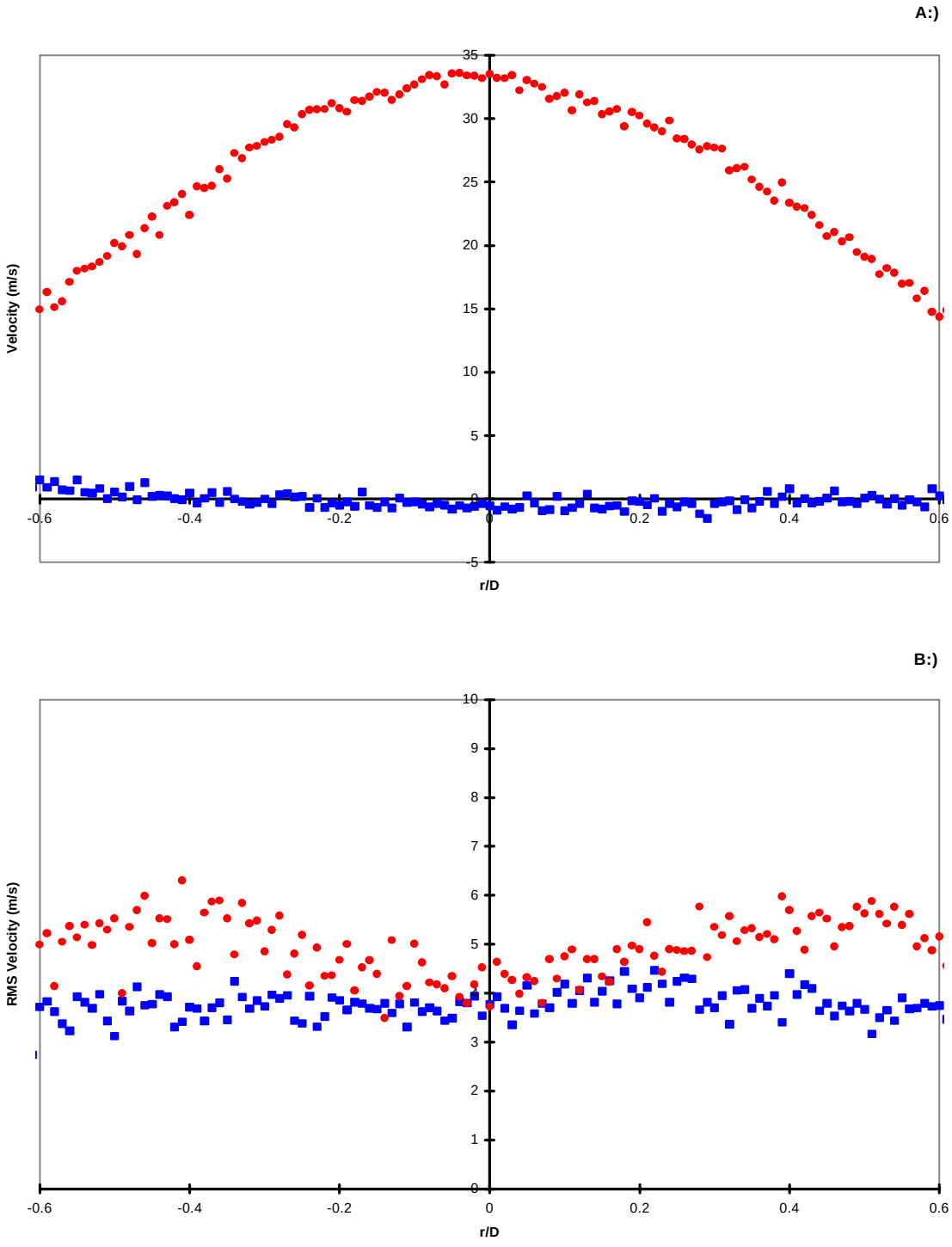

Figure A.37. Radial cut of annular jet at X/D=3, run 2
Circles -axial velocity; Squares -circumferential velocity
a.) Mean Velocities
b.) RMS Velocities

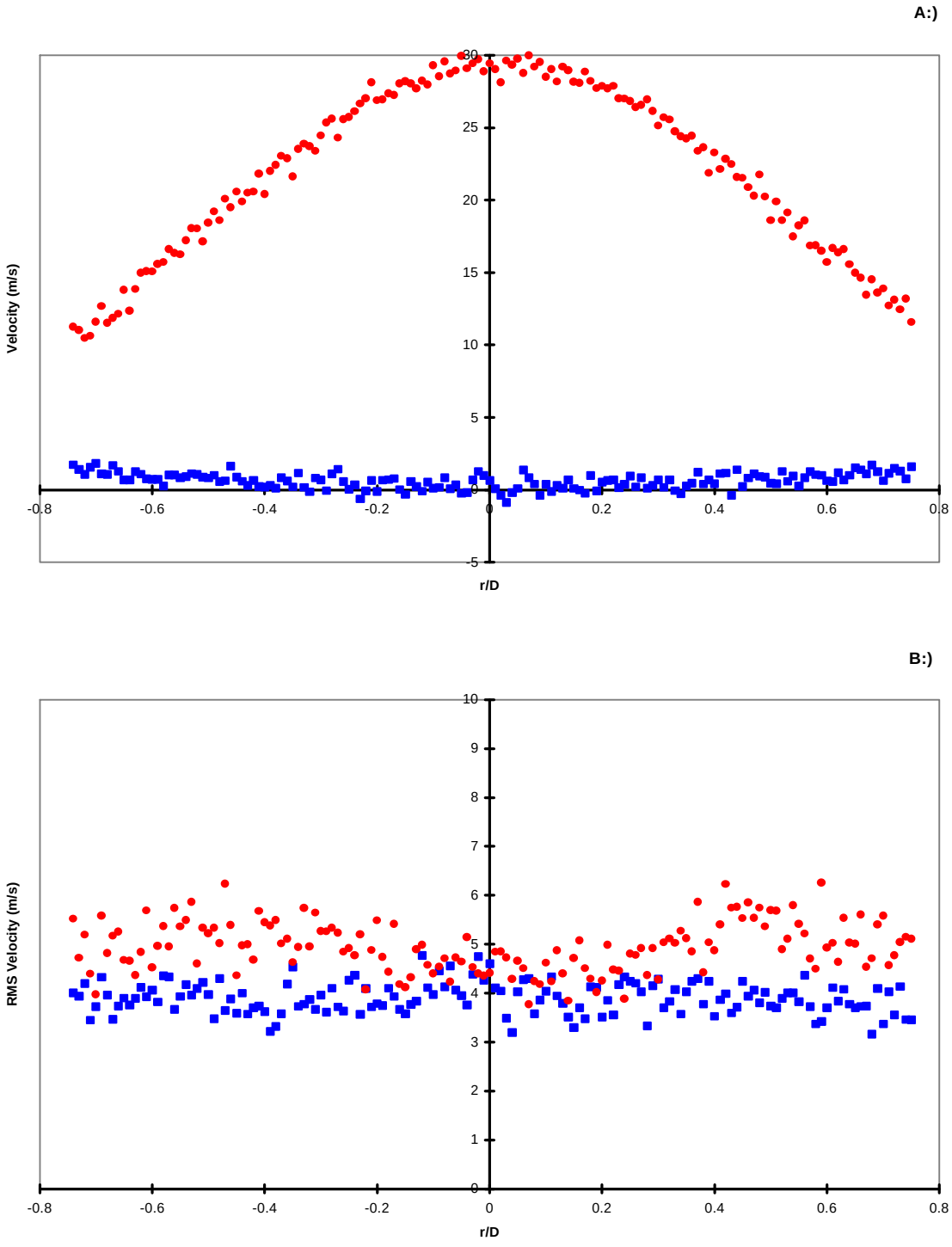

Figure A.38. Radial cut of annular jet at X/D=4, run 2
Circles -axial velocity; Squares -circumferential velocity
a.) Mean Velocities
b.) RMS Velocities

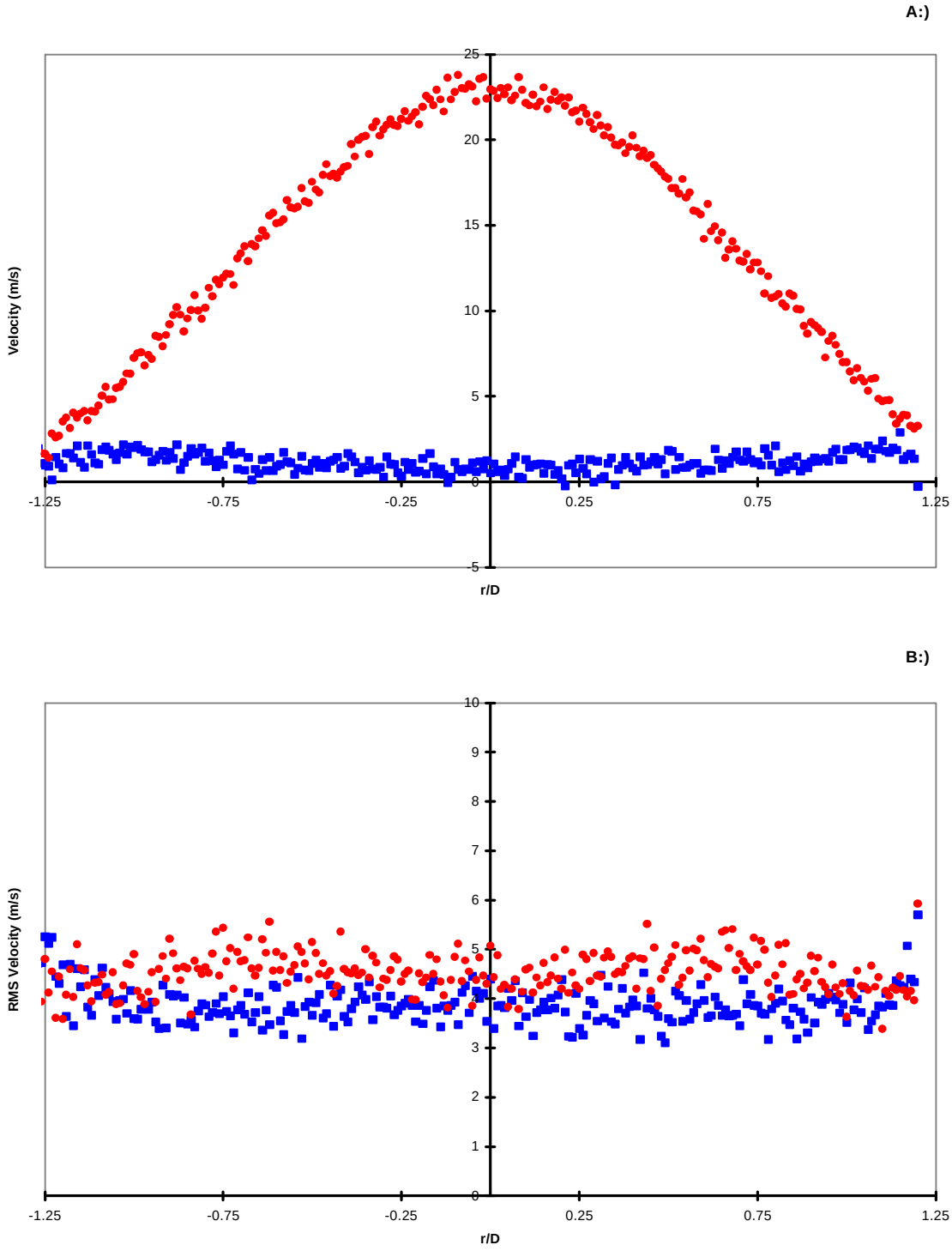

Figure A.39. Radial cut of annular jet at X/D=6, run 2
Circles -axial velocity; Squares -circumferential velocity
a.) Mean Velocities
b.) RMS Velocities

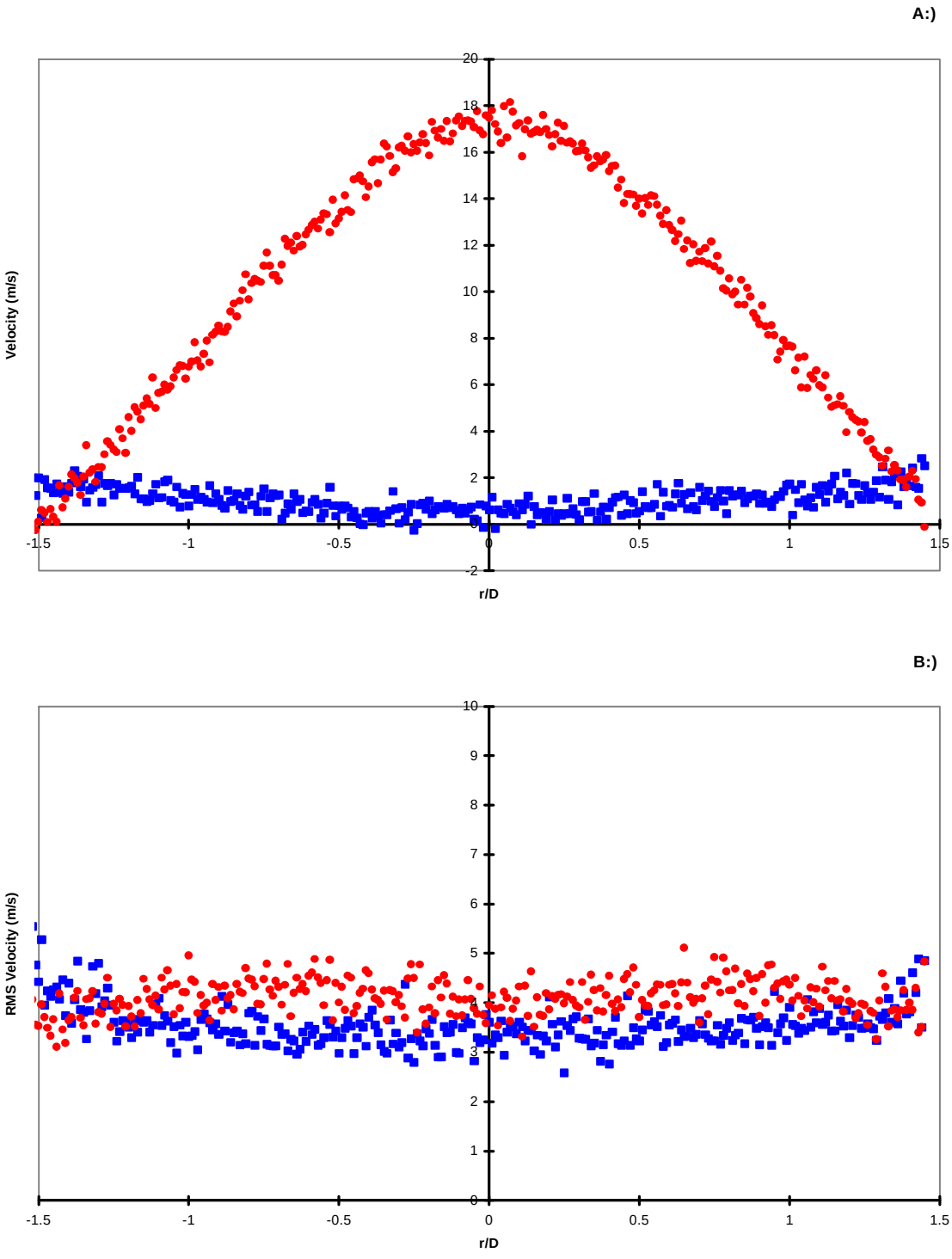

Figure A.40. Radial cut of annular jet at X/D=8, run 2
Circles -axial velocity; Squares -circumferential velocity
a.) Mean Velocities
b.) RMS Velocities

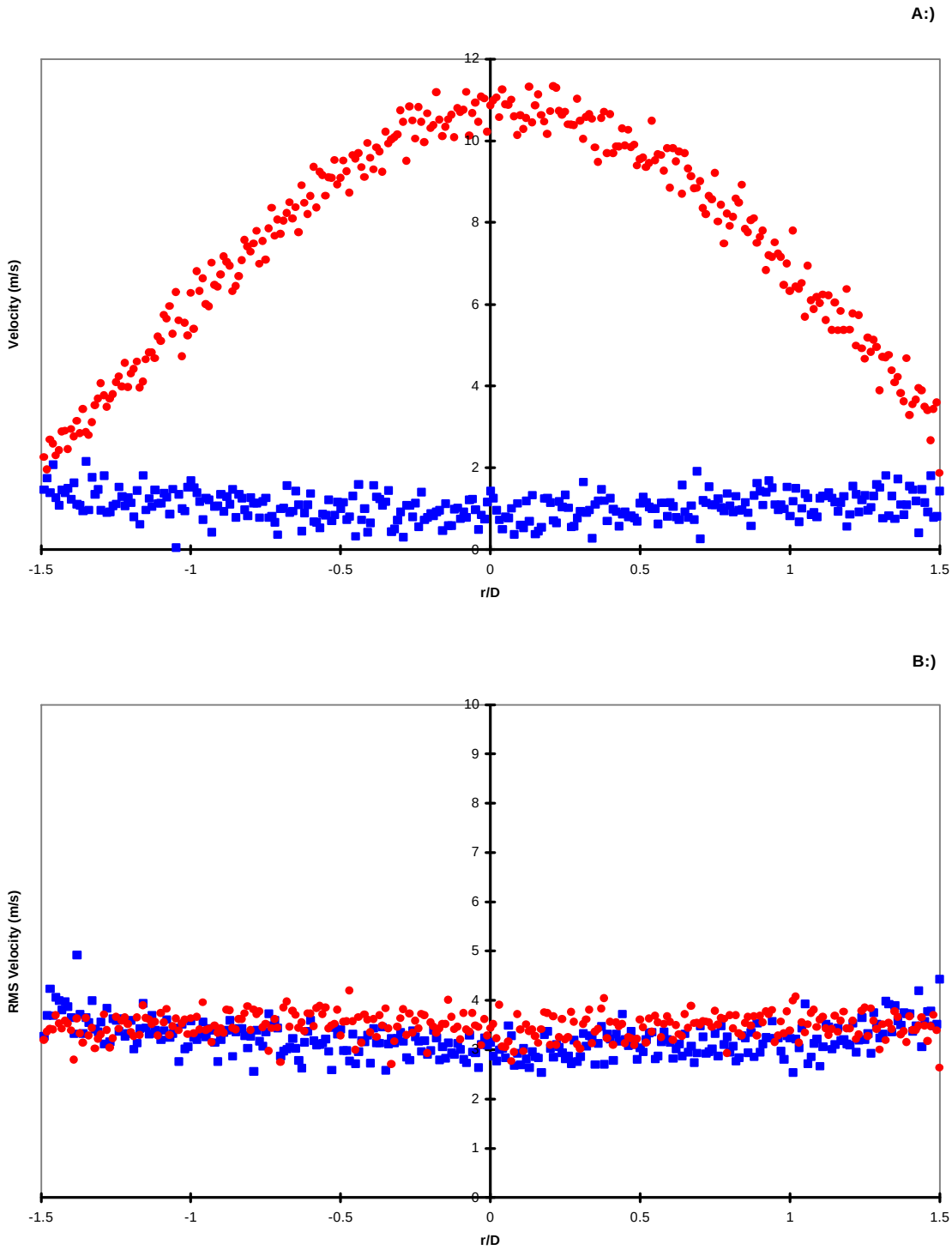

Figure A.41. Radial cut of annular jet at X/D=12, run 2
Circles -axial velocity; Squares -circumferential velocity
a.) Mean Velocities
b.) RMS Velocities